Untersuchung dimerisierter, frustrierter Heisenbergketten mittels DMRG-Methoden

Inaugural-Dissertation
zur
Erlangung des Doktorgrades
der Mathematisch-Naturwissenschaftlichen Fakultät
der Universität zu Köln

vorgelegt von
Friedhelm Schönfeld
aus Kirchen

Köln 1999

Berichterstatter:	Prof. Dr. E. Müller-Hartmann Priv.-Doz. Dr. A. Klümper

Tag der mündlichen Prüfung: 15. Juni 1999

Contents

Chapter 1

Introduction

One dimensional (1-d) systems provide a very fascinating and challenging field of activity from a theoretical point of view. This is mainly due to three reasons. First, 1-d systems show interesting phenomena and surprisingly rich phase diagrams because of the enhanced role of quantum fluctuations. Second, the one-dimensionality allows for derivations of several analytical results and facilitates numerical studies. Above all the density matrix renormalization group is suitable for these systems. Thus, 1-d systems provide a huge testing ground for numerical as well as analytical approaches. Third, several compounds allow for a theoretical description by means of quasi 1-d models, due to their chain structure[1]. Hence, in contrast to the naive expectation, in many cases the theoretical results can directly be compared to the experimental findings.

Since the discovery of $CuGeO_3$ as the first inorganic spin-Peierls (SP) compound [1], this substance has played a key role among the quasi 1-d systems. The SP transition, which is the analogue to the well known Peierls transition, is for two reasons of particular interest. On the one hand, the driving force can be understood on the basis of a simple quantum mechanical argument: The state of lowest energy of two $S =$

---

[1] In these compounds the interaction along one direction (chain direction) is much larger than perpendicular to it. Or, the interactions are of the same order of magnitude with the interchain interaction being highly frustrated leading to an effective reduction.

1/2 spins is the $S = 0$ singlet state. Hence, two adjacent spins tend to form a local spin-singlet even if they are embedded in a larger system. On the other hand, SP systems show a rich phase diagram and complex phenomena, e.g. in presence of a magnetic field or under doping.

The first observations of SP transitions in *organic* materials were already obtained in the 70's. The discovery of $CuGeO_3$, however, as an *inorganic* SP compound has considerably renewed the interest in this phenomenon. Large crystals of high quality can now be synthesized allowing for a variety of very precise experimental studies. The quasi 1-d chain structure which is embedded in a relatively simple 3-d lattice structure facilitates understanding of the experimental results. Furthermore, $CuGeO_3$ can be easily doped. This makes detailed investigations of the observed antiferromagnetism, which occurs under doping, possible. Moreover, the constituting components of $CuGeO_3$ are copper-oxygen octahedra as in the case of the high-temperature superconductors [2], so some of the experience with cuprates can be carried over.

$CuGeO_3$ has attracted enormous theoretical as well as experimental efforts and a particular thorough understanding of many properties has been achieved. On this basis a large part of comprehension of the microscopic mechanisms in $CuGeO_3$ can presumably be transferred to more complex systems in the near future.

Throughout this thesis SP compounds are described in the framework of dimerized, frustrated Heisenberg chains. The method of choice for treating the 1-d model is the density matrix renormalization group (DMRG) approach. This numerical algorithm was formulated in 1992 by Steve White [3, 4]. The DMRG technique is an extremely powerful tool for calculating properties of 1-d systems. Considering system sizes which can be handled, accuracy of the results and variety of models which can be treated, DMRG turns out to be superior to most other numerical approaches such as exact diagonalization or quantum Monte-Carlo simulations, for instance. Furthermore, the recently developed transfer-matrix DMRG (T-DMRG) which combines White's DMRG idea with the transfer-matrix approach [5–7] is an excellent tool for studying thermodynamic properties of 1-d systems.

The purpose of this thesis is twofold. First, several properties of general dimerized, frustrated Heisenberg chains are numerically investigated. The findings are discussed and compared to analytical results as far as those are accessible. Second, many experimentally observed features of $CuGeO_3$ are reproduced, verifying the validity of the chosen 1-d adiabatic approach. In many cases remarkable agreement is obtained between numerical and experimental results. Thus, within the approach chosen several properties can be explained on the basis of microscopic mechanisms.

An introduction to the basic DMRG algorithm is given in the next section. The extension to finite temperatures is illustrated in the following one. In the fourth section some fundamental properties of $CuGeO_3$ are reviewed and the model Hamiltonian is set up. The next two sections deal with $T = 0$ properties of SP systems. In particular the dimerization parameter for $CuGeO_3$ is determined. Furthermore, low lying excitations, doped systems and SP systems in an external magnetic field are investigated. In section seven finite-temperature results are derived and compared to the experimental findings of $CuGeO_3$. A summary and conclusion are given in chapter eight.

Chapter 2

Density Matrix Renormalization Group

The formulation of the density matrix renormalization group (DMRG) method by Steven White in 1992 [3, 4] was a breakthrough in the field of numerical renormalization group techniques. It has proven to be an extremely powerful technique for quasi one-dimensional quantum systems. A remarkable advancement is the recently developed extension to finite temperatures, combining the transfer-matrix approach with White‘s DMRG idea [5–7]. The partition function and the derivable quantities in the thermodynamic limit at finite temperatures are now numerically accessible, in principle for any one-dimensional translationally invariant model with short range interactions.

2.1 Concept of Renormalization

The basic idea of all lattice renormalization group techniques is to enlarge the system iteratively but keeping only a constant number of basis states. For example for a one-dimensional spin system the first step can be to assort the lattice sites into blocks of N sites. Then the Hamiltonian is divided into intrablock and interblock contributions. Now one can assign a so-called *Kadanoff block spin* to each block. For instance, the block can be identified with a single spin $S = 1/2$ by choosing the two block states with the lowest energies in the subspace $S^z = \pm 1/2$ as new basis states. The two possible spin orientations correspond to the selected basis states [8]. By iterating the above procedure one obtains recursion relations on the set of coupling constants which define the Hamiltonian and properties in the thermodynamic limit can be derived approximately. A similar approach, the *numerical real-space renormalization group method*, was first formulated by Wilson for the solution of the Kondo problem [9]. After dividing the infinite chain into identical blocks A of N sites and m basis states each, the Hamiltonian matrix H_{AA} for two adjacent blocks is diagonalized. The m lowest lying eigenstates form the truncated basis for the new block A' which is twice as large as the old one:

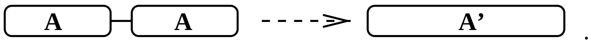

This procedure is iterated using the new block A' in the truncated representation as the basis block. The basic assumption in this approach is that only the energetically lowest lying block eigenstates are relevant for the ground state of the final (infinite) system. The essential problem, however, lies in the correct treatment of the boundaries. In the above approach the two adjacent blocks which are considered in one step are not connected to the rest of the chain. Hence, the eigenstates which are kept as the new basis are likely to have inappropriate features at the edges for describing the block as part of an infinite chain (see [4] and references therein). The DMRG method provides a good way to overcome the difficulty of choosing appropriate boundary condition for the new block.

2.2 Density Matrix

As pointed out above the crucial question is the selection of the new basis states in the renormalization step. The answer how to find an optimal truncated basis for a block B was given by White [3, 4]. To account for the fact that the block B is embedded in an infinite chain a *larger* system has to be considered to find the most important states of the subsystem B. The eigenstate of interest of the so-called *superblock*, i.e. the enlarged system, is usually the ground state. This state is called *target state* henceforth. Analyzing it's projection onto the relevant subsystem B it turns out that the most important states can be chosen by means of a density matrix of the corresponding subsystem. To illustrate how the density matrix enters in this context we consider a system (superblock) which consists of two blocks[1]

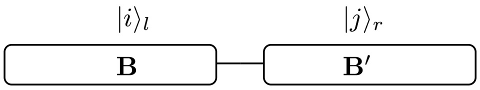

.

Let $|i\rangle_{l(r)}, i = 1, ..., k$ be an orthonormalized basis set of the left (right) block. The system is assumed to be in the normalized state (target state)

$$|\psi\rangle = \sum_{i,j} \psi_{i,j} |i\rangle_l |j\rangle_r \ . \tag{2.1}$$

The density matrix (of the left subsystem) comes immediately into play if we ask for the probability $p(i_0)$ of the left part being in a certain state $|i_0\rangle_l$. This probability reads

$$p(i_0) = \langle\psi|P_{i_0}|\psi\rangle \ , \tag{2.2}$$

where the projector P_{i_0} is given by [10]

$$P_{i_0} = |i_0\rangle_l \ {}_l\langle i_0| \sum_j |j\rangle_r \ {}_r\langle j| \ . \tag{2.3}$$

Inserting $|\psi\rangle$ and P_{i_0} in Eq. (2.2) one finds

$$p(i_0) = \sum_j \psi_{i_0,j} \psi^*_{i_0,j} \ , \tag{2.4}$$

due to the orthonormality of the basis sets. Hence, the probability is given by a diagonal element of the matrix

$$\rho_{i,i'} = \sum_j \psi_{i,j} \psi^*_{i',j} \ . \tag{2.5}$$

---

[1] The right block B′ corresponds to the rest of the (infinite) chain. For practical reasons, however, both blocks are often chosen to be identical, i.e. B′=B in the numerical application.

Eq. (2.5) defines the density matrix of $|\psi\rangle$ with respect to the left subblock B. According to (2.5) ρ is hermitian and since $|\psi\rangle$ is normalized $\mathrm{tr}\rho = 1$ is satisfied. The condition $\lambda_\alpha \geq 0$ for all eigenvalues of ρ follows from

$$\langle\varphi|\rho|\varphi\rangle = \sum_{i,i'} \varphi_i \, \rho_{i,i'} \, \varphi_{i'} \;= \sum_j \Big|\sum_i \varphi_i \, \psi_{i,j}\Big|^2 \geq 0 \,, \tag{2.6}$$

for any state $|\varphi\rangle$.

The most important states which should be kept in each renormalization step are those with the highest probability for the corresponding subsystem and they can be selected by means of the density matrix ρ (2.5). To show that these are the eigenstates of the density matrix which belong to the largest eigenvalues and that they are indeed optimal to represent the subsystem one has to minimize [4]

$$S = \| \, |\psi\rangle - |\tilde{\psi}\rangle \|^2 \,, \tag{2.7}$$

where $|\tilde{\psi}\rangle$ is the representation of the target state $|\psi\rangle$ with a truncated basis for the left block. So the aim is to find for a given m the truncated basis states $|\tilde{u}^\alpha\rangle, \alpha = 1, ..., m$ $(m \leq k)$ which are optimal for representing $|\psi\rangle$ in the subsystem. With $|\tilde{u}^\alpha\rangle = \sum_i \tilde{u}_i^\alpha |i\rangle_l$ the approximation reads

$$|\tilde{\psi}\rangle = \sum_{\alpha,j} a_{\alpha,j} |\tilde{u}^\alpha\rangle |j\rangle_r \tag{2.8}$$

and defining $|\tilde{v}^\alpha\rangle := \sum_j a_{\alpha,j} \tilde{d}_\alpha^{-1} |j\rangle_r = \sum_j \tilde{v}_j^\alpha |j\rangle$

$$|\tilde{\psi}\rangle = \sum_\alpha \tilde{d}_\alpha |\tilde{u}^\alpha\rangle |\tilde{v}^\alpha\rangle \,. \tag{2.9}$$

The constants $\tilde{d}_\alpha^{-1}$ are chosen to normalize $|\tilde{v}^\alpha\rangle$ i.e. to set $\sum_j |\tilde{v}_j^\alpha|^2 = 1$. Rewriting Eq. (2.7) in matrix notation

$$S = \sum_{i,j} \left| \psi_{i,j} - \sum_{\alpha=1}^{m} \tilde{d}_\alpha \tilde{u}_i^\alpha \tilde{v}_j^\alpha \right|^2 \,, \tag{2.10}$$

one recognizes that the minimization problem is equivalent to that of approximating a certain matrix ψ. Such problems can be solved by means of the singular value decomposition (SVD) [11]. The SVD-theorem states that every matrix is unitarily equivalent to a diagonal matrix with non-negative elements. The diagonal consists of the so-called singular values [12]. Thus the matrix ψ can be written as

$$\psi = UDV^\dagger \iff \psi_{i,j} = \sum_{\beta=1}^{k} d_\beta u_i^\beta v_j^\beta \tag{2.11}$$

where D is a diagonal matrix with positive or zero elements d_β. Since ψ is a quadratic $k \times k$ matrix the same holds for D and the unitary matrices U and V.

To minimize S the transformations U and V of $\psi_{i,j}$ are also applied to the approximation $\tilde{\psi}_{i,j}$:

$$U^\dagger \, \tilde{\psi} \, V =: B \iff \tilde{\psi} = UBV^\dagger \,. \tag{2.12}$$

The matrix B will be determined via the minimization of S. To this end it is helpful to rewrite Eq. (2.10) by means of a trace using expressions (2.11) and (2.12) for ψ and $\tilde{\psi}$, respectively

$$\begin{aligned} S &= \operatorname{tr}\big\{(\psi - \tilde{\psi})^\dagger (\psi - \tilde{\psi})\big\} \\ &= \operatorname{tr}\big\{V(D - B^\dagger)U^\dagger U(D - B)V^\dagger\big\} \\ &= \operatorname{tr}(D - B^\dagger)(D - B) \\ &= \sum_{i,j} |d_{i,j} - b_{i,j}|^2 \,. \end{aligned} \tag{2.13}$$

As D is diagonal S is minimized for vanishing off-diagonal elements of B, i.e. $b_{i,j} = 0$ for $i \neq j$. Since a reduction of the number of basis states is to be achieved ($k \to m$) the matrix B must not contain more than m nonzero diagonal elements $b_{i,i}$ (cf. the representation of $\tilde{\psi}$ in Eq. (2.10) which resembles already a SVD). Obviously Eq. (2.13) is then minimized if B contains the dominant singular values of ψ which are the largest elements of D. Hence the optimum approximation reads

$$\tilde{\psi}_{\text{opt}} = U \, \tilde{D} \, V^\dagger \,, \tag{2.14}$$

where the diagonal matrix $\tilde{D}$ contains the m largest singular values and $k - m$ additional zeros.

For the calculation of the relevant d_i the SVD is not used explicitly. The largest singular values and the corresponding $|u^\alpha\rangle$ vectors are derived by diagonalizing the density matrix (2.5), which can be written as

$$\rho = UD^2U^\dagger \ . \tag{2.15}$$

Each eigenvalue of ρ $\lambda_\alpha = d_\alpha^2$ can be interpreted as the probability for the left block B to be in the corresponding eigenstate $|u^\alpha\rangle$. To summarize, it is shown that the optimum basis states for the left subsystem are the eigenstates belonging to the largest eigenvalues of ρ.

2.3 DMRG Algorithm

Once having formulated the selection criterion one can set up the DMRG algorithm. The standard algorithm for an infinite chain is the following:

0. Start with a small block (B) of length L which can be treated exactly. Let $\tilde{m}$ denote the dimension of the corresponding Hilbert space.

1. Add one site (s) to the block and set up the corresponding Hamiltonian $H_{\mathrm{B-s}}$ (The enlarged block B−s corresponds to the subsystem B in the previous section.).

2. Combine two enlarged blocks to form the *superblock* and generate the Hamilton matrix $H_{\mathrm{B-s-s-B}}$ or $H_{\mathrm{B-s-B-s}}$ (see below).

3. Use a sparse matrix diagonalization method such as the Davidson [13] or the Lanczos [14,15] algorithm to find $|\psi\rangle$ the so-called *target state*, e.g. the ground state of the superblock.

4. Form the reduced density matrix[2] for the left half of the system

---

[2] For the studied model the target state and hence the density matrix can always be chosen to be real.

$\rho(i,i') = \sum_j \psi_{i,j}\psi_{i',j}$ [3] and find the m eigenvectors corresponding to the largest eigenvalues. These constitute the columns of the transformation matrix U.

$\boxed{\mathbf{5.}}$ Transform the Hamiltonian and all other relevant operators of the left part (B$-$s) which are used to generate the new Hamiltonian (and possible additional operators of interest) of the superblock in the next step. The transformation onto the truncated new basis reads:

$$H' = U^T H_{\mathrm{B-s}} U.$$

$\boxed{\mathbf{6.}}$ Identify H' with H_{B} and return to $\boxed{1.}$

In each iteration step the superblock is enlarged by the two additional sites (s$-$s), whereas the number of basis states is kept fixed. The calculated properties converge to their values in the thermodynamic limit.

The crucial point in the above algorithm is the storage and the diagonalization of the superblock Hamiltonian. In the following dimerized, frustrated Heisenberg chains are investigated; a site corresponds to a spin $S = 1/2$. Therefore the matrix $H_{\mathrm{B-s-s-B}}$ or $H_{\mathrm{B-s-B-s}}$ consists of $(4\,m^2)^2$ elements. For m typically of the order of 100 the complete storage would require about 13 gigabyte. Fortunately most of the matrix elements are zero, and only the fraction of non-vanishing elements has to be stored. In step $\boxed{2.}$ the superblock can be constructed in two ways

a)

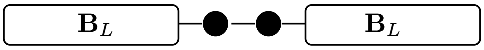

b)

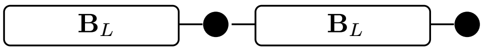

,

where B_L denotes an L-site subblock of the $(2L+2)$-system and $\bullet$ denotes a single site (s). Dealing with open boundary conditions the

---

[3] ρ is a $2\tilde{m} \times 2\tilde{m}$ matrix in the first iteration and a $2m \times 2m$ matrix in the subsequent steps.

superblock should be assembled as in a) to achieve a sparse Hamiltonian matrix $H_{\mathrm{B-s-s-B}}$. In the case of periodic boundary conditions (and nearest neighbor interactions only) a sparse Hamiltonian matrix can be achieved with configuration b) generating $H_{\mathrm{B-s-B-s}}$[4]. In the following a model with an alternating nearest neighbor exchange coupling is studied. Therefore one has to use configuration a) since configuration b) with two identical blocks is not compatible with the alternation. To minimize finite-size effects periodic boundary conditions are considered mostly in spite of the accuracy loss [4]. In particular for the calculation of energy gaps in the bulk limit periodic boundary conditions are necessary, since open boundary conditions can lead to excited states which are bound to the chain ends.

2.4 Finite Size Algorithm

The above iteration prescription is the so-called *infinite size* algorithm. The superblock is iteratively increased. Thus it is designed to calculate quantities in the thermodynamic limit. The algorithm can be extended improving the accuracy for the calculation of properties of a finite system with fixed size $\tilde{L}$. First one uses the *infinite size* algorithm until the superblock has the desired length $\tilde{L}$. In the subsequent iterations a superblock with fixed length $\tilde{L}$ is generated out of two subblocks with different lengths. If the left block represents a system of L sites two sites are added and the superblock is completed by connecting a ($\tilde{L}$-L-2)-site block

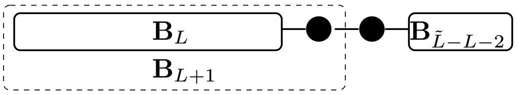

.

The Hamilton matrix and all other necessary operators of the ($\tilde{L}$-L-2)-site system have to be taken from a previous iteration. In each step one constructs the $\tilde{L}$ site superblock whereby the sizes of the subblocks vary

---

[4] The Hilbert space of the superblock is the direct product of the four subspaces corresponding to B, s, B, s. The sparseness of the Hamiltonian matrix of the superblock is greatly reduced, if the two B blocks are directly connected, since the corresponding block matrices contain many nonzero elements.

from some starting length L_{min} to $\tilde{L}$-L_{min}-2. This procedure, which is called a *sweep* through the lattice, can be repeated in that way, that the right subblock is increased in each step whereas the left part is taken from a previous iteration. The superblock configurations in the different iterations are depicted in the following sketch:

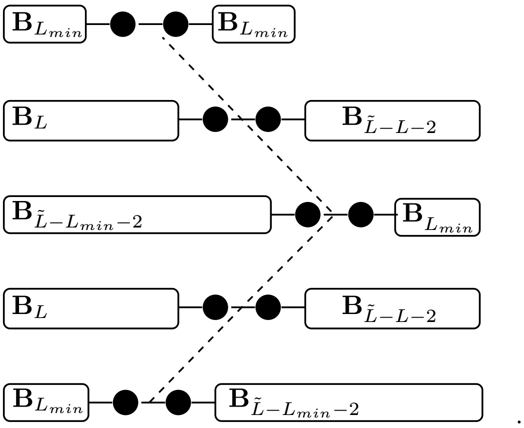

In the first step the *infinite size* algorithm is used to iteratively enlarge the $2L_{min}+2$ superblock until the desired length $\tilde{L}$ is reached. The remaining steps are part of the *finite size* algorithm, i.e. a sweep through the system. Usually two or three sweeps are sufficient and the accuracy does not discernibly increase on further sweeps[5]. The gain of accuracy, however, requires a longer runtime due to the additional sweeps and a larger amount of memory. In each step all operators corresponding to the L-site subsystem have to be stored, since they are needed in a subsequent iteration to complete the superblock.

The *finite size* algorithm is particularly suited for treating systems which are not translationally invariant. For instance, in chapter five it will be applied to modulated systems with periodicities of the order

---

[5] One might ask, why the accuracy increases at all, since in section 2.2 an *optimum* selection criterion has been formulated for the selection of the basis states. However, one has to bear in mind that in the first steps of the finite size algorithm a superblock of smaller length $(2L+2)$ is used to generate the density matrix and not the superblock of the desired length $\tilde{L}$.

of one hundred sites. In the first steps the *infinite size* algorithm is used, i.e. the reflection of the left hand block is taken to build up the superblock, irrespective of the fact that reflection symmetry is not given at this stage. This initial error is reduced either by supplementary sweeps through the system of the desired length or by intermediate sweeps through the system the length of which is commensurable with the lattice modulation.

2.5 Expectation Values

For the computation of expectation values $\langle A\rangle$ one must keep track of the corresponding operator which is to be 'measured'. In each iteration one has to construct the matrix $A_{\mathrm{B-s-s-B}}$ ($A_{\mathrm{B-s-B-s}}$) of the operator under study from the operator $A_{\mathrm{B-s}}$ of the $(L+1)$-site subsystems. In the *finite size* algorithm the expectation value is usually computed in the symmetric configuration of the last sweep, i.e. when both subblocks are of equal length $L = \tilde{L}/2-1$. The expectation value of the $\tilde{L}$-site system is simply given by

$$\langle\psi|A_{\mathrm{B-s-s-B}}|\psi\rangle = \sum_{i',j',i,j} \psi_{i',j'} A_{i',j',i,j} \psi_{i,j} \tag{2.16}$$

where $|\psi\rangle$ is the ground state computed within the diagonalization in step $\boxed{3.}$.

For expectation values of products $\langle AB\rangle$, where A and B are operators acting on different sites[6] in the same block one should not use

$$\langle\psi|A_{\mathrm{B-s-s-B}}B_{\mathrm{B-s-s-B}}|\psi\rangle = \sum_{\tilde{i},\tilde{j},i',j',i,j} \psi_{i',j'} A_{i',j',\tilde{i},\tilde{j}}\, B_{\tilde{i},\tilde{j},i,j} \psi_{i,j} \tag{2.17}$$

since the sum over $\tilde{i},\tilde{j}$ does not run over a complete set of states due to the truncation. To calculate this correlation function one has to keep track of the product (AB) and use Eq. (2.16) or one has to use operators which act in different blocks.

---

[6] In section 5.2.1, for instance, A and B are the z-components $S^z_{\tilde{i}}$, $S^z_{\tilde{j}}$ of two spins 1/2 on different sites ($i \neq j$).

2.6 Multiple Target states

Instead of targeting one state e.g. the ground state of the superblock, one can also focus on several low lying states. This is necessary, for instance, if the system is in a mixed state. In that case the density matrix of a subsystem is the weighted sum of the different density matrices belonging to each target state. Of course, it is more accurate to focus only on a single target state because then all selected basis states are specialized for its representation, whereas in the case of several target states only a fraction of the truncated basis is designed to represent each target.

2.7 Conserved Quantities

Conserved quantities can be used to reduce the numerical effort. As mentioned above, in the framework of this thesis properties of spin-1/2 Heisenberg chains are investigated. Here, the most important quantum number is the z component of the total spin, S^z_{total}. The parity, which is conserved if the superblock is reflection symmetric with respect to the middle bond, is of minor importance.

Because of the block structure of the superblock Hamiltonian only the matrix block corresponding to one particular S^z_{total} (e.g. $S^z_{total} = 0$ for the ground state) has to be generated and diagonalized. Of course this saves an enormous amount of memory and time in comparison to the treatment of the complete Hamiltonian. For the construction of $H_{\mathrm{B-s-s-B}}$, restricted to the subspace with $S^z_{total} = \mathrm{const}$, one has to keep track of the quantum numbers $S^z_{\mathrm{B-s}}(i)$ of each basis state $|i\rangle$ of the B − s subsystem.

The parity is conserved using the superblock configuration B − s − s − B in the *infinite size* algorithm. In the case of periodic boundary conditions and the B − s − B − s configuration, one can exploit the invariance of the system under the translation of half the system size. In both cases this yields a reduction of the dimension of the Hilbert space by a factor of roughly 2. In the *finite size* method neither of these symmetries is fulfilled due to the non-symmetric superblock construction in the intermediate steps.

2.8 Computation of Energy Gaps

In this thesis the DMRG algorithm is often used for the calculation of energies of excited states. The derived energy gaps are of particular interest because they are relatively easy to compute and they can be directly compared to excitation energies measured in experiments.

Without an external magnetic field the ground state of an antiferromagnetic spin chain is a spin singlet. Thus only the $S^z_{total}=0$ subblock of the superblock matrix $H_{\mathrm{B-s-s-B}}$ has to be considered. Analogously, the $S^z_{total}=1$ subspace has to be considered for studying a triplet excitation. In either case the target state which has to be chosen is the lowest lying state in the corresponding subspace. It is, however, more tedious to find the target state for the first singlet excitation since only S^z_{total} but not S_{total} can be fixed with moderate numerical effort in the course of the DMRG calculation. One way to distinguish the singlet state from the triplet state with $S^z_{total}=0$ is to apply S^+_{total} onto the possible target states (trial states). The second lowest state with $S^+_{total}|\psi_{trial}\rangle \approx 0$ is the state which has to be targeted to find the first excited singlet state. The price one has to pay is that an additional operator has to be generated and has to be stored in each step. A simpler but less reliable way is to extrapolate the actual energy from the previous iterations (or from exact Lanczos data in the first steps) and to select the state the energy of which is closest to the extrapolation.

Moreover, the computation of dispersion curves is desirable. Unfortunately, a straightforward calculation by means of the DMRG algorithm is impossible, because the momentum q is not conserved in the course of the iterations[7].

---

[7] This difficulty has partly been overcome by Hallberg [16] and by Kühner–White [17] combining the DMRG with the continuous fraction expansion of Green functions. Some details concerning this approach are given in appendix A.

2.9 Accuracy Considerations

The overall DMRG error depends crucially on the number of states which are kept in each iteration and on the system size (number of iterations). Additionally it depends on the model which is under study, in particular it depends on the range of interactions and on the boundary conditions. Highest accuracy is obtained if the number of connections (interactions) between the block which is renormalized and the rest of the superblock is minimal. In the *infinite size* algorithm this is due to the fact that the rest of the superblock, the reflected block, is supposed to approximate the rest of the infinite chain. For example in the case of the XY-model for $L = 102$ the truncation error of the ground state energy per site is smaller than 10^{-9} for open boundary conditions, while it is of the order of 10^{-5} for periodic boundary conditions keeping $m = 128$ states in either case. In the latter case there are two connections between the block and its reflection whereas there is only one connection in the first case applying open boundary conditions.

As another test of precision the triplet excitation gap Δ_{01} in the Majumdar-Ghosh model [18] is calculated. Due to the simple singlet-product structure of the ground state its energy per site, $e_0 = -0.375J$, is known exactly. For the same reason the value is also reproduced exactly within the DMRG method. This does not hold for the first excited state. The DMRG approach is a variational method due to the basis truncation in the iteration procedure and the energy of the first excited state is overestimated. Hence, the DMRG yields an upper bound for the excitation gap. The numerical results for Δ_{01} extrapolated to $L \to \infty$ for various numbers of states kept are given in Tab. 2.1. The analytical value was calculated by means of a perturbative approach extrapolated to infinite order using an analytical Lanczos technique [20].

The accuracy of the numerically derived excitation gap is much lower in comparison to the result for ground state energy of the XY-model in the thermodynamic limit. This is due to the complicated structure of the excited state (no product state) and the large next-nearest neighbor interaction which is present in the Majumdar-Ghosh model.

# states	Δ_{01}
45	0.2417
60	0.2398
70	0.2368
80	0.2364
90	0.2358
100	0.2352
128	0.2344
140	0.2343
160	0.2342
180	0.2341
extrapolation	$0.2339 \pm 2 \cdot 10^{-4}$
analytic	0.23386(3)

Table 2.1: Triplet excitation gap Δ_{01} of the Maumdar-Ghosh model in the bulk limit for various numbers of DMRG-states. The lowest value is analytically derived (see text).

2.10 Implementation

The DMRG algorithm is implemented using the object oriented programming language C^{++}. Time intensive algebraic matrix and vector operations are done by means of the LAPACK (Linear Algebra PACKage) and the BLAS (Basic Linear Algebra Subroutines) libraries which are implemented in the *Sun Performance Library.* The source code is about 4000 lines. On the one hand, the program is designed to achieve a good performance while on the other hand, it is designed to be applicable to various problems such as the calculation of higher excitations and self-consistent calculations for models with various interactions.

Most calculations have been performed on SUN workstations at the *Institut für Theoretische Physik der Universität zu Köln.* For several calculations the *SUN Ultra Enterprise 10000* and the *SUN Ultra Enterprise 4500* at the *Regionales Rechenzentrum der Universität zu Köln* have been used.

Besides some general basic classes such as matrix/vector operations the program includes several DMRG-specific classes within a certain hierarchy. The modular structure of the program improves the clarity and facilitates possible modifications and extensions.

The DMRG-specific classes are:

Site contains the matrices to model a single site (here the spin matrices: S^+, S^- and S^z).

Edge contains two *Sites*. The last and the last but one *Site* are needed, to connect an *Edge* with another *Block*.

Block contains two *Edges* (right and left), the Hamilton matrix of the block and several functions, e.g. for connecting two blocks or for basis transformations.

Superblock contains the Hamilton matrix of the superblock and the routines to generate it (see below). To save memory only nonzero matrix elements are stored. Such matrices are covered by the class *SparseMatrix*. The matrix can either be kept in memory or can be stored on hard disk. Furthermore *Superblock* contains the diagonalization routine (see below).

Target contains the target state(s) and routines to calculate the desired expectation values. In addition it contains the density matrix (2.5), the deduced transformation matrix U (2.15) and the generating routines.

Before the superblock Hamiltonian is generated by a member-function of the class *Superblock*, the basis states of the left and right subblock, which in combination have the proper quantum number S^z_{total}, are selected. The indices of the selected states are stored in two integer arrays corresponding to the left and right subblock. Constructing the Hamiltonian these arrays are used for addressing the selected states.

After the construction of the Hamiltonian $H_{\mathrm{B-s-s-B}}$ or $H_{\mathrm{B-s-B-s}}$ of type *SparseMatrix* the Davidson algorithm [13] is used for the matrix diagonalization. The start vectors can either be chosen randomly or can be derived from the previous target state. This often leads to a slightly smaller number of necessary iterations within the Davidson routine.

The density matrix, which is a member of *Target* has block structure, corresponding to the various S^z sectors. The blocks are diagonalized one by one. This does not save much time but it is a convenient way to keep track of the S^z quantum numbers of the selected states which build the transformation matrix U.

A sketch of the hierarchic structure and of the interdependence of the various classes is shown in Fig. 2.1.

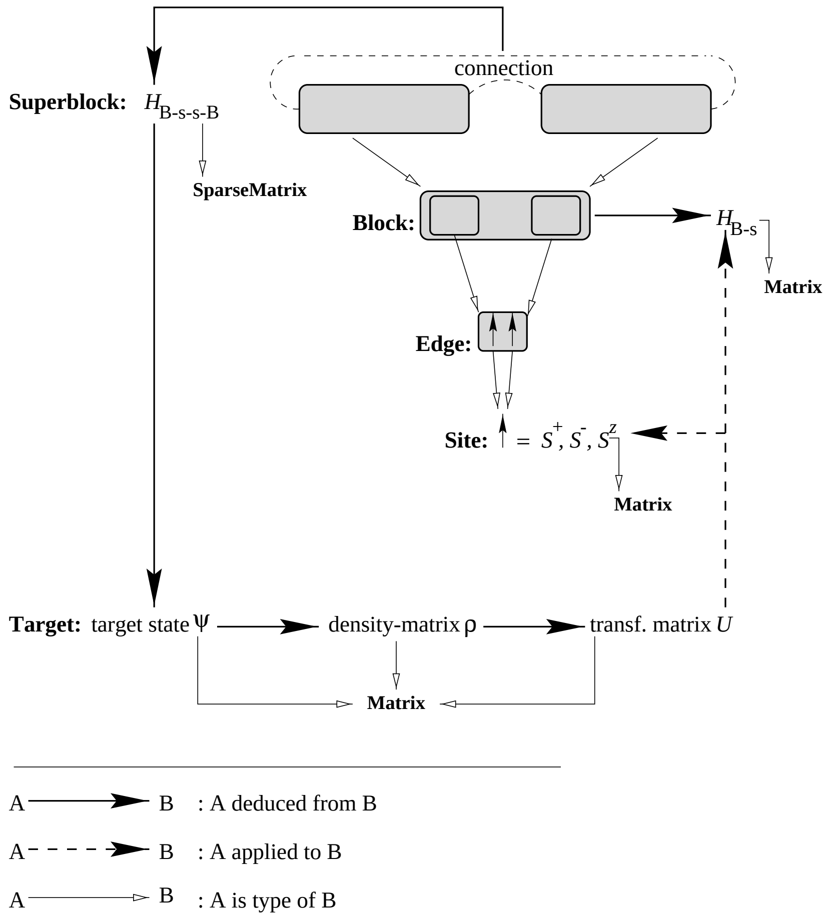

Figure 2.1: Schematic diagram showing the interdependence of the various classes. The relevant class names (bold) are followed by the class members which are important for illustrating the program structure. The class members are depicted by symbols and/or letters. The explanations for the three different arrow types are given at the bottom.

Chapter 3

Transfer-Matrix DMRG

The DMRG algorithm as it is discussed in chapter 2 is applicable to investigate the low energy physics of quantum systems. Although it is possible to focus on multiple target states one cannot treat finite temperatures since too many excited states have to be regarded. The recently developed transfer-matrix DMRG (T-DMRG), however, overcomes this difficulty and is particularly suited for this task [5–7].

3.1 T-DMRG Algorithm

In the following the T-DMRG method is outlined which is used in the last part of this thesis for studying the finite temperature behavior of dimerized, frustrated Heisenberg chains. For the sake of concreteness the Hamiltonian is explicitly given below. It is formally motivated later on in the following chapter.

$$\begin{aligned}
\hat{H} &= \sum_{i=1}^{N} \hat{h}_i \,, \qquad \text{with} \qquad\qquad (3.1)\\
\hat{h}_i &= \{(1+\delta)\,\mathbf{S}_{i,1}\cdot\mathbf{S}_{i,2} + (1-\delta)\,\mathbf{S}_{i,2}\cdot\mathbf{S}_{i+1,1} \\
&\qquad + \alpha\,\mathbf{S}_{i,1}\cdot\mathbf{S}_{i+1,1} + \alpha\,\mathbf{S}_{i,2}\cdot\mathbf{S}_{i+1,2}\}\,J \\
&\quad + g\mu_B H(S^z_{i,1} + S^z_{i,2}) \,,
\end{aligned}$$

where $\mathbf{S}_{i,j}$ denotes spin 1/2 operators referring to the jth spin in the ith cell. The parameters J, δ, α stand for the exchange coupling, the

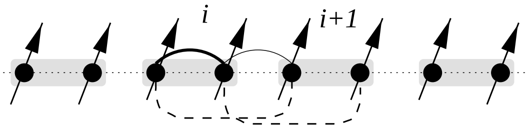

Figure 3.1: Sketch of a dimerized, frustrated Heisenberg chain. The bold line denotes the strong nearest neighbor interaction $J(1+\delta)$, the thin line the weak nearest neighbor interaction $J(1-\delta)$ and the bold dashed lines denote the frustrations αJ. The interactions shown are those which are covered by the local Hamiltonian $\hat{h}_i$ (see text). The shaded areas indicate the two-site cells.

dimerization and the relative frustration, respectively. The last term in $\hat{h}_i$ describes the Zeeman energy in presence of an external magnetic field H. The local Hamiltonian $\hat{h}_i$ is graphically depicted in Fig. 3.1.

In the representation used in Eq. (3.1) two spins are grouped together to achieve a translationally invariant description of the system. The translation invariance is essential for the applicability of the transfer-matrix method. A similar strategy was adopted in Ref. [21] to cast a system with next-nearest neighbor interaction into a form suitable for application of the T-DMRG algorithm.

To apply the Trotter-Suzuki formula we first decompose the Hamiltonian (3.1) into two parts $H_{e(o)}$ which contain the sum over even (odd) cells. After checkerboard decomposition [22] of the effective four state problem the partition function is calculated by means of the quantum transfer-matrix T_M [22, 23],

$$Z = \lim_{M\to\infty} \mathrm{tr}\left[\mathrm{e}^{-\epsilon H_o}\mathrm{e}^{-\epsilon H_e}\right]^M = \lim_{M\to\infty} \mathrm{tr}\, T_M^{N/2} , \tag{3.2}$$

where $\epsilon = \beta/M$, $\beta = 1/T$ and M is the Trotter number. To derive T_M one has to rewrite Eq. (3.2) inserting $2M$ complete sets of eigenstates,

$$|\alpha_i\rangle = |\sigma_i^1\rangle \otimes |\sigma_i^2\rangle \otimes \cdots \otimes |\sigma_i^N\rangle , \tag{3.3}$$

where the upper index labels the cells and the lower index ($1 \le i \le 2M$) labels the so-called Trotter slices. $|\sigma_i^j\rangle$ stands for a complete basis set of the jth cell with Trotter index i (see below). The insertion leads to

$$\begin{aligned} Z = \sum_{\alpha_1,\alpha_2,\cdots\alpha_{2M}} & \langle\alpha_1|\mathrm{e}^{-\epsilon H_o}|\alpha_2\rangle \times \\ & \langle\alpha_2|\mathrm{e}^{-\epsilon H_e}|\alpha_3\rangle\langle\alpha_3| \cdots |\alpha_{2m}\rangle\langle\alpha_{2m}|\mathrm{e}^{-\epsilon H_e}|\alpha_1\rangle \,. \end{aligned} \tag{3.4}$$

Each factor $\langle\alpha_i|\mathrm{e}^{-\epsilon H_{o/e}}|\alpha_{i+1}\rangle$ factorizes into $N/2$ local terms. Comparing Eq. (3.2) with the right hand side of Eq. (3.4) one finds, that the quantum transfer-matrix T_M can be written as a sum, the summands of which factorize into local transfer-matrices τ [7]:

$$\begin{aligned} &\langle\sigma_1^3 \cdots \sigma_{2M}^3|T_M|\sigma_1^1 \cdots \sigma_{2M}^1\rangle = \\ &\qquad \sum_{\{\sigma_k^2\}} \prod_{k=1}^{M} \tau(\sigma_{2k-1}^3\sigma_{2k}^3|\sigma_{2k-1}^2\sigma_{2k}^2)\tau(\sigma_{2k}^2\sigma_{2k+1}^2|\sigma_{2k}^1\sigma_{2k+1}^1)\,, \end{aligned} \tag{3.5}$$

$$\text{with} \qquad \tau(\sigma_k^{i+1}\sigma_{k+1}^{i+1}|\sigma_k^i\sigma_{k+1}^i) = \langle s_{k+1}^{i+1}, s_{k+1}^i|\mathrm{e}^{-\epsilon\hat{h}_i}|s_k^i s_k^{i+1}\rangle\,,$$

where $|\sigma_k^i\rangle = (-1)^{i+k}|s_k^i\rangle$ and $|s_k^i\rangle$ is an eigenstate of S_i^z. As denoted above, the superscripts and subscripts of σ and of $|s\rangle$ represent the coordinates of spins in real and Trotter space, respectively. Periodic boundary conditions are imposed in the Trotter direction, i.e.

$$\tau(\sigma_{2M}^2\sigma_{2M+1}^2|\sigma_{2M}^1\sigma_{2M+1}^1) = \tau(\sigma_{2M}^2\sigma_1^2|\sigma_{2M}^1\sigma_1^1).$$

The local Hamiltonian $\hat{h}_i$ conserves the total spin in the cells i and $i+1$. In Trotter space (σ-basis) this translates into $\sigma_k^i + \sigma_{k+1}^i = \sigma_k^{i+1} + \sigma_{k+1}^{i+1}$ and leads to block diagonal matrices τ.

In the thermodynamic limit $N \to \infty$ the trace in the partition function Eq. (3.2) equals

$$Z \;= \mathrm{Tr}\, T_M^{N/2} \;= \sum_i \lambda_i^{N/2}\,,$$

where λ_i are the eigenvalues of T_M,

$$= \lambda_0^{N/2}\left\{1 + \left(\frac{\lambda_1}{\lambda_0}\right)^{N/2} + \left(\frac{\lambda_2}{\lambda_0}\right)^{N/2} + \cdots\right\},$$

which reduces to

$$\overset{N\to\infty}{=} \lambda_0^{N/2}\,, \tag{3.6}$$

if λ_0 denotes the maximum eigenvalue. Hence, thermodynamic properties are determined solely by the maximum eigenvalue λ_0 and the corresponding left and right eigenvectors ($\langle\psi^l|$ and $|\psi^r\rangle$) of T_M. For the Hamiltonian (3.1) the maximum eigenvalue lies in the subspace with $\sum_k \sigma_k^i = 0$ [24].

The remaining task is to calculate λ_0 in the limit $M \to \infty$. This can be done by iterative augmentation in Trotter direction, which is achieved by applying the DMRG idea. To illustrate how White's DMRG idea can be applied in this context it is useful to switch to a graphic representation. First τ is identified with the square:

$$\tau(\sigma_{k-1}^{i+1}\sigma_k^{i+1}|\sigma_{k-1}^{i}\sigma_k^{i}) =$$

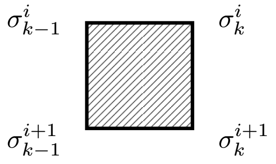

.

In this representation the quantum transfer-matrix T_M (3.5) is equal to

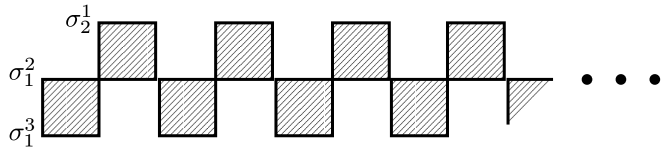

,

where the sum over $\{\sigma_k^2\}$ $(k=1,\dots,M)$ is represented by the shared corners. For each Trotter number M the quantum transfer-matrix T_M is identified with a superblock as introduced in the previous chapter. For even M the superblock can be constructed from two identical subblocks, e.g.

$$T_4 =$$

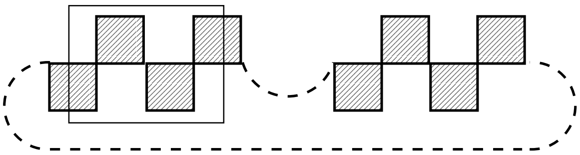

,

where the dashed lines indicate the additional summations for generating the superblock with periodic boundary conditions in Trotter space.

For M odd one has to use two different subblocks, e.g.

$T_5 =$

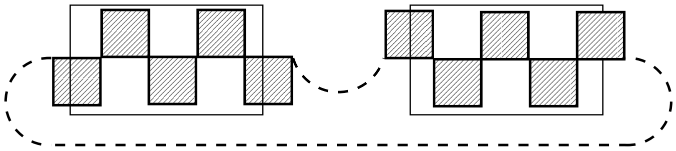

In the iteration process the framed parts of the subblocks are renormalized, i.e. they are transformed onto a truncated basis. Afterwards these blocks are enlarged by adding a local matrix τ.

Since T_M, which can be chosen to be real, is not symmetric one needs the left *and* the right eigenvector ($\langle\psi^l|$, $|\psi^r\rangle$) of the largest eigenvalue to generate the density-matrix. In the non-symmetric case the density-matrix (cf. Eq. (2.5)) is defined as [6]

$$\rho(i,i') = \sum_j \psi^l_{i,j}\psi^r_{i',j} \,, \tag{3.7}$$

where i, i' label the basis states of the part which is renormalized and j labels the basis states of the rest of the superblock. Applying the *infinite size algorithm*, basically the same iteration prescription is used as given in chapter 2. But, as indicated above, the system is increased iteratively in the Trotter direction.

In the calculation $\epsilon = 1/TM$ is to be fixed (cf. Eq. (3.2)). Hence, the incrementing Trotter number corresponds to a reduction of the temperature. Therefore, in the course of the iterations, thermodynamic properties are directly accessible as a function of temperature. The free energy, for instance, is determined by the maximum eigenvalue $f = -(T/4)\ln\lambda_0$. From the derivatives of f one can, in principle, calculate the internal energy u and other quantities of interest. However, as it is difficult to evaluate the derivatives of f accurately it is more precise to evaluate expectation values using the eigenstates $\langle\psi^l|$, $|\psi^r\rangle$. The internal energy per site, for instance, is given by

$$u = \langle\hat{H}\rangle_T/N = \langle\hat{h}_i\rangle_T = \langle T_{h_i}\rangle/\lambda_0 \,, \tag{3.8}$$

where $\langle\rangle_T$ denotes the thermal average. The definition of T_{h_i} is similar to that of T_M (3.5), however, for instance $\tau(\sigma_2^2\sigma_3^2|\sigma_2^1\sigma_3^1)$ is replaced by

$\tau_{h_1}(\sigma_2^2\sigma_3^2|\sigma_2^1\sigma_3^1) = \langle s_3^2, s_3^1|\hat{h}_1 \mathrm{e}^{-\epsilon\hat{h}_1}|s_2^1 s_2^2\rangle$ [6]. Similarly one finds the magnetization $m_z = \langle\sum \hat{S}_i^z\rangle_T/N$. The specific heat and the susceptibility are obtained by means of the corresponding derivatives.

3.2 Implementation

The finite temperature DMRG algorithm is implemented[1] in the programming language C^{++}. The source code is about 2000 lines. The main focus is put on the performance.

The largest eigenvalue of the non-symmetric matrix T_M together with the left and right eigenvector is calculated by means of a power algorithm [25]. More delicate, however, is the diagonalization of the density-matrix (3.7), which is not symmetric either, since all eigenvalues have to be calculated to find the m largest ones. In the course of the program-development this step turned out to be crucial. The numerical errors of the eigenstates which form the transformation matrix U accumulate throughout the DMRG iterations and can dramatically affect subsequent iterations. After a certain number of iterations the accumulated error can lead to complex eigenvalues of the density-matrix ρ. A proper numerical treatment of these unphysical results is not clear. The problem, however, can be circumvented or at least postponed to later iterations by minimizing the errors of the eigenstates of ρ. This is achieved using a higher precision within the diagonalization of ρ, which is performed with the help of *MAPLE.*

The elements of the subblocks of the density-matrix and the *MAPLE* code itself are piped into *MAPLE* by the main program. After the diagonalization and the selection of the most important states by the *MAPLE* routine the selected eigenvectors are stored on hard disk. A flag-file signals that the *MAPLE* program has finished and the main program resumes control. The vectors are read in and are used for the basis transformation (truncation) of the subsystems. Eventually a new transfer-matrix T_M is constructed from the transformed and enlarged subblocks.

---

[1] The code has been written together with Rainer Raupach.

Chapter 4

$CuGeO_3$

The lattice structure of $CuGeO_3$ was already analyzed in 1954 by Ginetti [26]. However, only the discovery of this compound to be the first inorganic spin-Peierls (SP) system by Hase *et al.* [1] in 1993 has led to a pronounced interest in this quasi one dimensional spin system.

Due to the high quality of the $CuGeO_3$ crystals and due to the anorganic composition intensive experimental studies, e.g. neutron or X-ray scattering, can be performed. The lattice structure which is simpler than the ones of the previously known organic SP compounds [27] facilitates a detailed theoretical understanding of the observed structural phase transition. In addition this inorganic compound can easily be doped. For instance, one observes that the substitution of a small fraction of Cu by Zn/Mg or of Ge by Si leads to a dramatic reduction of the transition temperature [28, 29].

4.1 Structure and Model

The crystal structure of $CuGeO_3$ is displayed in Fig. 4.1. The magnetic properties of $CuGeO_3$ which are responsible for the SP transition arise from spin 1/2 moments of the Cu^{2+} ions. The copper ions are located in the middle of CuO_4 plaquettes which are arranged in chains along the c-direction sharing a common edge. The plaquettes form the basis planes of CuO_6 octahedra which are arranged along the b-direction

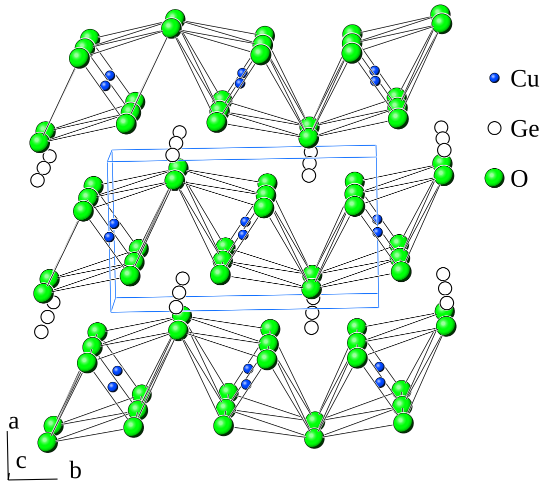

Figure 4.1: Crystal structure of $CuGeO_3$ [30]. The spin 1/2 Cu^{2+}-chains are along the *c*-direction.

sharing a common oxygen atom as depicted in Fig. 4.1. The second basis component of $CuGeO_3$ are GeO_4 tetrahedra which reside between the octahedron-planes (*b*- ,*c*-directions).

The dominant magnetic intrachain coupling between Cu^{2+} moments in $CuGeO_3$ arises from superexchange via the bridging oxygens of the common edges. Although the Cu-O-Cu bond angle is almost 90° and therefore expected to be ferromagnetic by the Goodenough–Kanamori rules, side group effects due to the hybridization of O and Ge orbitals lead to a small effective antiferromagnetic (AF) exchange interaction [31]. Furthermore, the Cu-O-O-Cu exchange paths lead to an additional sizeable next–nearest neighbor AF exchange coupling which frustrates the magnetic interaction between the Cu^{2+} spins [32].

The magnetic interchain coupling can be estimated from the dispersion of the magnetic excitations perpendicular to the chains to be an order of magnitude smaller than the intrachain exchange [33–35]. Hence, a 1-d approach for modeling the magnetic properties of $CuGeO_3$ seems to be justified. To model the low energy physics, magnetic and elastic degrees of freedom have to be taken into account. One may use the following Hamiltonian, where the spin-phonon coupling enters via the phonon dependent spin-spin interaction $J(\vec{u}_i, \vec{u}_{i+1})$:

$$\hat{H} = \sum_{i=1}^{L} \Big\{ J\left(\vec{u}_i, \vec{u}_{i+1}\right) \mathbf{S}_i \cdot \mathbf{S}_{i+1} + \alpha\, J\, \mathbf{S}_i \cdot \mathbf{S}_{i+2} \Big\} + \sum_{\vec{q}} \omega_{\vec{q}}\, b^{\dagger}_{\vec{q}} b_{\vec{q}} \,. \quad (4.1)$$

In this formula i denotes the sites of a chain with length L, $\mathbf{S}_i$ are $S = 1/2$ spin operators and αJ denotes the frustration, i.e. the exchange interaction between next-nearest neighbor spins. The operator $b^{\dagger}_{\vec{q}}(b_{\vec{q}})$ creates (annihilates) a phonon with momentum $\vec{q}$. Here, only one phonon mode is assumed to be SP-active. A detailed discussion including four relevant phonon modes can be found in Ref. [36]. The displacement of the jth atom in terms of the phonon operators is given by

$$\vec{u}_j = \sum_{\vec{q}} \sqrt{\hbar/(2Nm\omega_{\vec{q}})}\, \mathrm{e}^{i\vec{q}\vec{R}_j}\, \vec{e}_{\vec{q}} \left(b_{\vec{q}} + b^{\dagger}_{-\vec{q}}\right) , \quad (4.2)$$

where m is the effective mass, N the number of elementary cells, $\vec{R}_j$ denotes the equilibrium position and $\vec{e}_{\vec{q}}$ the polarization vector. For the numerical investigation the Hamiltonian (4.1) is simplified treating the phonons in mean-field approximation, i.e. the $\vec{u}_j$ are replaced by their expectation values. Furthermore only a single phonon mode with momentum close to π is presumed to be responsible for the SP transition and a linear dependence of the exchange integral on the atomic displacements is assumed. Then the site-dependent nearest neighbor exchange coupling $J(\vec{u}_i, \vec{u}_{i+1})$ reads

$$J(i) = J + \left(\langle u_i \rangle - \langle u_{i+1} \rangle\right) \gamma \ , \quad (4.3)$$

where γ is the spin-lattice coupling constant and J is the nearest neighbor exchange integral in the undistorted phase. Defining the dimensionless relative distortions $\delta_i = (\langle u_i \rangle - \langle u_{i+1} \rangle)\gamma/J$ the approximation of the Hamiltonian (4.1) reads

$$\begin{aligned}
\hat{H} &= \hat{H}_{\text{chain}} + E_{\text{elast}} \ , \qquad (4.4)\\
\hat{H}_{\text{chain}} &= \sum_{i=1}^{L} \{J(i)\mathbf{S}_i \cdot \mathbf{S}_{i+1} + J\alpha\, \mathbf{S}_i \cdot \mathbf{S}_{i+2}\} \ ,\\
E_{\text{elast}} &= \frac{K_0}{2}\sum_i \delta_i^2 \ ,
\end{aligned}$$

where the last term is the elastic energy which is associated with the static lattice distortion. The exchange interaction $J(i)$ and the spring constant K_0 are given by

$$J(i) = J(1+\delta_i) \quad \text{and} \quad K_0 = \frac{J^2\omega_{\vec{q}}^2 m}{2\gamma^2} \ .$$

In addition, the Zeeman energy

$$\hat{H}_{\text{Zeeman}} = g\mu_{\text{B}} H S^z \qquad (4.5)$$

has to be taken into account in presence of an applied external magnetic field H, where S^z denotes the total magnetization $\sum S_i^z$.

The mean-field treatment of the phononic degrees of freedom is equivalent to an adiabatic approximation assuming a static lattice distortion. The justification of the adiabatic treatment is *a priori* not given in contrast to the case of the organic SP compounds [37]. In $\mathrm{CuGeO_3}$ the energy scale of the phonons involved in the SP transition is not separated from the magnetic energy scale [38, 39]. However, in the course of this thesis it turns out that many of the experimentally observed features of $\mathrm{CuGeO_3}$ can be understood within the one-dimensional adiabatic approach.

4.2 Spin-Peierls Transition

The SP transition in $\mathrm{CuGeO_3}$ is a *three*-dimensional structural phase transition. It is, however, the *one*-dimensional spin system ($\mathrm{Cu^{2+}}$ chains) the transition is driven by.

The most favorable state for two antiferromagnetically coupled spins is the singlet. Hence, there is a certain tendency in the spin system to from singlet pairs between the strongly coupled nearest neighbors. In the case of a 1-d system with the spin-spin interaction depending on the lattice degrees of freedom, this leads to dimerization, i.e. the magnetic system gains energy by the formation of singlet pairs on neighboring sites as depicted below:

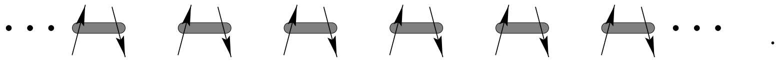

Due to the magneto-elastic coupling the singlet formation comes along with a lattice distortion leading to an alternating bond modulation along the chain. The loss of elastic energy which is associated with the lattice distortion is overcompensated by the magnetic energy gain.

The term *spin*-Peierls transition comes from the analogy to the Peierls transition in quasi one-dimensional metals. As in the case described above a metal with a half-filled conduction band exhibits an instability towards dimerization. Here, the lattice distortion leads to an alternation of the electron hopping and hence to a doubling of the unit cell and to a bisection of the first Brillouin zone. Driven by $2k_F$-interactions the half-filled electron band splits into a filled valence and an empty conduction band. These bands are separated by an energy gap. The opening of the gap leads to an energy gain of the electronic system. For non-interacting fermions the gain is proportional to $(\delta^2 \ln \delta)$, if δ describes the alternation of the hopping [40].

As in the case of the Peierls transition the magnetic energy gain which drives the *spin*-Peierls transition can be attributed to the opening of a gap Δ. For a uniform antiferromagnetic spin-1/2 system one finds a gapless excitation spectrum, a spinon continuum [41]. In the SP ordered phase the spin 1/2 moments form singlet dimers along the chains. The resulting singlet ground state is separated from the triplet excitations by an energy gap Δ. This energy gap is related to the amount of energy which is necessary to convert a single dimer of the singlet ground state into a triplet. In the case of a spin 1/2 Heisenberg chain the energy gain associated with the opening of the gap is proportional to $\delta^{4/3}$ and the gap itself is proportional to $\delta^{2/3}$ if δ denotes the strength of the alternation of the exchange coupling [42,43]. As mentioned before, this energy gain overcompensates the loss of elastic energy due to the lattice distortion, which is proportional to δ^2.

Experimentally, the SP transition and the opening of a spin gap is observed in inelastic neutron scattering (INS), magnetic susceptibility, X–ray scattering, and electron–diffraction experiments (for a review of the experiments concerning CuGeO$_3$ see [45]).

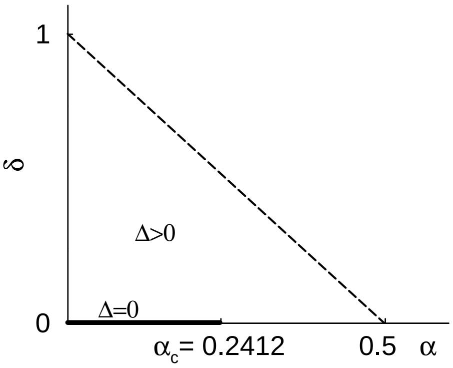

The general phase diagram of dimerized frustrated Heisenberg chains ($\hat{H}_{\text{chain}}$ in Eq. (4.4)) with dimerization $\delta_i = (-1)^i\delta$ is depicted in the right figure. As soon as a dimerization $\delta > 0$ is switched on the system is gapped. But also for $\delta = 0$ the ground state is dimerized for sufficiently large frustration due to spontaneous symmetry breaking, i.e. the formation of singlet pairs[1]. By numerical scaling analysis the critical frustration for $\delta = 0$ was found to be $\alpha_c \approx 0.2412$ [46–48]. For the special case $2\alpha + \delta = 1$ (dashed line) the ground state is known exactly. It is a product wavefunction of independent singlet dimers [18,19,49].

Furthermore, SP systems exhibit a rich phase diagram in applied magnetic fields. The phase diagram of CuGeO$_3$ in reduced units, which is generic for general SP-compounds, is shown in Fig. 4.2. With decreasing temperature, beside the transition from an undistorted uniform (U) phase to a collective non–magnetic singlet state with a dimerized (D) lattice as discussed above, a different transition occurs in sufficiently large magnetic fields. In this high field phase an incommensurate (I)

---

[1] In this context the meaning of *dimerized* or *dimerization* is twofold. On one hand it denotes the relative alternation of the exchange couplings $(-1)^i\delta$ and on the other hand it signifies the alternation of the expectation values $\langle \vec{S}_i \vec{S}_{i+1} \rangle$.

lattice modulation is found which is stabilized by the Zeeman energy.

In the following chapter fundamental properties of the D-phase are discussed. In chapter 6 the I-Phase and in particular the D-I transition are investigated. Both analysis are performed at zero temperature. In chapter seven the focus is put on the D-phase and the D-U transition at finite temperatures.

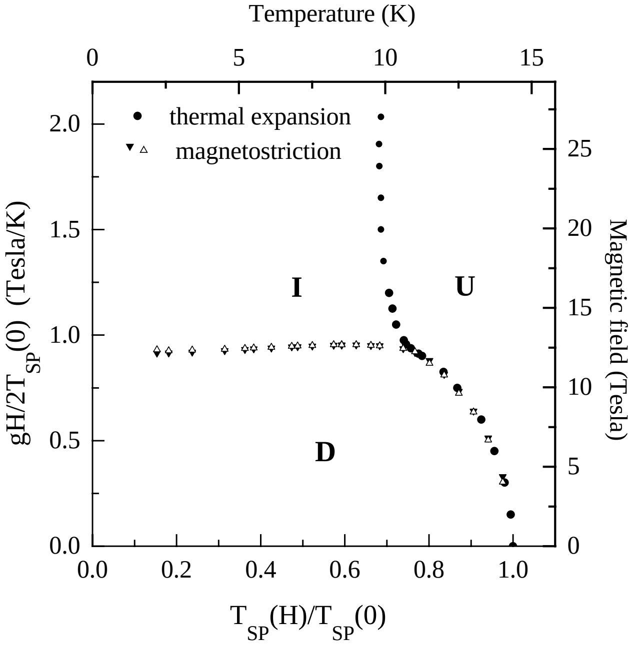

Figure 4.2: Experimental phase diagram of $CuGeO_3$. U: uniform (spin liquid) phase; D: dimerized phase; I: incommensurate phase.

Chapter 5

$CuGeO_3$ in Zero Magnetic Field

In this chapter properties of the D phase with the alternating lattice modulation $\delta_i = (-1)^i \delta$ are examined. In the first part the magnitude of the dimerization δ with respect to $CuGeO_3$ is determined with the help of the DMRG technique. The dimerization and the other model parameters are tested by comparing the calculated singlet excitation with the experimental findings from Raman scattering experiments. In addition the triplet excitation energy as a function of δ is analyzed beyond its relevance for $CuGeO_3$.

In the second part doped systems are considered. After a short introduction about general aspects of doped systems and how impurities can be incorporated in the present approach, particular attention is given to the distortion patterns and the antiferromagnetic correlations which develop in the neighborhood of dopants.

5.1 Model Parameter

5.1.1 Fixing of J and α

Before the dimerization δ is determined by means of the DMRG method the nearest and next-nearest neighbor exchange couplings J and αJ have to be fixed. Since these parameters are assumed to be only slightly affected by the structural lattice distortion for $T < T_{SP}$ they can be fixed in the U phase. A precise knowledge of both J and α is crucial to determine δ, since the gap-relation $\Delta(\delta)$ depends on them. In particular, there exists a critical frustration $\alpha_c \approx 0.2412$ [46–48] for a spin gap to develop due to spontaneous dimerization (cf. phase diagram on page 38). Several efforts have been made to determine J and α and to decide whether the gap observed in CuGeO$_3$ is partially a manifestation of spontaneous dimerization or not [48, 50, 51]. In each case the parameters J and α are derived by means of a two parameter fit of the magnetic susceptibility of CuGeO$_3$ in the U phase. Both, Riera *et al.* [50] and Fabricius *et al.* [51] come to the conclusion that $J \approx 160\,\mathrm{K}$ and $\alpha \approx 0.35$ provides a reasonable parameter set. Lanczos calculations of Bouzerar also verified that these parameters yield an extraordinarily good fit to the experimental susceptibility in the whole temperature range, $50\,\mathrm{K} < T < 1000\,\mathrm{K}$, using the g factor $g_b = 2.26$ as measured by ESR [52]. For the following investigations the constant elastic energy in Eq. (4.4) is neglected and only the spin part of the Hamiltonian, i.e.

$$\hat{H}_{\text{chain}} = J \sum_{i=1}^{L} \Big\{ (1 + (-1)^i \delta)\, \mathbf{S}_i \cdot \mathbf{S}_{i+1} + \alpha\, \mathbf{S}_i \cdot \mathbf{S}_{i+2} \Big\} \,, \tag{5.1}$$

is considered. As far as CuGeO$_3$ is concerned the values $J = 160\,\mathrm{K}$ and $\alpha = 0.35$ are used.

5.1.2 Determination of the Dimerization

Given J and α the dimerization parameter δ is fixed from the requirement that the excitation spectrum of Eq.(5.1) reproduces the low temperature value of the singlet–triplet gap (Δ_{01}) of about 25 K as measured by INS [33, 34][1] .

Using the *infinite size* algorithm (section 2.3) the ground state energies and the first excited energies are calculated for chains of about one hundred sites. The large system sizes allow to read off the values in the

---

[1] The gap corresponds to the minimum of the dispersions in c- *and* b-direction (cf. Fig. 4.1 and [35]). The effect of interchain coupling in CuGeO$_3$ can approximately be included by taking a mean gap, i.e. averaging the dispersion perpendicular to the chains along k_b, resulting in a larger gap of approximately 44 K (cf. sect. 6.2.2 and sect. 7.2).

infinity chain limit $L \to \infty$ directly. Iterating up to considerable longer chain lengths is not recommendable since finite-size effects are already almost absent for $L \approx 100$ but the overall DMRG error increases since a small truncation error enters in each step[2].

The energy as a function of δ for $\alpha = 0.35$ is shown in Fig. 5.1 (stars and bold line). One observes that the experimental gap value $\Delta_{01}^{exp}/J \approx 0.156$ is obtained for $\delta \approx 0.012$ [53]. In addition energy gap data for different frustrations are shown which will be discussed in section 5.1.4.

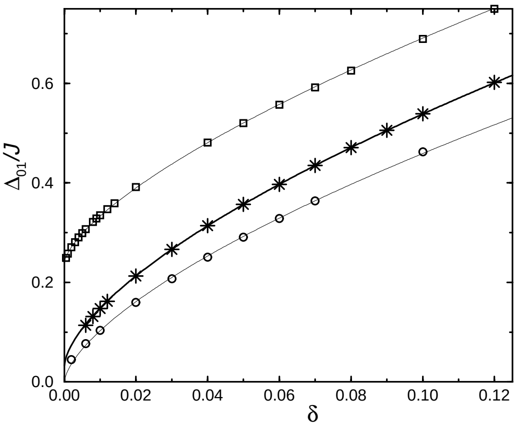

Figure 5.1: Triplet gap as a function of the dimerization δ for various values of the frustration α. Symbols are DMRG results; the solid lines are simple power law fits $\Delta_{01} \approx \Delta_{01}(\alpha) + a\delta^{\nu}$ with three different parameter sets (α,$\Delta_{01}(\alpha)$,ν): circles (0.241, 0, 0.65), stars (0.35, 0.033, 0.642), squares (0.5, 0.24, 0.685).

Having determined the dimerization δ in the D phase using the interactions J, α determined in the U phase one may ask whether there is an independent parameter check of the validity of the derived parameter set. Indeed, the internal consistency of the model parameters can

---

[2] The actual number of iterations depends on the values of δ and α or, more precisely, on the resulting correlation length and on the number of states which are kept.

be verified by exploring the consequences for the Raman spectrum.

5.1.3 Singlet–Singlet Gap Δ_{00}

For the parameter check we focus on the lowest singlet–singlet gap Δ_{00} which can be seen as a sharp peak in the experimental Raman spectra [54–58]. Since Raman light scattering measures the singlet excitations [59] it is to some extent complementary to INS from which the dispersion of the triplet excitation has been obtained. On cooling below T_{SP} additional peaks appear in the Raman spectrum. The lowest Raman excitation in the dimerized phase is observed at $30\,\mathrm{cm}^{-1}$, i.e. slightly below $2\Delta_{01}$ [54–58]. This excitation energy has to be compared to the result one derives in the present model choosing the parameters denoted above.

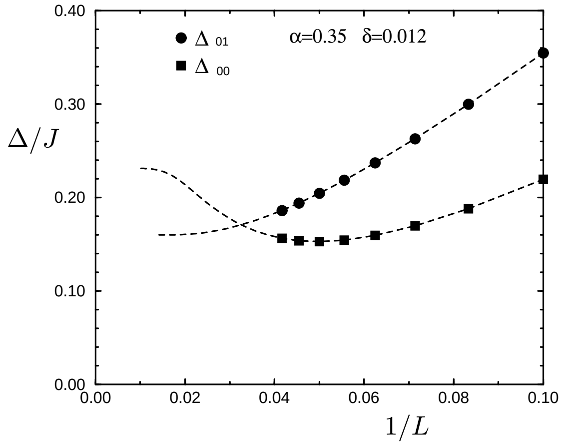

Figure 5.2: Singlet–triplet gap Δ_{01} and singlet–singlet gap Δ_{00} as a function of the inverse system size $1/L$. The symbols are exact Lanczos results and the dashed lines DMRG results [53].

Fig. 5.2 shows the singlet–singlet gap Δ_{00} and also the singlet–triplet gap Δ_{01} as a function of $1/L$ for the fixed parameter set. The symbols depict exact Lanczos diagonalization results for chains up to 24 sites from Bouzerar *et al.* [53] and the dashed lines show the DMRG data for $L \leq 100$. Both data sets are in excellent agreement for $L \leq 24$ confirming the accuracy of the DMRG results. Obviously, Δ_{00} shows an unusual non-monotonous scaling behavior. As a finite size effect for short chains, the lowest singlet appears below the triplet excitation. This has already been noted by Riera *et al.* [60]. Due to the non-monotony of $\Delta_{00}(L)$, however, the extrapolation to the thermodynamic limit is rather delicate and requires the knowledge of the correct scaling function which is not known in this case.

The DMRG method is particularly suited for this problem, since L can be increased such that the thermodynamic limit is reached and the singlet gap can be read off directly. It is found to be $\Delta_{00} \approx 0.232J$. Obviously $\Delta_{00} \leq 2\Delta_{01}$ holds and Δ_{00} is close to but approximately 13% below the experimental result for the lowest Raman excitation energy $\Delta_{00}^{exp} = 30\,\mathrm{cm}^{-1} = 0.268J$. A perfect agreement with the experimental data for both the triplet *and* the singlet excitation gap could not be expected, due to the relatively simple Hamiltonian (5.1) on which the calculations are based. For instance the magnetic interchain coupling or the dynamics of the phonons are likely to renormalize the magnetic energies. Nevertheless, the result for Δ_{00} yields no inconsistency and thus verifies the parameter choice for J, α, and δ in the framework of the approach chosen.

From the numerical result for the ground state energy per site $e_0(L)$ one can deduce a correlation length of $\xi \sim 7.4$ lattice spacings by fitting the appropriate scaling function (cf. appendix B and [53]). Moreover, similar to the excited triplet, the excited singlet state can be regarded as a state which resembles the ground state but contains two bound $S = 1/2$ spinons which are coupled to a singlet (cf. section 5.1.4) [61,62]. One can estimate an upper bound for spatial extension of the two-spinon object from the system size where the saturation sets in to be about 40 sites (cf. Fig. 5.2).

In general, the computation of excitation spectra can also be performed via Fourier transformation of dynamical correlation functions. This can be used to formulate an alternative approach for the calculation of low lying excitations (singlet or triplet). Combining the DMRG approach with the continuous fraction expansion of Green functions allows for instance the computation of dispersion curves for finite systems [16]. A refined version of this approach has recently been developed by Kühner and White [17]. An example and details concerning this technique are given in appendix A. In the given context, however, it is much more efficient to compute the excited states by fixing $S^z_{total} = 1$ (triplet) or by applying S^+_{total} to the possible target states (singlet) as explained in section 2.8.

5.1.4 Low Energy Spectrum

In this section some general features of the low energy spectrum of the model (5.1) are considered, independent of the application to $CuGeO_3$.

Firstly let us focus on the singlet–triplet energy gap $\Delta_{01}(\delta)$ for various frustration values. The scaling behavior of the ground state is discussed in appendix B. In an unfrustrated system the energy gap scales like $\delta^{2/3}$ as was shown by Cross and Fisher [42, 43]. In general, however, multiplicative logarithmic corrections make it difficult to observe the asymptotic behavior. Since these logarithmic corrections are absent for $\alpha = \alpha_c$ [44] the energy gap values for $\alpha = 0.241$ are included in Fig. 5.1 (circles). A two parameter fit $\Delta_{01} = a\delta^\nu$ yields a value of 0.65 for the exponent ν.

Surprisingly, power law fits with exponents close to 2/3 describe the gap growth fairly well not only in the subcritical frustration regime, but also for supercritical frustration if a constant energy gap $\Delta_{01}(\alpha)$, due to spontaneous dimerization, is taken into account.

The results shown in Fig. 5.1 are consistent with those in Refs. [44, 63]. In Ref. [63], however, small deviations from the low lying gap values shown in Fig. 5.1 are present[3] leading to somewhat smaller exponents.

In the supercritical frustration regime the exponent 2/3 can nicely be explained applying the spinon picture. Spinons are the elementary excitations of antiferromagnetic (weakly dimerized) Heisenberg chains.

---

[3] In general for tiny gaps the extrapolation used in Ref. [63] yields presumably too small values. For instance $\Delta_{01}(\alpha = 0.4) \approx 0.05$ is derived in Refs. [44, 64] which is about twice as large as the value found in Ref. [63].

A spinon is a spin S=1/2 object which is associated with a domain wall in the dimerization as schematically depicted below

.

Inserting two spinons in an externally dimerized chain one finds that the singlets between the spinons are out of phase with respect to the external dimerization,

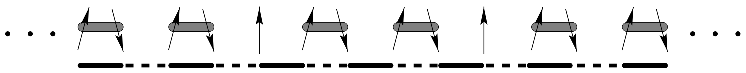

,

where the strong (weak) bonds $J+\delta J$ $(J-\delta J)$ are depicted with bold (dashed) lines underneath. The energy cost is proportional to the spinon distance. Hence, the spinons are mutually bound by a linear potential. Within the framework of a continuum approach the Hamiltonian for the spinons contains this linear potential and a quadratic kinetic energy,

$$E\psi(x) = -\frac{J}{2m}\frac{\partial^2}{\partial x^2}\psi(x) + \frac{3\delta J}{4}x\psi(x) \ , \tag{5.2}$$

with the restriction $x \geq 0$ (soliton distance). Rescaling of Eq.(5.2) by

$$x = \xi y \quad \text{with} \quad \xi = (3m\delta/2)^{-1/3} \tag{5.3}$$

yields

$$E\tilde{\psi}(y) = J\left(\frac{3}{4}\frac{\delta}{\sqrt{2m}}\right)^{2/3}\left(-\frac{\partial^2}{\partial y^2}\tilde{\psi}(y) + y\tilde{\psi}(y)\right) \ . \tag{5.4}$$

The solutions for the spinon wave function in Eq. (5.4) are given by the shifted Airy functions [65]. Moreover, Eq. (5.4) shows that a linear potential together with a quadratic kinetic energy leads to energies proportional to $\delta^{2/3}$ if δ measures the potential strength [61,62]. Therefore, Eq. (5.4) provides a simple explanation for the numerically observed relation $\Delta_{01} \sim \delta^{2/3}$.

The main difference in the subcritical regime $\alpha < \alpha_c$ is the absence of the energy gap for $\delta = 0$, leading to a linear kinetic energy for the spinons. Revisiting the scaling argument used above one finds that now a square root potential would retain the exponent 2/3. Indeed this is corroborated by the DMRG calculations of the confining potential (for details see appendix C and [61, 62]).

In conclusion, the exponent of the gap growth can be understood applying a simple quantum mechanical picture in the case of sub- *and* supercritical frustration.

5.1.5 Higher Excitations

Not only from the theoretical point of view but also with respect to the measured excitation spectrum of the insulating magnetic substance $(VO)_2P_2O_7$ it is challenging to investigate the occurrence of a second triplet excitation. $(VO)_2P_2O_7$ represents a low-dimensional spin system composed of $S=1/2$ V^{4+} ions which have Heisenberg interactions. First, the system was believed to be a realization of a two-leg antiferromagnetic spin-ladder [66, 67]. This picture was revised by Garret *et al.* [68, 69] in favor of a static dimerized model. Furthermore Garret *et al.* [68] observed two low lying excitations in neutron-scattering experiments. The occurrence of bound states, in particular the occurrence of a second bound triplet state has intensively been analyzed in several theoretical studies [70–73]. Unfortunately this excitation is hardly accessible by DMRG. Since the momentum q cannot be fixed, it is not possible to distinguish the states belonging to the first triplet branch at higher q from the second triplet state with $q = 0$. Thus the selection of the appropriate target state is impossible.

Another possibility to access the second triplet is to apply the continuous fraction technique. The excitation can be calculated as described in appendix A. But instead of the lowest singlet state the Raman operator is applied to the lowest state with $S^z = 1$. This approach, however, requires an enormous numerical effort even for small systems, so that no reliable data for $L \to \infty$ were obtained.

5.2 Doped $CuGeO_3$

$CuGeO_3$ exhibits a surprisingly rich phase diagram upon doping [28,29, 74–80]. For instance the substitution of Cu by Zn/Mg or of Ge by Si leads to a rapid suppression of the spin gap and the SP order parameter, while antiferromagnetic (AF) order is enhanced. Both kinds of doping can be viewed as mechanisms that lead to effective interruptions of the spin chains. The experimentally observed fact that Si doping has a more drastic effect on the reduction of the SP temperature than Zn doping can be explained by structural arguments. The Cu-O-Cu exchange path depends crucially on the hybridization between Ge *d*-orbitals and the bridging oxygen *p*-orbitals [31]. Replacing Ge by the somewhat smaller Si atom leads to a suppression of the superexchange constants in both adjacent chains simultaneously (cf. Fig. 4.1 on page 34), whereas substituting Cu by Zn, which has spin $S = 0$, causes the suppression of the superexchange only in a single chain. Experimentally, however, Si doping is by a factor 3 more effective than Zn doping [78], which is an even stronger enhancement than the structural argument predicts.

In the following Zn or Mg ($S = 0$) impurities are modeled, focusing on two surprising features which occur upon doping. The first is the unexpected coexistence of the SP phase and antiferromagnetism. The second is the observation of an additional peak in the Raman spectra of the doped compounds $Cu_{1-x}Zn_xGeO_3$ [58]. There are several theoretical studies considering the AF order [81–86]. Both features can qualitatively be understood also on the basis of the following DMRG results.

5.2.1 Doping Induced Antiferromagnetism

In a uniform dimerized state AF order is excluded because all the spins are bound in singlets. Increasing the fraction of Zn dopants stabilizes antiferromagnetism while suppressing SP ordering. For low doping one observes even the coexistence of AF long-range order and the SP phase [76–78]. The occurrence of antiferromagnetism upon doping is surprising, because normally disorder, as induced by the dopants, leads to a strong suppression of AF order. Modeling the dopants as described below the enhancement of AF order and the coexistence with the SP phase is immediately reproduced in the framework of the approach chosen.

5.2.1.1 Modeling Doped $\mathrm{CuGeO_3}$

Basically a $S=0$ impurity can be modeled by removing a single spin. The mutual interaction αJ between both adjacent spins of the impurity (vacancy) is neglected in the following[4]. Hence, inserting $S=0$ impurities is equivalent to dissect the spin chain into finite segments. Removing a single spin of a dimerized chain leaves a free spin next to the missing one. Here, the focus is put on the free spin which resides at the open end of the finite chain segment and particularly on its localization. An unpaired spin induces inevitably a domain wall in the dimerization

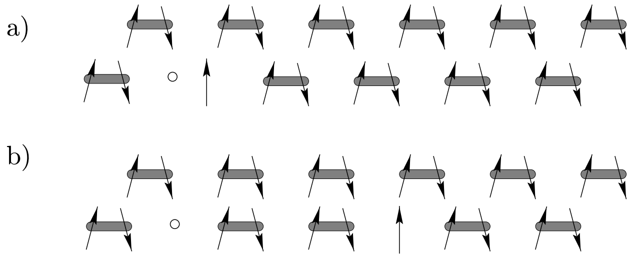

Figure 5.3: a) Two adjacent chains in the dimerized state. The grey eyelets denote the singlet binding of two spins. Removing one spin in the lower chain leaves one singlet partner freed.
b) Same chain configuration as in a) after two hops of the free spin. The first two singlets are now misaligned with respect to the upper chain.

as shown in Fig. 5.3.b. A similar scenario is sketched on page 47 in the context of the discussion of spinons as the constituents of the excited triplet state. The order parameter changes sign (cf. Fig. 5.3.b) and the dimerization is suppressed at the position of the free spin.

The free spin is not bound to the vacancy, as long as only a single

---

[4] This is justified for the relatively weak frustration $\alpha=0.35$ as is shown in Fig. 17 in Ref. [87]

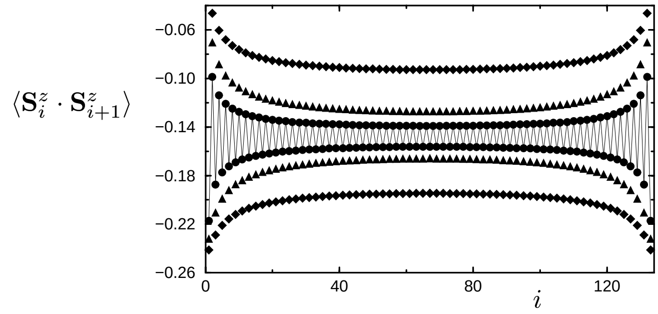

Figure 5.4: Correlation function $\langle \mathbf{S}_i^z \cdot \mathbf{S}_{i+1}^z \rangle$ for an unfrustrated Heisenberg chain (inner curve, circles and line), for frustration $\alpha = 0.241$ (triangles) and for $\alpha = 0.35$ (diamonds).

chain is under consideration. In a more realistic scenario, however, elastic interchain coupling, which causes the staggered dimer ordering along the b-direction (cf. Fig. 5.3.a), has to be taken into account [38,88]. Similar as in the case of two spinons (page 47) this leads to a linear confining potential, because the dimers between the vacancy and the spinon are misaligned with respect to the neighboring chains. As a consequence the spinon is no longer free but it is bound to the impurity.

Note that in the study of the low lying excitations presented in section 5.1.4 the spinon potential was caused by the explicit dimerization $(-1)^i \delta_0$. Yet the unchanged dimerization in the vicinity of the free spin is a somewhat unrealistic scenario as the lattice distortions are assumed to react to the spin system. Therefore, now the dimerization is not fixed from the beginning, but determined self-consistently as described in the following section. The neighboring chain which is assumed to be free of impurities in the relevant range has a fixed dimerization. Elastic interchain coupling causes a shifted pattern in the impurity chain as depicted in Fig 5.3.a.

A Heisenberg chain has particularly strong correlations $\langle \mathbf{S}_i^z \cdot \mathbf{S}_{i+1}^z \rangle$ at open chain ends (e.g. [4,89]). As shown in Fig. 5.4 this remains true also for frustrated chains. The strong, slowly decaying alternation already for $\alpha \leq \alpha_c$ is, so to speak, a precursor of the D phase, indicating the tendency towards dimerization. The energy cost of inserting a single spin, which comes along with breaking a strong bond, is minimal for the bonds in the middle of the chain (cf. Fig. 5.4). Therefore, the free spin can lower the energy by moving away from the chain end towards the middle of the chain. On the other hand the singlets between the free spin and one chain end are misaligned with respect to the neighboring chain (see Fig. 5.3). This implies an energy loss which again leads to an attractive linear potential and causes the binding of the spin to one chain end.

The following calculations are done on the basis of the one-dimensional Hamiltonian (4.4), taking an additional elastic interchain coupling into account. This leads to the modified elastic energy

$$E_{\mathrm{elast}} = \sum_i \left\{ \frac{K_\|}{2} \delta_i^2 + K_\perp \delta_i \hat{\delta}_i \right\} . \tag{5.5}$$

The interchain coupling $K_\perp$ is an effective coupling constant for the elastic interaction with all four neighboring chains, which are assumed to have the same fixed modulation $\hat{\delta}_i = (-1)^i \delta_0$. The modulation amplitude δ_0 belongs to the elastic coupling constant $K_\|$ in a purely one-dimensional system ($K_\perp = 0$). The interchain coupling is assumed to be positive to account for the experimentally observed checkerboard dimer structure in the undoped case [38, 88].

For numerical reasons open chains with even number of sites are investigated. Thus two free spins, which reside more or less at the chain ends, have to be considered. Focusing on the physics of a single spinon, chains of up to 140 sites are calculated to ensure that both spinons do not mutually interact[5].

Next we discuss the results; details about how the Hamiltonian (4.4), (5.5) can self-consistently be treated, i.e. how the δ_i are determined, are deferred to section 5.2.1.2. Fig. 5.5.a shows modulation patterns for $K_\perp \delta_0 = 0.01, 0.2$ and 1.0 (in units of J) with circles, squares and

---

[5] The relative energy difference of the spinon-singlet ground state and the triplet state where both spinons are parallelly aligned is found to be less than $10^{-5} J$, indicating an extremely weak mutual interaction.

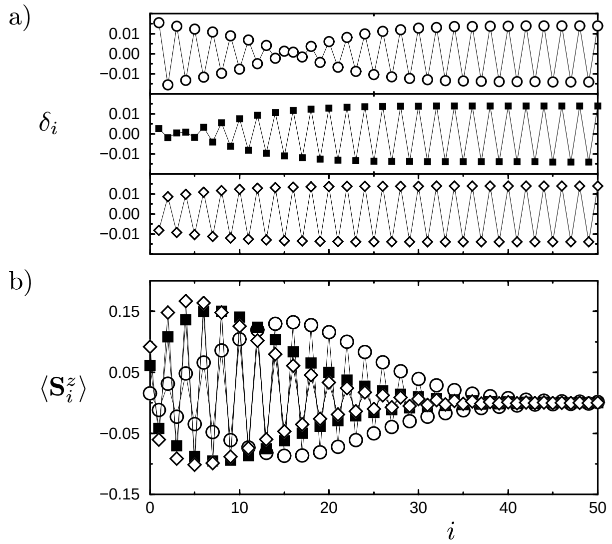

Figure 5.5: a) Local dimerization δ_i at the end of an open chain for $\alpha = 0.35$. The elastic interchain coupling $K_\perp \delta^0$ equals $0.01, 0.2,$ and $1.0\,J$, $K_\parallel = 18.8, 32.4, 89.5\,J$ (from top to bottom).
b) The corresponding local magnetizations for the modulation pattern shown in a).

diamonds, respectively. For each calculation $K_\parallel$ is fixed so that the absolute dimerization is about 1.3% in the bulk[6].

Obviously the dimerization is suppressed in the vicinity of the free spin as becomes most evident in the upper panel of Fig. 5.5.a. This was to be expected since the spin has no partner to form a singlet. Due to the delocalization of the free spin the dimerization is reduced in a region of about twice the correlation length. Fig. 5.5.b displays the corresponding local magnetizations from which the delocalization range can be read off directly. The local magnetizations can be interpreted as the spinon probability $|\psi^2|$ (cf. Eq. (5.2) for the continuous case). As expected, the local magnetizations sum up to $S^z = 1/2$ in each case. Large interchain coupling $K_\perp$ leads obviously to almost localized

---

[6] $K_\parallel + 2K_\perp = K_0 = \text{const} \approx 18J$; cf. E_{elast} in (4.4) and (5.5)

spinons at the chain ends.

Henceforth, the spinon, i.e. the delocalized unpaired free spin (Fig. 5.5.b), and the associated zero in the distortion pattern (Fig. 5.5.a) is denoted as *soliton*.

Although the spinon carries the integrated magnetization of $S^z = 1/2$ one finds a considerable number of sites showing a negative magnetization $S_i^z < 0$. The AF correlations extend from the first to almost the 40th site in the case of $K_\perp \delta^0 = 0.01$ (open circles). The large AF ordered domains associated with the impurities explain the tendency to AF long-range order in the doped compounds, since magnetic interchain coupling and an effective interaction within the chains may cause a three dimensional arrangement of the AF regions in the different chains.

If the number of dopants is not too large, i.e. the mean distance of the impurities is larger than a critical value, one finds constantly dimerized regions between the impurities. This provides a natural explanation for the observed coexistence of AF order and dimerization.

5.2.1.2 Self-Consistent DMRG Approach

As shown in Fig. 5.5.a the spinon causes a modulation of the δ_i. Hence, in these calculations the δ_i must not be fixed from the beginning, but have to be calculated self-consistently. The optimum dimerization, which will be called *adaptive modulation* henceforth[7], is found by minimizing $\langle \hat{H}_{\text{chain}} \rangle + E_{\text{elast}}$ (Eqs. (4.4),(5.5)) with respect to all $\{\delta_i\}$ which yields the condition

$$J\langle \mathbf{S}_i \cdot \mathbf{S}_{i+1} \rangle + K_\parallel \delta_i + K_\perp \hat{\delta}_i - \frac{J}{L} \sum_i \langle \mathbf{S}_i \cdot \mathbf{S}_{i+1} \rangle = 0 \; . \qquad (5.6)$$

The last term is included to ensure that the δ_i satisfy the constraint $\sum_{i=1}^{L} \delta_i = 0$. By means of Eq. (5.6) a new set of $\{\delta_i\}$ can be derived as a function of $\hat{\delta}_i$ and $\langle \mathbf{S}_i \cdot \mathbf{S}_{i+1} \rangle$. The expectation values are taken with respect to the lowest-energy state which is calculated via DMRG for a given set $\{\delta_i^0\}$. Starting with an e.g. alternating configuration for the δ_i^0 it turns out that as few as about 10 iterations are sufficient to

---

[7] This is because the lattice distortions are allowed to adapt to the spin system.

reach a stable modulation pattern which does not change perceptibly on further iterations. For the calculation of the lowest state we use the *finite size* algorithm (section 2.4) to account for the translationally non-invariant modulations.

5.2.2 Bound Spinon Excitations

Recently Els *et al.* [58] discovered an additional peak at energies of about the singlet–triplet gap ($17\mathrm{cm}^{-1} \approx 24K$) in the Raman spectra of the doped samples $\mathrm{Cu_{1-x}Zn_xGeO_3}$. An explanation for the occurrence of the additional excitation is given in Ref. [58]. As shown above the spinon resides near the impurity because of the linear potential which arises due to the elastic interchain coupling. The additional singlet excitation is interpreted as the transition from the lowest lying bound-spinon state to the next higher one.

In section 5.1.3 the lowest lying singlet excitation was calculated for periodic boundary conditions in the limit $L \to \infty$. In view of the experimental observation in the doped samples, now the lowest excitations of *open* chains with adaptive distortion patterns (cf. Fig. 5.5.a) are calculated. In this case two additional singlets with energies less than Δ_{01}^{bulk} are found[8]. The lowest excited singlet state has an energy of $0.59\Delta_{01}$ and the second lowest one of $0.85\Delta_{01}$ for $K_\perp\delta^0 = 0.2J$. The ratios $\Delta_{00}^{1,2}/\Delta_{01}^{bulk}$, where $\Delta_{00}^{1(2)}$ denote the lowest (second lowest) singlet excitation gap, depends only weakly on the interchain coupling $K_\perp$. For instance for $K_\perp\delta^0 = 0.001J$, $\Delta_{00}^{1}/\Delta_{01}^{bulk} = 0.52$ and for $K_\perp\delta^0 = 1J$ it increases to $\Delta_{00}^{1}/\Delta_{01}^{bulk} = 0.64$. So, in agreement with the experiment on doped $\mathrm{CuGeO_3}$, additional singlet excitations are found for open systems in the framework of the self-consistent approach. The calculated energies, however, are not in quantitative accordance with the experimental value, probably because of magnetic interchain coupling.

Lastly the lowest triplet excitation is analyzed applying open boundary conditions with adaptive distortions. For the triplets no significant energy change in comparison to the undoped (periodic) case is found.

---

[8] Recalling the notation used above: Δ_{01} denotes the singlet–triplet and Δ_{00} the singlet–singlet gap.

Fig. 5.6 shows the local magnetizations of the lowest state with $S^z = 2$ in comparison to the 'ground state' with $S^z = 1$[9]. Obviously the excitation is located in the bulk which explains why the triplet energy gap is hardly affected by the change of the boundary conditions.

A similar analysis of the excitations was performed in [86]. Among other items the local magnetizations of the lowest excitation for open chains were calculated (not self-consistently). In agreement to the above results it was shown that the low lying singlet excitations are located at the chain ends, whereas the lowest triplet excitation occurs in the bulk. Obviously the same holds true for the adaptive modulation pattern which yields the magnetizations shown in Fig. 5.6.

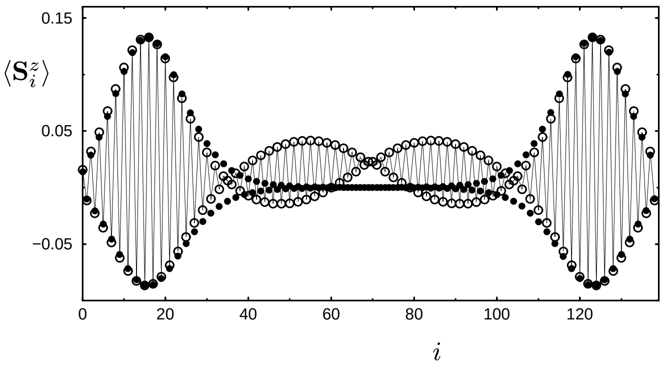

Figure 5.6: The local magnetization in the ($S^z = 1$)–'ground state' (filled circles) in comparison with the magnetization in the lowest state with $S^z = 2$, for $K_\perp \delta^0 = 0.01J$ and $\alpha = 0.35$ (see Fig. 5.5).

---

[9] As stated in the footnote on page 52 the relative energy difference between the lowest state where the two spinons at the chain ends are coupled to a singlet and the state where they are parallelly aligned (spinon triplet) is less than $10^{-5}J$. Hence, the triplet state is also denoted as 'ground state'.

Chapter 6

Spin-Peierls Systems under Magnetic Field

A large fraction of the experimental as well as the theoretical work on SP systems is dedicated to investigations of properties in external magnetic fields.

SP compounds exhibit characteristic properties above a certain critical field. The value of the wave vector q of the lattice distortion in the absence of an external field is π, reflecting the alternating spin exchange coupling[1]. When a magnetic field is applied q sticks to π for low magnetic fields. Above a critical field, however, it starts to deviate signaling the transition to the incommensurate (I) phase. In this high field phase the modulation of the exchange coupling is incommensurate with respect to the underlying lattice structure. The phase diagram of $CuGeO_3$ which is representative for SP compounds in general is shown in Fig 4.2.

The incommensurably modulated phase has attracted much interest among theoreticians. Although many of the observed features of the I phase can be understood on the basis of the pioneering theoretical studies of Nakano-Fukuyama [92, 93], Fujita-Machida [94], and others [95–97] several observations indicate that a refinement of these analytical approaches is necessary. A detailed analytical description of the I phase is still a challenging task.

Strictly speaking, infinite systems are necessary to account for the

---

[1] The lattice constant a is set to unity.

incommensurate, i.e. the non periodic, spin–lattice structure. Using the DMRG approach one is of course restricted to finite systems. But the lattices and therefore also the periodicity of the modulations considered can be chosen very large. So the tractable modulations are very close to incommensurable structures.

In the next section the transition from zero to finite magnetization is analyzed, with particular emphasis on the order of the phase transition. Firstly, this is done for SP systems in general. Three different ways of modeling the magnetic phase are considered. Secondly, the results are applied to $CuGeO_3$ under magnetic field.

6.1 D–I Phase Transition

From the theoretical point of view, contradictory predictions have been derived concerning the order of the phase transition from zero to finite magnetization. The phase transition was predicted to be of first order by Cross [98]. Bhattacharjee *et al.* obtained the same conclusion using a phenomenological Ginzburg-Landau expansion [99]. But mean-field calculations of Fujita-Machida for a renormalized XY-model display a second order phase transition [94] while Buzdin *et al.* [97] find a second order phase transition only at $T = 0$ and a first order one for $T > 0$ using essentially the same model as Fujita-Machida.

In this section magnetizations for three different types of models are calculated showing that the order of D–I phase transition is strongly model dependent. For all the calculations parameter sets are chosen which are convenient for the numerical treatment, i.e. displaying small finite size effects.

6.1.1 Fixed Alternating Modulation

As a starting point let us consider the simple case where the lattice distortion is kept frozen as in the D phase in spite of the presence of a magnetic field,

$$\delta_i = (-1)^i \delta \ . \tag{6.1}$$

The amplitude δ is treated as a fixed parameter. This approach is appropriate for modeling structurally dimerized systems or ladder systems. Chitra and Giamarchi [100] calculated the magnetization of frustrated *or* dimerized spin chains in a magnetic field using bosonization techniques. Within this continuum-limit approach the frustration and dimerization cannot be treated simultaneously since this would amount to the treatment of a double sine-Gordon model. In both cases, for dimerization *or* frustration, the magnetization is found to increase as $m \propto \sqrt{H - H_c}$ just above the critical field [100]. With the DMRG method, the square root behavior is found to remain true in presence of both dimerization *and* frustration, see Fig. 6.1.

As recently shown by Tonegawa *et al.* by means of exact diagonalization [101] an additional remarkable feature appears in some parameter range of dimerization and frustration, namely a plateau at $m = 1/4$ as shown in Fig. 6.1[2].

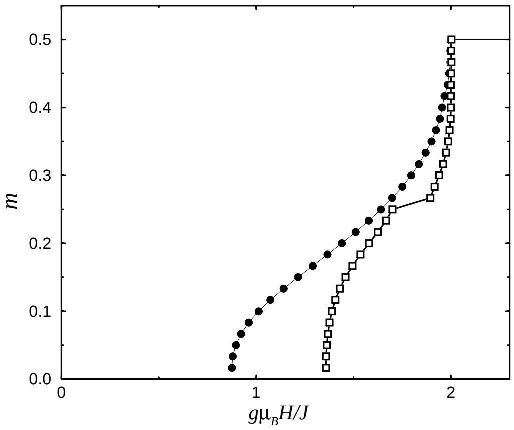

Figure 6.1: Magnetization as a function of the magnetic field for $\delta = 0.3$, $\alpha = 0.1$ (filled circles) and $\delta = 0.5$, $\alpha = 0.2$ (open squares) for a 60-site chain.

---

[2] Due to the discreteness of the magnetization values $m = n/L$, with $n = 0 \dots L/2$ (here $L = 60$), the plateau cannot be resolved completely. The plateau including the edge singularities is only seen in the limit $L \to \infty$.

The occurrence of plateaus is expected to be linked to the Lieb–Schultz–Mattis (LSM) theorem [102]. The extended version of the theorem states that if $n(S-m)$ *is not integer* a low lying state exists with energy $O(1/L)$ above e_0 under the assumption of a non-degenerate ground state [103]. Here S is the magnitude of the spins, m is the magnetization, L is the system size and n denotes the periodicity of the ground state with energy per site e_0. The periodicity is determined by the explicit spatial structure of the Hamiltonian and by a possible spontaneous symmetry breaking. The plateau appears at $m = 1/4$ (Fig. 6.1). Indeed, a four site periodicity seems reasonable in this case since half of the spins are bound in dimers and the other half is aligned parallel to the z axis. Actually, the periodicity of four of the $m = 1/4$ state was numerically verified in Ref. [101]. For $m = 1/4$ and $n = 4$ the condition $n(S-m)$ *not integer* is not fulfilled and the system may be gapped according to the LSM theorem. However, the low energy state predicted in the LSM theorem has the same magnetization as the ground state. Thus, strictly speaking, the theorem does not apply to the calculated plateau in the magnetization curve [104]. But one can expect that in general a gapless phase has low-energy states in both fixed and different magnetization sectors [103].

The second order phase transition as shown in Fig. 6.1 is in agreement with the fact that measurements under applied field for instance on $Cu_2(C_5H_{12}N_2)_2Cl_4$ show no hysteresis effects [105]. This substance is found to resemble an antiferromagnetic, strongly dimerized and frustrated Heisenberg chain [106,107] and a continuous increase of the magnetization for $H \geqslant H_c$ is observed. However, a linear dependence of the magnetization on the magnetic field was found instead of the expected square root behavior near H_c [105].

6.1.2 Sinusoidal Modulation

For spontaneously dimerized systems the dimerization pattern changes in the case of finite magnetization. For instance, X-ray measurements on $CuGeO_3$ clearly show that the structure of the lattice distortion becomes incommensurate for $H > H_c$ [108–110]. As a result of the lattice distortion the magnetic system should display a similar incommensurate modulation. Thus in this case an appropriate choice for the modulation is

$$\delta_i = \delta \cos(q r_i) \ , \tag{6.2}$$

as it was suggested in [60, 111]. To begin with, q is considered as a free parameter which is fixed by minimizing the total (free) energy. Note that for $q \neq \pi$ the elastic energy is q independent for the ansatz (6.2) yielding only a constant contribution at given amplitude δ. Hence it will be dropped for the following consideration.

Using the Jordan-Wigner transformation the applied magnetic field corresponds to a shift of the chemical potential. For the $XY-$model with a finite magnetization $m = S^z/L$, one can show that an infinitesimal spin-lattice coupling leads to an instability at momentum $q = 2k_{\mathrm{F}} = \pi(1 + 2m)$. In the case of the Heisenberg model, this relation is expected to hold true as well [98, 100, 111–113]. Within the present approach this is numerically confirmed by showing the energy to be

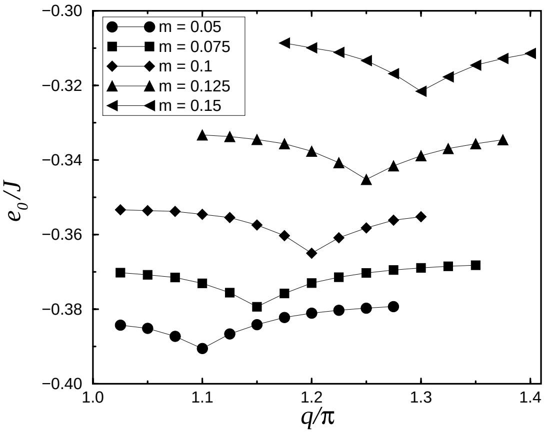

Figure 6.2: Ground state energy per site of an 80-site chain as a function of the modulation vector q (Eq. (6.2)) for various magnetizations m and $\alpha = 0.35$, $\delta = 0.1$.

minimal at

$$q = \pi(1 + 2m) \tag{6.3}$$

for a given magnetization m, for various sets of parameters δ, α and various system sizes. The ground state energy per site for $H = 0$ as a function of q is plotted in Fig. 6.2, for a set of magnetizations m and for fixed $\delta = 0.1$ and $\alpha = 0.35$. The positions of the cusps correspond exactly to $q = \pi(1 + 2m)$. Fig. 6.2 displays the generic behavior, independent of the parameters α and δ, and definitely confirms the relation between the wave vector and the magnetization.

Henceforth, the parameter q is fixed according to Eq. (6.3), and the magnetization is investigated as a function of the applied field. It turns out that the fixed sinusoidal exchange coupling (6.2) has a rather strong effect on the magnetization leading to a *first order* phase transition.

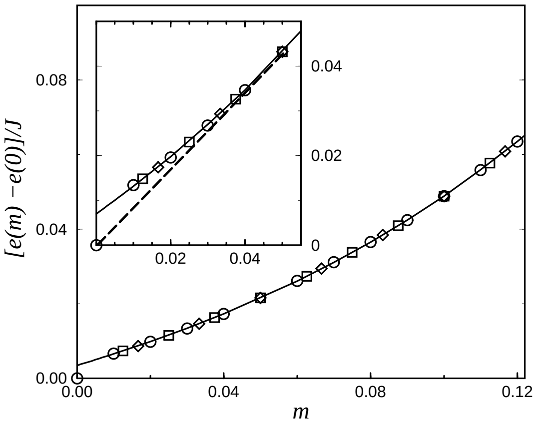

Figure 6.3: Ground state energies per site, $e(m) - e(0)$, as a function of the magnetization for the sinusoidal modulation (6.2) ($\delta = 0.2$, $\alpha = 0.35$) for chains of 100 (circles), 80 (squares), and 60 (diamonds) sites. To highlight the discontinuity at $m = 0$ a cubic fit for $m > 0$ is depicted as a solid line. The inset shows an enlargement and the tangent for $m = 0.05$ as described in the text.

To elucidate this, the magnetic ground state energy per site $e(m) = (\langle \hat{H}_{\text{chain}} \rangle + E_{\text{elast}})/L$ as a function of the magnetization is presented in Fig. 6.3. Results for several chain lengths are included to show that finite-size effect do not harm the drawn conclusion.

The salient feature of $e(m)$ for sinusoidal modulation is the discontinuous jump at $m = 0$. To understand this jump it is helpful to look at the averaged squared distortion $\frac{1}{L}\sum_i \delta_i^2$ which takes the value δ^2 at $q = \pi$ and $\delta^2/2$ otherwise. In the D phase all δ_i are maximally distorted whereas already for an arbitrarily small incommensurability there are large regions with weaker distortions. Hence, the elastic energy is discontinuous in the limit $q \to \pi$. This affects the magnetic energy which reacts to the modulated distortions.

The dependence $m(H)$ can be deduced from $e(m)$ in Fig. 6.3 by minimizing the total energy $\tilde{e} = e(m) - g\mu_{\text{B}}H$. In other words one has to compute the convex hull. This defines the magnetic field $H(m)$ and by inversion one obtains $m(H)$. The jump in $e(m)$ leads to a first order transition with a jump in $m(H)$. The resulting magnetization $m(H)$ deduced from Fig. 6.3 is depicted in Fig. 6.4.

Calculating the corresponding local magnetizations for each site [111] one finds that there is a large alternating local magnetization close to each zero of the modulation like in the doped case (cf. Fig. 5.5). The local magnetizations around each zero add up to the contribution of one spinon with $S^z = 1/2$. Summing the z-component of all spinons yields the total magnetization $m{\cdot}L$.

6.1.3 Adaptive Modulation

In the previous section the modulation, more precisely the parameter q, was fixed by minimization of the total energy. It is more accurate, however, to determine the whole modulation $\{\delta_i\}$ by minimizing the total energy (4.4) in a certain S^z subsector with respect to all the parameters δ_i. For a given magnetization the lattice distortion is thus allowed to adapt to the spin system.

For the self-consistent treatment of the lattice we use the DMRG approach as outlined in the context of modeling doped systems in sec-

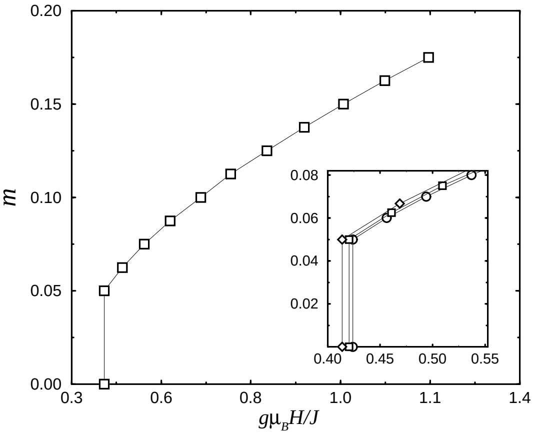

Figure 6.4: Magnetization as a function of the applied magnetic field for $\alpha = 0.35$ and $\delta = 0.2$ of a 80-site chain as deduced from the open squares in Fig.6.3. The inset shows an enlargement near H_c for 100- (circles), 80- (squares), and 60- (diamonds) site chains.

tion 5.2.1.2. In comparison to the application to doped systems there are two minor modifications. First, the elastic intrachain coupling is set to zero. This is justified since it is reasonable to assume that the incommensurate modulation is the same (modulo -1) in adjacent chains. Therefore the interchain coupling causes only a renormalization of the coupling constants. Second, a sinusoidal or a step-like modulation is chosen in the first iteration in the case of small and large dimerization respectively. The ensuing modulation is of course independent of the start modulation. The proper start configuration, however, reduces the number of iterations which are necessary to yield a stable pattern.

The envelope of the final modulation can be fitted by a product of complete Jacobi elliptic functions of modulus k as predicted analytically [93, 94, 97, 114]. Fig. 6.5 shows a generic modulation pattern for very low magnetization, i.e. low concentration of solitons. In this limit the vicinity of each zero resembles a hyperbolic tangent [93]. The relatively large dimerization $\max\{\delta_i\} \approx 0.2$, due to the small elastic coupling constant $K_0 = 1.7J$, leads to a rather small correlation length

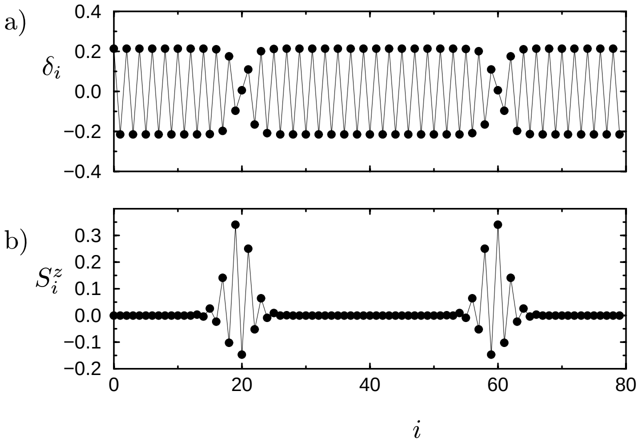

Figure 6.5: a) Incommensurate modulation δ_i of an 80-site chain for $\alpha = 0.35$ and $K_0 = 1.7J$.
b) The corresponding local magnetizations for the modulation pattern shown in a).

of only a few sites as can be seen in Fig. 6.5.

Once the modulation pattern is determined the corresponding energy is calculated in each S^z subsector. The energy $e(m)$ is found to be convex and continuous, in contrast to the curves with fixed sinusoidal modulation. Thus one finds a continuous, *second* order phase transition from the D phase to the adaptively modulated I phase. The corresponding magnetization $m(H)$ is depicted in Fig. 6.6 with filled circles.

The enormous steepness of the continuous magnetization is explained by the following argument: For non-interacting spinons which are far enough apart, the energy per site $e(m) - e(0)$ is proportional to the number of spinons and hence to the magnetization m. The proportionality constant e_0 is the creation energy of a single spinon and determines the critical field $2e_0 = g\mu_{\mathrm{B}}H_c$ since the spinons are created pairwise by the annihilation of singlets. Because the spinons are exponentially localized (cf. Fig. 6.5) two spinons at mutual distance l have additionally an exponential interaction $w(l) = w_0 \exp(-cl)$. Here c is a constant of

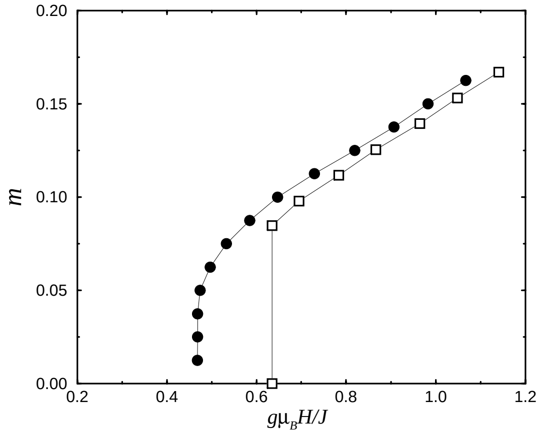

Figure 6.6: Filled circles: Magnetization for the adaptive modulation with $K_0 = 1.7$, $\alpha = 0.35$. Open squares: Magnetization with a dispersive elastic energy as discussed at the end of the paragraph. $\tilde{K} = 6K_0$, K_0 and α unchanged.

the order of the inverse correlation length and w_0 is a proportionality constant which is positive for repulsion and negative for attraction. The typical distance of the spinons is $l = 1/(2m)$ since each spinon carries spin $S = 1/2$. Hence, for not too large values of m, the total energy in an external magnetic field H equals

$$e(m) - e(0) = g\mu_{\mathrm{B}}(H_c - H)m + w_0 2me^{-\frac{c}{2m}} \,. \tag{6.4}$$

By minimizing this expression for repulsion ($w_0 > 0$) one derives $H(m)$ which increases exponentially slow just above H_c. This in turn leads to the drastic increase of m as depicted in Fig. 6.6.

To present more clearly the effects of soliton interaction which causes the convexity of $e(m)$ it is convenient to pass to an affine representation of the ground state energy by investigating

$$e_{\mathrm{eff}}(m) := e(m) - e(0) - g\mu_{\mathrm{B}}H_c m \tag{6.5}$$

which would vanish identically if no interaction between the solitons existed. Note that $e_{\mathrm{eff}}(m)$ is convex if and only if $e(m)$ is. In Fig. 6.7

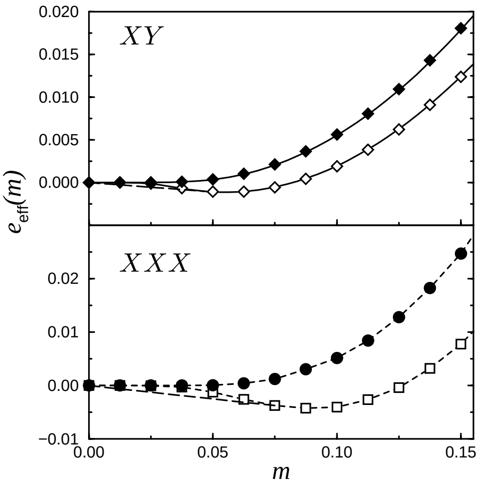

Figure 6.7: Affine representation of the ground state energy per site.
$XY-$model: The upper solid curve shows e_{eff} as defined in Eq. (6.5) for a dispersionless elastic energy with $K_0 = 0.625$. The lower solid curve shows e_{eff} for a dispersive elastic energy ($\tilde{K} = 6K_0$) as discussed in the text. Both curves are obtained via the continued fraction technique. The filled and open diamonds depict DMRG results for an 80-site chain.
$XXX-$model: DMRG results in the dispersionless case (filled circles) and for $\tilde{K} = 6K_0$ (open squares) for $K_0 = 1.7$ and $\alpha = 0.35$. The short dashed lines are guides to the eye only.
The long-dashed lines indicate the convex hulls to the lower curves.

the resulting generic curves are shown with filled symbols (solid line) for the $XY-$model and the spin isotropic $XXX-$model. The results for the unfrustrated $XY-$model in the thermodynamic limit were derived by Uhrig by means of a continued fraction technique based on Green functions [111]. This approach to the $XY-$model allows to iterate up to 80 times for an infinite chain with periodicities of up to 120-sites. These data are included as an additional check that no spurious effects due to finite size or insufficient iteration are investigated.

The results in Fig. 6.7 for a dispersionless elastic energy (filled symbols) comply perfectly with exponentially repulsive solitons as in Eq. (6.4) [115].

A dispersionless elastic energy is, of course, a simplification of the real phononic system. Cross already argued [98] that a pinning in k-space should influence the order of the transition. Presumingly the D→I phase transition becomes first order if the elastic energy itself favors the distortion at $k = \pi$. This means that $\hat{K}(\pi)$ is minimum if the elastic energy can be expressed as $E_{\mathrm{elast}} = \frac{1}{2}\sum_k \hat{K}(k)|\delta_k|^2$. The argument compares, for a given wave vector q close to π, the elastic energy $\hat{K}(q)$ of a sinusoidal modulation (6.2) with the one of an array of domain walls with the same periodicity $2\pi/q$. Since the latter has also contributions of higher harmonics $\pm 3q$, $\pm 5q$, $\pm 7q$, ... its elastic energy is $\sum_n |a_{(2n+1)q}|^2 \hat{K}(q)$ where the coefficients $|a_{(2n+1)q}|^2$ are symmetric with respect to π. Thus the elastic energy is higher than the one for the sinusoidal modulation. By this mechanism higher harmonics are suppressed due to the elastic energy leading to a smoother and more sinusoidal modulation. If the convex curve for the adaptive modulation is influenced in a way to approach the discontinuous curve for sinusoidal modulation one must expect that a region of concavity appears for small m (cf. Fig. 6.7). Hence the convex hull differs from the curve itself and a jump in the magnetization occurs: the transition is first order. Put differently, a dip in the elastic energy at the zone boundary may lead to an *attraction* of the solitons.

For the numerical investigation of the hypothesis, $\hat{K}(k) = K + 2\tilde{K}\cos(k)$ is used with $K_0 = K - 2\tilde{K}$ kept fixed to refer to the same amplitudes in the D phase. This elastic energy in real space can be written as

$$\begin{aligned} E_{\mathrm{elast}} &= \frac{1}{2}\sum_i \left(K\delta_i^2 + 2\tilde{K}\delta_i\delta_{i+1} \right) \\ &= \frac{1}{2}\boldsymbol{\delta}^{+}\,\mathbf{K}\,\boldsymbol{\delta}\ , \end{aligned} \tag{6.6}$$

where $\boldsymbol{\delta}$ is a vector with components δ_i and $\mathbf{K}$ is a cyclic tridiagonal $L \times L$ symmetric matrix of coupling constants with diagonal elements K and off-diagonal elements $\tilde{K}$. Generic results for the energies $\tilde{e}(m)$ in affine representation are depicted with open symbols (solid line) in Fig. 6.7. Indeed a concavity for small magnetizations m is found. This implies soliton attraction and a first order transition.

Furthermore, in Fig. 6.6 the resulting magnetization curve with dispersion of the elastic energy is shown. The difference between the second order transition for the elastic energy without dispersion and the first order transition with dispersion is clearly visible. Additionally, the critical field H_c at which the transition occurs rises on including the dispersion. This complies also with the consideration above since the energy of a single soliton rises due to $K + 2\tilde{K}\cos(k) > K_0$ except at $k = \pi$ for $\tilde{K} > 0$.

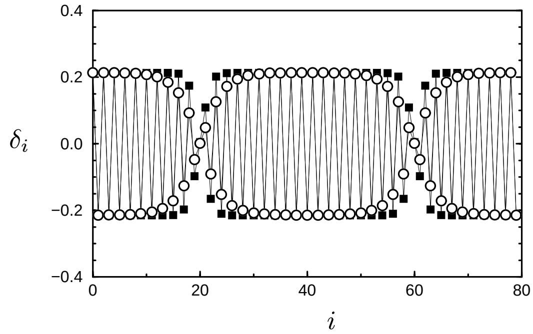

Figure 6.8: Modulations for $S^z = 1$ for the same parameters as in Fig. 6.7 for the $XXX-$model.

Finally, in Fig. 6.8 the modulation patterns with and without dispersion are compared (open circles and filled squares, respectively). Indeed, the inclusion of $\tilde{K} > 0$ makes the modulation softer and more sinusoidal. In conclusion the numerical results convincingly corroborate the expectations for the effect of a dispersive elastic energy.

Numerically, it is extremely tedious to decide whether an arbitrarily small $\tilde{K}$ yields already soliton attraction. For smaller values of $\tilde{K}$ the minima in the affine representation occur for smaller and smaller magnetization and they are more and more shallow. Probably the soliton attraction exists down to arbitrarily small values of $\tilde{K}$, but it may become irrelevant in practice due to the exponential smallness of the corresponding energies.

Negative values of $\tilde{K}$ have also been investigated. No qualitative change of the soliton interaction has been found in comparison to the dispersionless case. The iterative procedure, however, becomes quite unstable already for small negative values of $\tilde{K}$.

6.1.3.1 Adiabatic Gaps

So far the average magnetization as a function of the applied magnetic field was analyzed. Another interesting quantity which is accessible once $e(m)$ can be computed are the adiabatic gaps. It is so far an unsettled question whether spin-Peierls systems have or have not gaps in the incommensurate phase.

On the one hand, it seems clear that the incommensurate modulation pattern can be shifted along the chains without energy cost. This is certainly true in the continuum description and thus it is also true up to exponentially small pinning energies for not too small correlation lengths. This quasi-continuous symmetry gives rise to gapless quasi-Goldstone bosons called phasons [99,116]. They do not change the spin sector and thus have $\Delta S^z = 0$. The physics of phasons is beyond an adiabatic treatment of the lattice distortion. Here, within the static approach, the distortion is assumed to be fixed in a certain S^z subsector.

A different issue is the question whether the gaps $\Delta_\pm$ corresponding to $\Delta S^z = \pm 1$ are finite or not. Note that these gaps do not need to be equal since the spin rotation symmetry is broken for finite magnetization. From a non-adiabatic viewpoint one can infer from the smoothness of the $e(m)$ curves that there are no such gaps in the I phase since the modulation adapts always to the average magnetization. Applying, however, an operator like $S^+(k)$ or $S^-(k)$ [111,112] and asking for the accessible excitation spectrum may lead to a different answer. These operators act only on the spin part of the ground state and leave the modulation unchanged. Thus it is not unreasonable to expect that the gapless excitations are not accessible since their access required a rearrangement of the whole, truly three-dimensional, modulation. The underlying question is whether the states $S^\pm(k)|S^z\rangle$ are orthogonal to $|S^z \pm 1\rangle$ or not, where $|S^z\rangle$ denotes the ground state for the magnetization S^z.

Here the simpler question, whether in the strictly adiabatic framework the gaps $\Delta_\pm$ are finite or not, will be investigated. This is an extension of previous investigations [111] where only $\Delta_+ + \Delta_-$ could be computed, since this quantity does not require the knowledge of the corresponding magnetic field.

As before $e(m,H) := e(m) - mg\mu_\mathrm{B}H$ defines the ground state energy with self-consistently optimized modulation $\{\delta_i\}$.

$$\begin{aligned} e_\pm(m,H) \quad &:= \quad \frac{1}{L}\langle \hat{H}_\mathrm{chain}\rangle\Big|_{S^z=mL\pm 1} \\ & \qquad + \frac{K_0}{2L}\sum_i \delta_i^2 - \left(m \pm \frac{1}{L}\right) g\mu_\mathrm{B}H \end{aligned} \tag{6.7}$$

denotes the lowest-energy state with one additional spin flipped upward (+) or downward (−), respectively, *but* with the modulation $\{\delta_i\}$ belonging to $S^z = mL$, not to $S^z = mL\pm 1$. This means that for $e_\pm(m,H)$ the modulation is not optimized for the given magnetization. This corresponds to the situation accessible by application of $S^+(k)$ or $S^-(k)$ without reaction of the lattice part. Then the gaps are defined by

$$\Delta_\pm(m) = e_\pm(m,H) - e(m,H)\,. \tag{6.8}$$

The gaps Δ_+ and Δ_- for a 100-site ring are displayed in Fig. 6.9 for $\alpha = 0.35$ and $K_0 = 2.38$ corresponding to $\delta \approx 0.14$ in the D phase. Finite size effects are not yet completely negligible, but the qualitative behavior is the one shown. As far as the sum $(\Delta_+ + \Delta_-)$ is concerned it is in agreement with previous self-consistent renormalized Hartree-Fock results [111].

Most importantly, Fig. 6.9 shows that both gaps are indeed finite and of equal order of magnitude. It is interesting that apparently Δ_+ is smaller at small magnetization and Δ_- is smaller at larger magnetization. At least within the adiabatic approach, the I phase turns out to be gapped. Yet, it is an open question if this result has relevance in regard of the experiments on SP compounds.

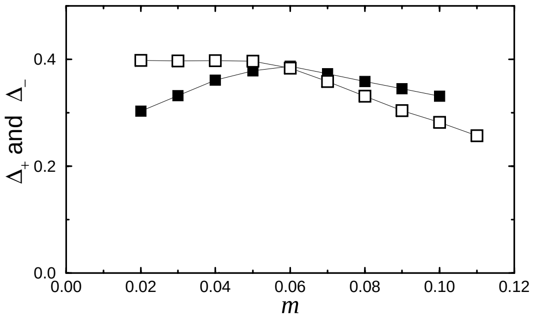

Figure 6.9: The energy gaps Δ_+ (filled squares) and Δ_-(open squares) as a function of the magnetization for $L = 100$, $\alpha = 0.35$ and $K_0 = 2.38$

6.2 CuGeO$_3$ in an Applied Magnetic Field

After the discussion of general properties of the high field phase let us now consider the application to CuGeO$_3$. A detailed discussion of CuGeO$_3$ under magnetic field focusing on experimental aspects can be found in Ref. [30]. Two experimental quantities can directly be compared to the DMRG results for the I phase. First, the elastic energy associated with the lattice distortion is correlated to the measured spontaneous strain. Second, the local magnetizations can be compared to NMR results.

6.2.1 Spontaneous Strain

The spontaneous strain is the relative length change of the system due to dimerization or incommensurable modulation:

$$\epsilon(H,T) = \frac{1}{L}\Big\{\Delta L(\delta(H),T) - \Delta L(0,T)\Big\} \quad , \qquad (6.9)$$

where H is the applied magnetic field, T the temperature and δ denotes the SP order parameter. $\Delta L(\delta,T)$ denotes the total length change, i.e. the difference $\Delta L(\delta,T) - \Delta L(0,0)$[3]. The spontaneous strain of

---

[3] $\Delta L(0,0)$ or in general $\Delta L(0, T < T_{SP})$ is derived by extrapolating $\Delta L(0, T > T_{SP})$ to low temperatures. The extrapolation is found to be independent of the

CuGeO$_3$ can be obtained via thermal expansion or magnetostriction measurements [117–120].

In the D phase δ is given by the absolute dimerization δ_0. In leading order one finds $\epsilon \propto \delta^2$, the linear term vanishes due to the obvious symmetry $\delta \to -\delta$. The proportionality has been verified experimentally by Lorenz *et al.* comparing $\epsilon(H,T)$ to the intensities of superstructure reflections [119]. Based on the proportionality $\epsilon \propto \delta^2$ the spontaneous strain, i.e. the relative length change of the system, can be compared to the DMRG calculations although the total system length is fixed within the numerical approach.

In the I phase the situation is more complex due to the spatial modulation of δ. The spontaneous strain cannot be sensitive to all the squared microscopic distortions δ_i^2 separately. However, it is reasonable to assume that the macroscopic quantity $\epsilon(H)$ is proportional to the averaged squared order parameter:

$$\epsilon(H) = c\,\langle\, \delta_i^2 \,\rangle_H \ , \tag{6.10}$$

where $\epsilon(H)$ denotes $\epsilon(H, T \to 0)$. The right hand side is proportional to the elastic energy in Eq. (4.4), which can be directly computed once the modulation pattern $\{\delta_i\}$ is determined.

As stated above, the simplest approach to model the I phase is the sinusoidal modulation (6.2), $\delta_i = \delta_0(H)\cos(qr_i)$ where the amplitude $\delta_0(H)$ allows for an additional field dependence. Therefore, the associated elastic energy in (4.4) equals $\frac{K_0}{2}\delta_0^2(H)\,\frac{1}{2}$ independent of the modulation vector q as long as $q \neq \pi$. Since the factor $\frac{1}{2}$ is absent for $q = \pi$ the sinusoidal modulation leads to a discontinuity at $H = H_c$. For $H > H_c$ one may assume that $\delta_0(H)$ scales with $T_{SP}(H)$ which explains the observed simultaneous saturation of $\epsilon(H)$ and $T_{SP}(H)$ for high fields (see below).

Fig. 6.10 shows two representative modulations which are obtained within the self-consistent approach for $S_z = 1$ and $S_z = 5$ corresponding to magnetic fields close to the D-I boundary ($\simeq$13 T) and a higher field ($\simeq$ 17 T), respectively. The calculation yields an obviously kink–like modulation for the small field in contradiction to the approach above.

---

applied magnetic field [117–119].

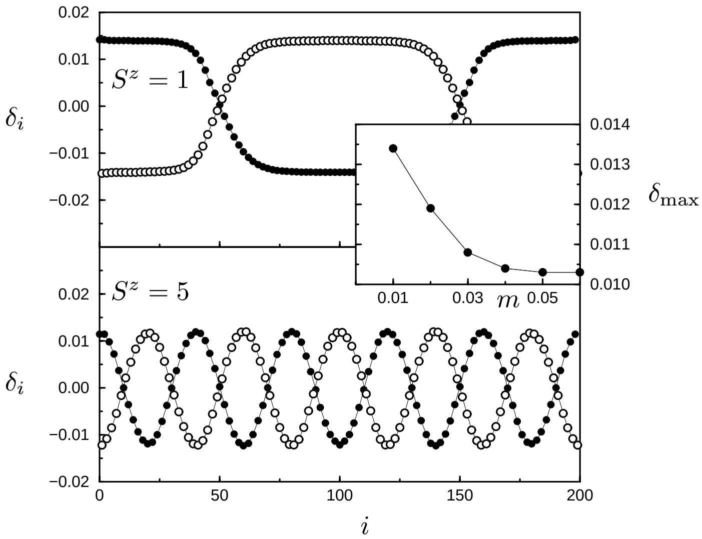

Figure 6.10: Local lattice modulation for a 200-site chain in the $S^z = 1$ (upper curve) and the $S^z = 5$ (lower curve) sub–sectors. The open (filled) symbols represent odd (even) sites. Inset: maximum dimerization amplitude as a function of the magnetization $m = S^z/L$ calculated for a 100-site chain.

Within the analytic approach for the soliton lattice the modulations δ_i are given by

$$\delta_i(H) = (-1)^i \delta_0 k \,\mathrm{sn}\big(\frac{i}{k\xi}, k\big) \ , \tag{6.11}$$

where $\mathrm{sn}(x, k)$ is a Jacobi elliptic function of modulus k, which is determined by the field dependent inter–soliton distance and by ξ the soliton width in units of the lattice constant [92,94,97]. The periodicity of $\mathrm{sn}(x, k)$ equals $4K(k)$, where $K(k)$ denotes the complete elliptic integral of second kind [65]. Thus the modulus k is fixed by the relation $m\,4K(k)\,k\xi = 1$ [116].

From X–ray scattering $\xi = 13.6$ is derived close to $H_{\mathrm{D/I}}$ [109] and the modulation period $q(H)$ can be extracted from the experimental magnetization.

The kink–like modulation for small fields can nicely be fitted by $\mathrm{sn}(x,k)$ yielding a correlation length of 10–11 sites in qualitative agreement with the experimental value. The fit is shown in the following section in the context of the analysis of the NMR results. The DMRG calculations, however, clearly show the failure of the kink–picture at higher fields. Already at moderate fields, i.e. for $S_z = 5$ (Fig. 6.10), the modulation looks almost like a simple sinusoidal distortion. Moreover, from the saturation of the maximum modulation $\delta_{\max}$ shown in the inset of Fig. 6.10 a solitonic picture with constant ξ can be excluded. The amplitude $\delta_{\max}$ is observed to become constant when the distance between the nodes of the order parameter becomes smaller than approximately $2\,\xi$.

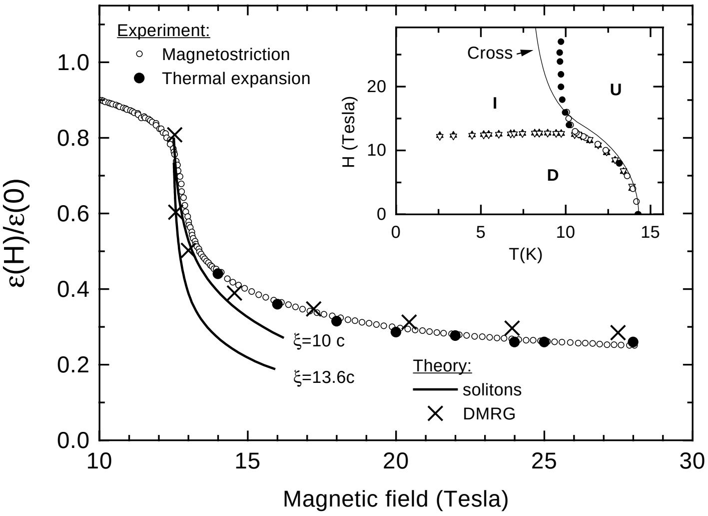

Figure 6.11: Spontaneous strain $\epsilon(H)/\epsilon(0)$ in the I phase as derived from thermal expansion (•) and magnetostriction (○) and $\langle\delta^2(H)\rangle$ calculated for a soliton lattice Eq.(6.11) (solid lines) and by DMRG (×) (see text). The Inset compares the experimental phase diagram to the calculation of Cross [98].

Now, according to Eq. (6.10) we compare the DMRG results for the elastic energy with the experimentally derived values of the spontaneous strain. The proportionality constant in Eq. (6.10) is eliminated by comparing $\epsilon(H)/\epsilon(0)$ to $E_{elast}(m(H))/E_{elast}(0)$. As depicted in Fig. 6.11 one finds an excellent agreement between the numerical data ($\times$) and experimental values ($\circ$,$\bullet$). For the numerical calculation the parameters $\alpha = 0.35$ and $K_0 \simeq 18J$ were used, leading to $|\delta_i| \approx 0.014$ in the D phase. As discussed in section 5.1 this parameter set (together with $J = 160\,\mathrm{K}$) is derived solely from properties in the U and the D phase. Hence, the agreement is obtained without an additional fit parameter. The inset compares the experimental phase diagram – in particular the saturation of $T_{SP}(H)$ (upper branch) as mentioned before – to the calculation of Cross [98].

The data shown in Fig. 6.11 indicate a crossover from the kink–like modulation for low fields to a sinusoidal one for higher fields. For H just above $H_c = 12.5\,\mathrm{T}$ one finds a rapid decrease of $\epsilon(H)$. This can be reproduced using the analytical formula for the soliton modulation (6.11). The corresponding ratio $\langle\delta_i^2(H)\rangle/\delta_i^2(0)$ using a correlation length $\xi = 10$ sites and the experimental value $\xi = 13.6$ sites are displayed with solid lines. The observed saturation at about 1/4 for fields higher than 20 T, however, contradicts the soliton approach (6.11) which implies a continued decrease, whereas the saturation, is in accordance with the sinusoidal modulation.

In summary, the field dependence of the averaged structural order parameter extracted from the data is in excellent agreement with the results of the DMRG calculations. A description of the spatial modulation in terms of a kink lattice is only possible quite close to the field driven commensurate–incommensurate phase transition at $H_{\mathrm{D/I}} = 12.5\,\mathrm{T}$. With increasing field both, the experimental as well as the numerical data, reveal a gradual change towards a sinusoidal modulation, which provides a good description of the distortion for fields above about 20 T.

6.2.2 NMR Results

Further information about the microscopic couplings in the I phase is supplied by NMR experiments. By means of the NMR line shape one gains insight into the distribution of the local spin polarizations. In this section the DMRG results for the local magnetizations are compared to the experimental NMR data. First, the results for a (slightly modified) sinusoidal modulation, are compared to the overall NMR line shape. Second, a more detailed analysis within the self–consistent approach is given.

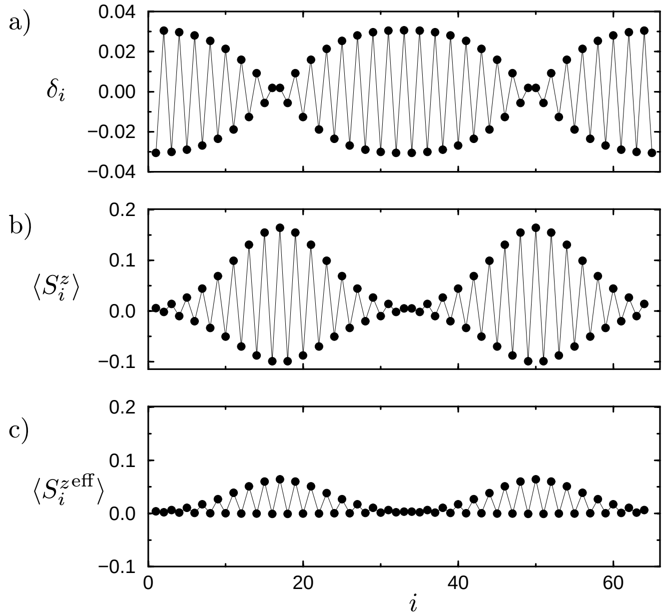

Figure 6.12: a) Sinusoidal modulation δ_i of a 66-site chain for $\alpha = 0.35$, $\delta_1 = 0.033$ and $\delta_3 = -0.07\,\delta_1$.
b) Local magnetizations for the modulation pattern shown in a).
c) Effective magnetizations deduced from the data in b) by averaging with $\gamma = 0.19$ (see text).

X-ray experiments [109] show also a third-harmonic super-lattice peak beside the first one. But the intensity of the latter is by far larger, $I_3/I_1 \sim 1/200$. Therefor{e, the incommensurate lattice distortion in the I phase is modeled with the sinusoidal modulation (6.2), adding a small third-harmonic contribution $\delta_3 \cos(3qr_i)$. The amplitude can be deduced from the X-ray intensities: $\delta_3/\delta_1 = -\sqrt{I_3/I_1} \sim -0.07$. Here, $\delta_1 = 0.033$ is chosen, which for $\alpha = 0.35$ reproduces the gap value resulting from averaging the dispersion perpendicular to the chains along k_b (cf. sect. 5.1.2) [35]. The modified sinusoidal modulation with the above parameters leads to the local magnetizations as shown in Fig. 6.12.b.

In NMR experiments the line shape of the copper nuclei is studied, which reflects the distribution of the local magnetizations. Thereby the spatial distribution of the $\langle S_i^z \rangle$ along the chain is accessible. In a continuous system the intensity is proportional to $(\partial \langle S_i^z \rangle / \partial i)^{-1}$. This is schematically indicated in Fig. 6.13, where for the sake of simplicity only a positive $\langle S_i^z \rangle$ modulation is considered. In particular the minimum and maximum magnetizations can directly be deduced from the NMR intensity.

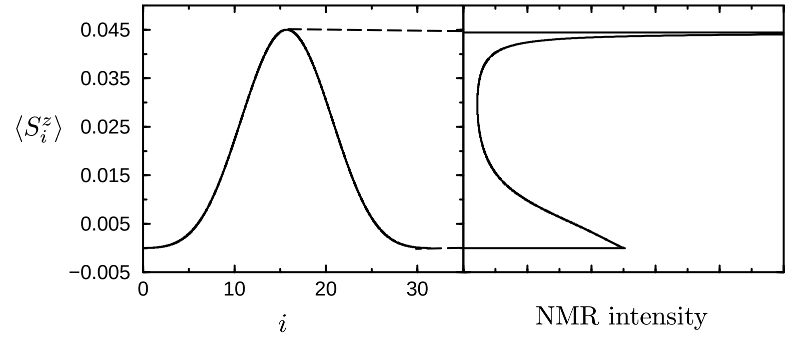

Figure 6.13: A sketch of a $\langle S_i^z \rangle$ distribution (left) and the resulting NMR line shape.

From the NMR experiment of Fagot-Revurat *et al.* [121] $|S^z_{\max} - S^z_{\min}|$ is read off to be about 0.065. This is obviously in contradiction with the theoretical $\langle S_i^z \rangle$ distribution shown in Fig. 6.12.b from which $|S^z_{\max} - S^z_{\min}|$ is read off to be about 0.26. In particular,

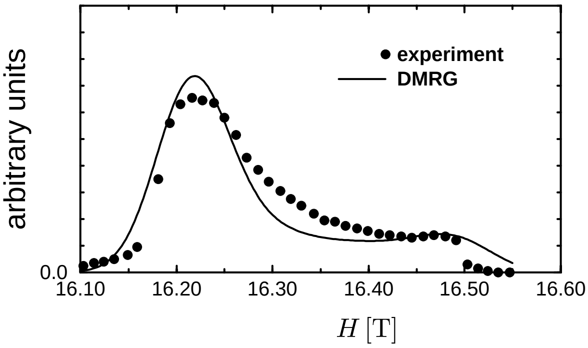

Figure 6.14: NMR line shape evaluated from the distribution of the local magnetizations displayed in Fig. 6.12.c. The internal NMR damping is $\sigma = 0.035$ T. The experimental data taken from Ref. [111] are depicted with •s.

the strongly negative part is in contradiction to the experimental findings. Yet, the misfit between theory and experiment can be resolved by considering zero-point fluctuations of phasons [111, 116]. Phasons as gapless excitations have already been discussed in section 6.1.3.1. They are linked to the possibility for the incommensurate distortion to slide along the chain without any energy cost. Strictly speaking, the energy cost is small but finite due to the discreteness of the underlying lattice which might induce a pinning of the incommensurate modulation. However, if the modulation length is large compared to the lattice spacing an upper bound for the pinning energy is estimated to be about $0.5\,\mathrm{K} \approx 0.003J$ [116][4]. The dynamics of the phasons induce oscillations of the modulation pattern. To incorporate these fluctuations in the present static, adiabatic approach a certain averaging over adjacent sites has to be performed leading to an effective polarization $\langle S_i^{z\,\mathrm{eff}}\rangle = (1-2\gamma)\langle S_i^z\rangle + \gamma(\langle S_{i+1}^z\rangle + \langle S_{i-1}^z\rangle)$. Here, γ is used as a fit parameter. Yet, a quantitative study of the zero-point fluctuations yields an estimate of γ which is in fair agreement with the fit value $\gamma = 0.19$ [116].

---

[4] In a continuous medium an incommensurate modulation breaks the continuous symmetry spontaneously, giving rise to Goldstone bosons, the so-called phasons. Here, for large modulation lengths the phasons are quasi Goldstone bosons which refer to the spontaneous breaking of the quasi continuous symmetry.

The averaged distribution $\langle S_i^{z\,\mathrm{eff}} \rangle$ is displayed in Fig. 6.12.c. The data are deduced from those shown in Fig. 6.12.b with the averaging factor $\gamma = 0.19$. Obviously, the amplitude is strongly reduced and a mainly positive distribution is obtained[5].

In Fig. 6.14 the solid line shows the theoretical NMR line shape deduced from the $\langle S_i^{z\,\mathrm{eff}} \rangle$ distribution shown in Fig. 6.12.c. To allow for a close comparison with the experimental NMR data (•s) an internal damping $\sigma = 0.035$ was used and the abscissa scale is converted into magnetic field following the procedure given in Ref. [121]. Obviously a reasonable agreement with the experimental data can be achieved.

A more detailed comparison of the magnetization distributions in the I phase is possible on the basis of the NMR data recently obtained in high quality experiments by Horvatic *et al.* [122]. There the data are analyzed within the scope of the continuum approach. In this approach the local magnetizations are given by the solution of the sine–Gordon equation [92, 123] which reads:

$$\langle S_i^z \rangle = \frac{W}{2} \left\{ \frac{1}{R} \mathrm{dn}\left(\frac{r_i}{k_m \xi_m}, k_m \right) + (-1)^i \mathrm{cn}\left(\frac{r_i}{k_m \xi_m}, k_m \right) \right\} , \qquad (6.12)$$

where cn and dn are Jacobi elliptic function of modulus k_m, i denotes the site index, ξ_m is the magnetic correlation length, and W, R determine the amplitudes of the alternating and non-alternating parts. In Ref. [122] all the constants are determined by means of the NMR results and the average magnetization.

For low soliton concentration, i.e. for H close to H_c, the distortion pattern can be described in terms of the Jacobi elliptic function sn as already introduced in Eq. (6.11)

$$\delta_i = (-1)^i \, \delta \; \mathrm{sn}\left(\frac{r_i}{k_d \xi_\mathrm{d}}, k_d \right) \quad . \qquad (6.13)$$

Within the self-consistent approach Eqs. (6.12),(6.13) are used to fit the numerical results. Two different k_d, k_m and correlation lengths ξ_d,

---

[5] Interestingly, the averaged distribution is remarkably similar to that obtained in the XY limit [111]. This may lead to a misinterpretation of the experimental results.

ξ_m are introduced to improve the quality of the fits. Yet, the distortive and the magnetic variables are expected to be equal on the basis of the continuum approach. Fig. 6.15 shows the DMRG data for δ_i, $\langle S_i^z \rangle$ and the fits according to Eqs. (6.12),(6.13).

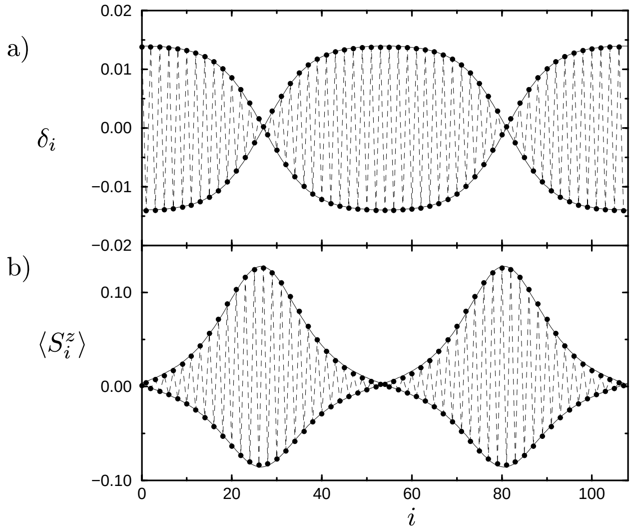

Figure 6.15: a) Local distortions: symbols stand for the self-consistent DMRG result at $K_0 = 18J$ and $\alpha = 0.35$; solid line stems from (6.13) with $\delta = 0.014$, $k_\mathrm{d} = 0.965$, and $\xi_\mathrm{d} = 10.1$.
b) Local magnetizations: symbols denote the DMRG result; solid line stems from (6.12) with $W = 0.21$, $R = 5.0$, $k_\mathrm{m} = 0.992$, and $\xi_\mathrm{m} = 7.8$.

The values for W, R can be reconciled with the experimental results with an averaging factor of $\gamma = 0.1875$. The magnetic correlation length of 7.8 sites is similar to the one found in the experiment for low fields [122]. The accordance of the magnetic correlation lengths, however, does not hold for larger magnetic fields, i.e. for increasing soliton concentration. The field dependences of the experimentally and numerically derived $\xi_\mathrm{m}(H)$ are opposite. For larger fields the numerical magnetic correlation length increases whereas the experimental one is found to decrease [116, 122].

Obviously, the fits shown in Fig. 6.15 are very close to the numerical data. Nevertheless, there are severe discrepancies in comparison to the continuum field results. The most important one is the difference between the magnetic correlation length $\xi_{\mathrm{m}} = 7.8$ sites and the distortive correlation length $\xi_{\mathrm{d}} = 10.1$ sites. The ratio $\xi_{\mathrm{d}}/\xi_{\mathrm{m}} \approx 1.3$ is surprisingly close to the experimental findings. By X-ray measurement [109], ξ_{d} was determined to be 13.6 ± 0.3 whereas by NMR ξ_{m} was found to vary between about 10 and 6 lattice spacings with the larger value close to the transition [122]. However, as stated above, the field dependence $\xi_{\mathrm{m}}(H)$ is opposite in comparison to the theoretical one.

Further numerical investigations show the ratio $\xi_{\mathrm{d}}/\xi_{\mathrm{m}}$ to be strongly frustration dependent. $\xi_{\mathrm{d}}/\xi_{\mathrm{m}}$ varies from about 1.07 for $\alpha = 0$ to 1.45 for $\alpha = 0.5$. Some further details concerning the analysis of the discrepancies between the numerical results and the continuum field theory and a clue to a possible improvement of the latter is given in Ref. [124].

Chapter 7

Finite Temperatures

So far zero-temperature properties have been investigated. In the following chapter thermodynamic properties of frustrated, dimerized Heisenberg chains are considered and applied to $CuGeO_3$. As outlined in chapter 3 these properties in the limit[1] $L \to \infty$ are accessible by means of the T–DMRG. Especially the study of low temperature properties is a challenging task since the interplay of the strong quantum fluctuations and the reduced thermal fluctuations spawns interesting physics.

7.1 General Results

In the thermodynamic limit most physical quantities are determined by the maximum eigenvalue λ_0 and the corresponding left and right eigenvectors of the quantum transfer-matrix T_M. The free energy per site is given by $f = -(T/4)\ln\lambda_{max}$. Other quantities of interest as the internal energy u and the magnetization m, per site respectively, are obtained via the expectation values of the appropriate operators. Further quantities as the entropy s, the specific heat c or the susceptibility χ are calculated by means of derivatives. In all calculations, the results of which are presented, 24 states are kept in the renormalization step

---

[1] Note, in contrast to the $T = 0$ calculations, where the system size was iteratively increased until the bulk limit was reached, here, all results are in the thermodynamic limit at the outset, since only the largest eigenvalue of the transfer-matrix is considered (cf. Eq. (3.6)).

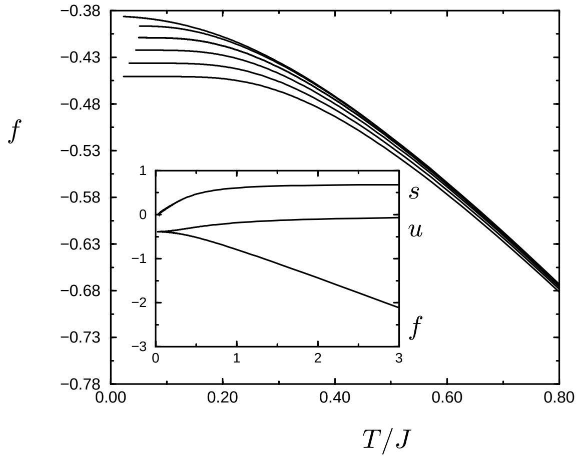

Figure 7.1: Free energy per site for $\alpha = 0.35$ and $\delta = 0, 0.4, 0.8, 1.2, 1.6$, and 2 from top to bottom. The inset shows in addition the internal energy u and the entropy s for $\alpha = 0.35$ and $\delta = 0$.

and $\epsilon = (TM)^{-1} = 0.05$ is chosen.

For convenience the elastic energy is neglected during the calculation pending further notice, i.e. $K_0 = 0$. The constant offset $\frac{K_0}{2}\delta^2$ is added later on. Exemplarily Fig. 7.1 shows the free energy f per site for $\alpha = 0.35$ ($K_0 = 0$) and several dimerizations. In addition the global behaviors of f, internal energy u, and entropy s are depicted in the inset. As has to be expected for a spin-1/2 chain, $f \sim -T \ln 2$ for large temperatures.

Clearly, increasing dimerization leads to a reduction of the free energy in the entire temperature range. This is due to the fact that the elastic energy was set to zero. Adding the offsets $\frac{K_0}{2}\delta^2$ for each dimerization, in principle, the temperature dependence of the order parameter $\delta(T)$ can be deduced by minimizing $f(T, \delta(T))$. Hence, the phase transition is directly accessible by the inspection of the free energy.

Yet, it is more accurate to compute $\delta(T)$ by means of the expectation value of the dimerization which is given by the derivative of the free energy with respect to δ

$$\langle \mathbf{S}_1\mathbf{S}_2\rangle - \langle \mathbf{S}_2\mathbf{S}_3\rangle \propto \frac{\partial f(T,\delta)}{\partial \delta}\Big|_{K_0=0} . \tag{7.1}$$

For the numerical evaluation a discrete set of dimerization values is chosen and for each δ_i the expectation values of the left hand side are computed. The phase transition takes place if

$$(\langle \mathbf{S}_1\mathbf{S}_2\rangle - \langle \mathbf{S}_2\mathbf{S}_3\rangle)(T) = 2\delta_i \frac{K_0}{J} . \tag{7.2}$$

Two representative results for $\alpha = 0$ and $\alpha = 0.35$ of the resulting order parameter, i.e. the sets $\{\delta_i(T)\}$ which are defined via Eq. (7.2), are depicted in Fig. 7.2. The exponents at the critical temperature T_{SP} are close to 1/2. This had to be expected due to the mean-field treatment of the elastic degrees of freedom. The numerical analysis, i.e. the computation of the expectation values in Eq. (7.2), has been performed with a step size of 0.01 for δ up to a value of 0.15 which appears to be an upper bound for the actual $\delta(T=0)$ for both sets of

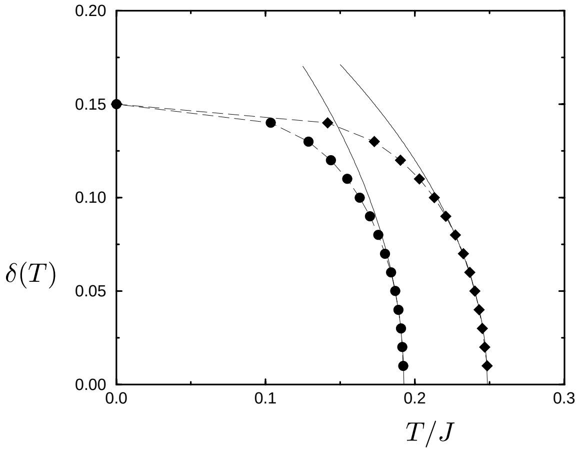

Figure 7.2: Spontaneous dimerization versus temperature for $\alpha = 0$, $K_0 = 1.6J$ (circles) and $\alpha = 0.35$, $K_0 = 2.4J$ (diamonds). The lines show fitted functions of type $c \cdot (T_c - T)^\beta$ with β fixed at 1/2.

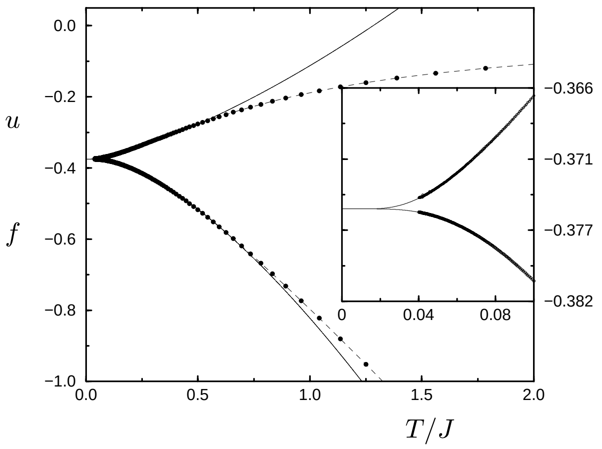

Figure 7.3: The symbols depict the T–DMRG results for Majumdar-Ghosh model for the free and the internal energy (lower and upper curve, f and u, respectively). The solid lines are fits as discussed in the text: $f = -0.375 - \gamma\,\mathrm{e}^{-\Delta/T}\,T^{3/2}$ with $\Delta = 0.1138$, $\gamma = 0.50$ (lower curve) and $u = -0.375 + \gamma\,\mathrm{e}^{-\Delta/T}\,\{1/2\,T^{3/2} + \Delta\,T^{1/2}\}$ (cf. Eq. (7.5)) with $\Delta = 0.1140$ and $\gamma = 0.48$ (upper curve). The fit interval was chosen to be $0.04 < T/J < 0.1$. A magnification of the relevant temperature range is shown in the inset.

parameters. The value is in agreement with the self-consistent DMRG calculations at zero temperature. Moreover, the critical temperature as a function of the elastic constant as well as a function of the dimerization $\delta(T = 0)$ can be deduced from Eq. (7.2).

With the help of the T-DMRG technique the quantities f,u, and s can be reliably computed down to temperatures of the order of $10^{-2}J$ using the parameters given above. The ground state energy per site in the thermodynamic limit, $e_0(L = \infty)$, can be read off directly from the free energy (cf. Fig. 7.1). Keeping 24 states in the truncation this procedure yields an error of the order of 10^{-4} in comparison to the $T = 0$ DMRG results. The truncation error, however, affects the free energy least, since it is directly deduced from the maximum eigenvalue of the transfer-matrix. The accuracy of other quantities which are obtained by means of expectation values or derivatives is lower.

Another quantity of interest in the low temperature regime is the excitation gap Δ. Within the finite-temperature approach it cannot be calculated directly. But it is accessible by fitting the T–DMRG results for small temperatures. In one dimension a quadratic minimum in the dispersion leads to a square root divergence of the density of states:

$$\mathcal{D}(\omega) \;=\; \frac{\gamma}{\sqrt{\omega-\Delta}} + O(1)\ . \tag{7.3}$$

Hence, for $T \ll \Delta$ the partition function is given by

$$\begin{aligned} Z &= 1+\int_{\Delta}^{\infty} \mathcal{D}(\omega)\mathrm{e}^{-\omega/T}\mathrm{d}\omega \\ &= 1+\gamma\sqrt{\pi}\,\mathrm{e}^{-\Delta/T}\,T^{1/2}\ . \end{aligned} \tag{7.4}$$

Thus, the singular part of the free energy is proportional to $\mathrm{e}^{-\Delta/T}\,T^{3/2}$. In this limit the internal energy is given by

$$\begin{aligned} u &= e_0+\int_{\Delta}^{\infty} \mathcal{D}(\omega)\omega\mathrm{e}^{-\omega/T}\mathrm{d}\omega \\ &= e_0+\gamma\sqrt{\pi}\,\mathrm{e}^{-\Delta/T}\,\{\frac{1}{2}T^{3/2}+\Delta\,T^{1/2}\}\ . \end{aligned} \tag{7.5}$$

In Fig. 7.3 the free and internal energies of the Majumdar-Ghosh model ($\alpha = 0.5$, $\delta = 0$) [18,19] are displayed together with the fits from which the gap is deduced[2].

Obviously the fit functions are well in accordance with the numerical data. Surprisingly the qualitative agreement holds for temperatures up to about $J/2$. The resulting gap values 0.1138 from the free-energy fit and 0.1140 from the internal-energy fit coincide quite nicely. Both values depend weakly on the fit interval, which was chosen to be $0.04 < T/J < 0.1$ in either case. The gap values are quite close to half of the singlet-triplet gap of the Majumdar-Gosh model

---

[2] As discussed on page 105 (appendix B) the ground state energy of the Majumdar-Ghosh model equals $0.375J$.
The last term in the expansion of the internal energy (7.5) is not systematic, since further terms of the density of states (7.3) have to taken into account. It turns out, however, that the quality of the fits is improved includung the term $\propto \mathrm{e}^{-\Delta/T}\,\Delta\,T^{1/2}$.

$\Delta_{01}/2 \approx 0.1169$ [20]. The origin of the factor 1/2 is the following. The elementary excitations are spinons each with a gap $\Delta = \Delta_{01}/2$, occurring, however, pairwise. Therefore, the spectroscopic data show a gap $2\Delta = \Delta_{01}$. For the thermodynamical data like the free or internal energy the activated behavior shows a characteristic energy corresponding to the gap of the individual elementary excitations. Whether these occur in arbitrary numbers or restricted to even numbers does not matter, see e.g. Ref. [125].

The quantitative determination of the gaps by fitting the above functions yields reliable results only if the gap is sufficiently large. The key problem is that the above approximation (Eqs. (7.4),(7.5)) is valid for low temperatures ($T \ll \Delta$) where the error of the T–DMRG method is maximum.

7.2 CuGeO$_3$

So far, in modeling CuGeO$_3$ the low-temperature regime around T_{SP} ($T_{\text{SP}}/J \approx 0.08$) has been unaccessible. Earlier calculations by means of exact diagonalization gave reliable results for temperatures down to about 35 K($\approx 0.22J$) [51]. For lower temperatures finite-size effects become too strong and an accurate extrapolation to the bulk limit is not possible. By applying the T–DMRG algorithm physical properties down to $T = 0.04J \sim 6$ K, well below T_{SP}, are now accessible. This corresponds to the temperature range commonly used in experiments. Even lower temperatures can be reached by increasing the number of basis states kept.

Applying the above approach to CuGeO$_3$, i.e. using a realistic set of parameters, several quantities can be derived, once the order parameter $\delta(T)$ is determined. In the following the susceptibility and the entropy are computed. These can directly be compared to the experimental results.

After having fixed the frustration α to 0.35, a value which is well established by now, the only adjustable parameter is the elastic coupling constant K_0. It is determined from the requirement of reproducing the critical temperature of CuGeO$_3$. For $K_0 = 11J$ the calculated critical temperature is equal to the experimentally observed value $T_{\mathrm{SP}} = 14.4\,\mathrm{K}$ (see e.g. [88, 119, 126]). Both, the experimental and the theoretical

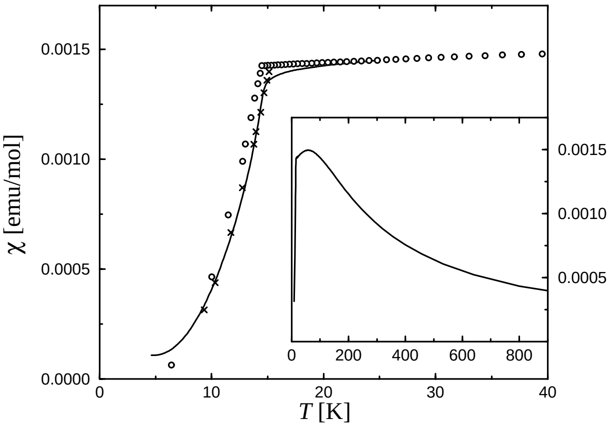

Figure 7.4: Zero field susceptibility of CuGeO$_3$. Comparison of experimental data (solid line) for the c-axis (g-factor 2.05) with the DMRG results using $K_0 = 11J$ (circles), $K_0 = 10.2J$ (crosses). The inset shows the global behavior of the calculated ^{4} susceptibility for temperatures up to 900 K.

susceptibilities are displayed in Fig. 7.4. The T-DMRG results and the experimental data agree very well. For $K_0 = 11J$, however, the susceptibility is systematically overestimated below T_{SP}. Using $K_0 = 10.2J$, the T-DMRG results perfectly coincide with experiment also for $T < T_{\mathrm{SP}}$ as shown in Fig. 7.4. Yet, the larger value for the elastic constants implies a transition temperature of about 15.2 K. This overestimation is a natural effect due to the applied mean-field approximation for the phonons. Neglecting the spatial fluctuations stabilizes the ordered phase. A similar overestimation of T_{SP} is observed by fitting a square root behavior to the experimentally measured order parameter [119]. Furthermore, there is an uncertainty of about 2% in the experimental determination of T_{SP} (cf. [119]).

Fig. 7.5 shows the entropy $s(T, \delta(T))$ for $\alpha = 0.35$. The solid lines indicate the entropy bounds derived by an analysis of the magnetic part of

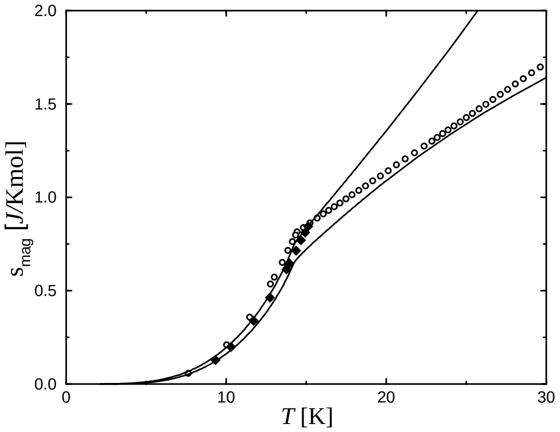

Figure 7.5: Entropy for $CuGeO_3$. Comparison of experimentally determined bounds (solid lines) with DMRG results using $K_0 = 11J$ (open circles) and $K_0 = 10.2J$ (solid diamonds).

the experimental specific heat. For temperatures above 35 K the consistency with exact diagonalization results was already mentioned in Ref. [51]. Clearly, the experimentally determined bounds are respected also for temperatures between T_{SP} and 35 K. Below the critical temperature one observes deviations of about 5% with respect to the upper bound for $K = 11J$. Decreasing the elastic constant to $K = 10.2J$ with the consequences stated above the bounds are respected in the entire temperature range.

In conclusion, the T–DMRG method provides an excellent tool for the investigation of the low temperature regime of dimerized, frustrated spin chains. In principle the temperature dependence of any thermodynamic quantity can be calculated down to extremely low temperatures of the order of $10^{-2}J$.

As stated above, regarding $CuGeO_3$, it turns out that a spring constant $K_0 = 11J$ has to be used to reproduce the experimentally observed critical temperature of $T_{SP} \approx 14.4$ K, using the parameters $J = 160$ K, $\alpha = 0.35$ as established by high temperature studies. The value

$K_0 = 11J$ $(10.2J)$ implies a maximum dimerization of $\delta(T = 0) \approx 2.6\%$ (2.8%) leading to a singlet-triplet gap of $\Delta_{01} \approx 40\,\mathrm{K}$ (42 K). The large dimerization compares well with recent results of Büchner *et al.* [127]. They conclude a minimum dimerization of 3% based on measurements of the pressure dependence of the exchange couplings together with the structural distortion.

The resulting triplet gap of about 40 K is considerably larger than the minimum experimental gap of about 25 K which was used in section 5.1 to determine the dimerization. Yet, interchain coupling has been completely neglected so far. As a first step it could be approximately included regarding the triplet dispersion along the b-direction. Averaging the gap in b-direction yields a value of 44 K, which is quite close to the theoretical value of 40 K (42 K) corresponding to $K_0 = 11J$ $(10.2J)$.

Nevertheless, the above K_0 values deviate notably from the elastic constant $K_0 = 18J$ $(\delta(T=0) \approx 1.3\%)$, which was used in the previous section for modeling several $T = 0$ properties.

Here, magnetic susceptibility (Fig. 7.4) and entropy (Fig. 7.5) of CuGeO$_3$ are almost perfectly reproduced with $K = 10.2J$. The slight deviation in the value of T_{SP} can be traced back to the mean-field treatment of the lattice dimerization which overestimates transition temperatures.

Chapter 8

Conclusion

8.1 Summary

The present thesis deals with the investigation of SP systems, which is performed by a detailed analysis of dimerized, frustrated Heisenberg chains. Based on this model a number of properties of the anorganic SP compound $CuGeO_3$ are discussed using the adiabatic approximation for the phononic system.

For a thorough study of the model two related and yet complementary numerical methods are used: the DMRG [3,4] and the T-DMRG [5–7]. They are related as both methods apply the same renormalization concept using the density matrix [3, 4] for the selection of the most important basis states. They are complementary since the DMRG method is suitable for investigating zero-temperature properties, whereas the T-DMRG approach covers the finite-temperature regime, however, without being applicable to arbitrarily low temperatures. Both methods are introduced in the first part of the thesis.

Having provided the numerical tools, fundamental properties of the SP compound $CuGeO_3$ are reviewed. Motivated by structural arguments, the 1-d Hamiltonian for the spin system is set up, treating the 3-d phononic system in mean-field approximation. Whether the adiabatic approximation of the phonons is justified or not is not clear at the outset, however, it is indispensable for an efficient numerical treatment of the spin-phonon system. Within this approach many experimentally observed features of $CuGeO_3$ are reproduced and a remarkable agreement between numerical and experimental results is obtained in several cases. Hence, the justification of the chosen adiabatic approach can be given *a posteriori*.

The first step in modeling $CuGeO_3$ is the determination of the dimerization parameter δ, using the values for the exchange coupling ($J = 160\,\mathrm{K}$) and the frustration ($\alpha = 0.35$) that are fixed in the U phase [50, 51]. A relative dimerization of $\delta(T)|_{T=0} \approx 1.2\%$ is found to reproduce the experimentally observed singlet-triplet gap of about 25 K.

The internal consistency of the chosen set of parameters is verified by the almost quantitative reproduction of the singlet-singlet energy gap[1] as measured in Raman light scattering experiments for $T < T_{\mathrm{SP}}$.

Surprisingly, the lowest singlet excitation is found to scale non-monotonously with increasing system size. The application of the DMRG method, however, allows to read off the gap value directly, without the knowledge of the appropriate scaling function, as the system size can be increased such that the thermodynamic limit is reached.

For a detailed analysis of soliton[2] properties a new self-consistent approach is set up. The self-consistency is necessary because of the interdependence of lattice distortion and magnetic degrees of freedom due to the spin-phonon coupling.

First, this method is applied to the investigation of doped systems. Within the self-consistent treatment of the distortions two features of doped $CuGeO_3$ find a natural explanation: firstly, the observed AF ordering in coexistence with the SP phase [76–80], secondly, the appearance of an additional peak in the Raman spectra of the doped samples $Cu_{1-x}Zn_xGeO_3$ [58].

Here, Zn/Mg ($S = 0$) impurities are modeled by removing a single spin and dissecting the spin chain, i.e. neglecting the remaining next-nearest neighbor coupling αJ. Inserting a vacancy one singlet is broken

---

[1] The numerically derived gap is close to, but 13% below the experimental result. Choosing a slightly larger dimerization of 1.3% *both*, singlet–triplet and singlet–singlet gap are reproduced within an error of a few percent.

[2] To recall the terminology, in this context the entity consisting of a spinon, i.e. a dressed free spin, and the concomitant zero in the lattice modulation is denoted as *soliton*.

since a singlet partner is lacking. The resulting spinon, i.e. the dressed freed spin, becomes bound to a chain end as soon as elastic interchain coupling is taken into account. However, due to its delocalization the spin without partner affects a number of dimers. The calculation of the resulting non-vanishing local magnetizations yields unexpectedly strong AF correlations in large domains. Although the total magnetization is fixed, e.g. $S^z = +1/2$, half of the affected spins show a considerably negative magnetization. In a real, 3-d crystal magnetic interchain coupling is likely to cause a spatial arrangement of the AF ordered domains leading to AF long-range order, as revealed by experiments.

The appearance of an additional peak in the Raman spectra can as well be explained within the picture outlined above. Having determined the adaptive modulation of the dopant-bound soliton, excited states are analyzed while the modulation is kept fixed. In comparison to the uniform dimerized case an *additional* singlet excitation occurs, whereas the triplet excitations remain almost unaffected by the solitons at the edges. The experimentally found energy of the additional singlet excitation is, however, not reproduced. This quantitative discrepancy can probably be attributed to magnetic interchain coupling, which is neglected in the calculations.

Basically, there are two ways of creating solitons. One possibility is via the insertion of impurities, as discussed above. The other possibility is to apply an external magnetic field. For sufficiently large magnetic fields a number of singlets are broken implying the pairwise creation of spinons or solitons. In this high-field phase an incommensurate modulation is stabilized by the Zeeman energy due to the net magnetization of the individual spinons. The resulting soliton lattice is investigated within further self-consistent calculations.

Measurements of the spontaneous strain $\epsilon(H)$, i.e. the relative length change due to dimerization, provide some insight into the modulation in the I phase. The experimental quantity $\epsilon(H)$, which is accessible via thermal expansion and magnetostriction measurements [117–120], is directly correlated to the average squared distortion, i.e. the elastic energy of the modulation. Indeed, the numerically derived elastic energy as a function of the magnetic field complies perfectly well with the experimentally determined $\epsilon(H)$ of $CuGeO_3$. In particular the value of the critical field $H_c \approx 12.5\,\mathrm{T}$ and the saturation value of about 1/4 of the zero-field value are reproduced within the self-consistent approach using the parameters which were determined in the U and in the D phase solely. The numerically and experimentally observed saturation of $\epsilon(H)$ for fields higher than 20 T, is in contradiction with the analytical approach commonly used (Eq. (6.11)) [92, 94–97, 114]. A kink-like modulation with constant correlation length ξ can be excluded, due to the observed saturation of $\epsilon(H)$, which comes along with the saturation of the maximum dimerization

A more elaborate analysis of the soliton structure in the I phase is possible on the basis of recent NMR results [122]. The calculated overall NMR line shape is well in accordance with the experimental result if phasonic zero-point fluctuations are taken into account. Since only static distortions are considered in the approach chosen, phasonic fluctuations have to be included later on approximately by performing an averaging over nearest neighbor sites. Due to the strong AF correlations within the spinons the averaging leads to a considerable reduction of the magnetization amplitudes in accordance with the experimental results of $CuGeO_3$ [111, 116].

A close inspection of the adaptive modulations and the corresponding local magnetizations, in context with the analytical approaches, reveals that two different correlation lengths ξ_m and ξ_d are involved in the magnetic and the distortive structure of the solitons, respectively. In fair accordance with the numerical result experiments provide also evidence for the difference between both lengths [109, 122]. The field dependence of the magnetic correlation length ξ_m deduced from the NMR data [122] is, however, opposite to that of the theoretical result. Further studies need to be conducted to clarify this point.

Besides modeling $CuGeO_3$, several more general aspects of dimerized, frustrated spin-1/2 Heisenberg chains are investigated. These are the gap growth, the ground state energy as a function of dimerization and the transition to the high-field phase for dimerized, sinusoidally modulated, and adaptively modulated chains. With respect to the first quantities, gap growth and ground state energy, the DMRG findings comply well with the few known exact results and scaling relations. The results derived in regard to the D-I phase transition are in accordance with the discussed considerations.

The last part of the thesis is dedicated to the investigation of finite-temperature properties. Using a variant of the T-DMRG method, the low-temperature regime and in particular the phase transition from the U into the D phase is studied in detail. Once the order parameter as a function of temperature is determined by calculating the appropriate correlation function, the susceptibility and the entropy can be computed. Using the above values for the exchange coupling and the frustration, which are established by several high-temperature studies, an elastic constant $K_0 \approx 11J$ is necessary to reproduce the experimentally observed critical temperature of $T_{\text{SP}} \approx 14.4\,\text{K}$. Results from the above parameter set for both, susceptibility and magnetic entropy, do perfectly agree with the experimental data [138]. There is, however, a discrepancy regarding the parameter set, or more precisely the elastic constant, used throughout the $T=0$ calculations ($\Delta \approx 25\,\text{K} \hookrightarrow K_0 = 18J$). A spring constant of $K_0 \approx 11J$ as is to be used for $T>0$ corresponds to a maximum dimerization of about 2.6%. This dimerization in turn leads to a singlet-triplet gap of about 40 K, a gap value which is almost twice as large as the experimentally observed (minimum) gap of CuGeO_3. The large gap, however, compares fairly well with the gap of 44 K, which is obtained by averaging over the dispersions transverse to the chains [35]. In that sense the discrepancy in the spring constant may be, at least partially, attributed to the neglect of magnetic interchain coupling.

In summary, within the $T = 0$ approach the triplet and singlet gaps, the critical magnetic field, and the overall spontaneous strain of CuGeO_3 are quantitatively reproduced. Furthermore, several other properties of SP systems can qualitatively be described. Furthermore, thermodynamic quantities derived within the finite-temperature approach comply nicely with the experimental data of CuGeO_3. Regarding the question of the different dimerizations (spring constants) used in the two approaches leading to gaps of 25 K and about 40 K, it is reasonable to assume that the thermodynamic properties depend strongly on the (larger) average gap, whereas the (minimum) singlet-triplet gap is decisive for the properties at $T=0$.

8.2 Outlook

A further refinement of the self-consistent approach concerning the investigations of solitons is to consider additional magnetic interchain coupling [128]. This could lead, for instance, to a modified field dependence of the magnetic correlation length and improve the accordance with the experiment.

Regarding the finite-temperature approach further studies and comparisons to experimental data of $CuGeO_3$ are possible, such as the investigation of the pressure dependence of the critical temperature [129] and the comparison of susceptibilities in presence of external magnetic fields to the corresponding results of $CuGeO_3$. Furthermore, the calculation of the site-dependent energy-energy correlation function enables us to calculate the U-D *and* the U-I phase transition. The - quasi exact - result of the phase boundary can be compared to the approximative result of Cross and Fisher [42], to the refined version of Klümper and to the experimental phase diagram of $CuGeO_3$ (cf. Fig. 4.2).

Appendix A

Dynamical Properties

Dynamical properties of finite systems can be approximately derived using the DMRG technique in combination with the continuous fraction expansion of Green functions [16]. Here some results for the Raman spectrum (singlet excitations) are presented. Within the standard Loudon–Fleury theory of magnetic Raman scattering [49, 130] the relevant part of the Raman operator for the dimerized phase reads

$$H_R = \Lambda \sum_i (\mathbf{S}_i \cdot \mathbf{S}_{i+1} + \gamma \mathbf{S}_i \cdot \mathbf{S}_{i+2}) \ , \tag{A.1}$$

for a scattering geometry in which the incoming and scattered photons are polarized along the chain [53, 131]. Experimentally, essentially no scattering is observed in other geometries. The prefactor Λ is an overall coupling constant while the term proportional to γ arises as a consequence of frustration [131, 132]. The value of γ depends on microscopic details. It is, however, expected to be of the same order of magnitude as the frustration α due to their common microscopic origin.

The Raman excitation spectrum at $T = 0$ is given by the Fourier transform of the dynamical correlation function of the Raman operator H_R, which reads

$$\begin{aligned} I(\omega) &= \sum_i |\langle i|H_R|0\rangle|^2 \, \delta(\omega - (E_n - E_0)) & \text{(A.2)} \\ &= -\frac{1}{\pi} \lim_{\eta \to 0^+} \mathrm{Im} G(\omega + i\eta + E_0) \quad , & \text{(A.3)} \end{aligned}$$

where the sum in the first equation runs over all excited states $|i\rangle$ with energies E_i. The ground state with energy E_0 is denoted by $|0\rangle$. The corresponding Green function, is defined by

$$G(z) = \langle 0|H_R^\dagger (z-H)^{-1} H_R|0\rangle \quad . \tag{A.4}$$

Following Ref. [16], the function $G(z)$ is expressed in terms of a continuous fraction

$$G(z) = \cfrac{\langle 0|H_R^\dagger H_R|0\rangle}{z - a_0 - \cfrac{b_1^2}{z - a_1 - \cfrac{b_2^2}{z - a_2 - \cfrac{b_3^2}{z - \cdots}}}} \quad , \tag{A.5}$$

the coefficients a_n and b_n can be obtained via the recursion relations

$$\begin{aligned} a_n &= \langle f_n|H|f_n\rangle / \langle f_n|f_n\rangle \ , & \text{(A.6)}\\ b_n^2 &= \langle f_n|f_n\rangle / \langle f_{n-1}|f_{n-1}\rangle \ , \ b_0 = 0 \ , & \text{(A.7)}\\ \text{with} \quad |f_{n+1}\rangle &= H|f_n\rangle - a_n|f_n\rangle - b_n^2|f_{n-1}\rangle \ , & \\ \text{and} \quad |f_0\rangle &= H_R|0\rangle \ . & \end{aligned}$$

For the evaluation of Eqs. (A.3) or (A.4) with the help of the DMRG one must assure that the truncated Hilbert space contains also the relevant excited states besides the ground state $|0\rangle$. According to Ref. [16] this can be achieved by choosing appropriate target states. In this case one may choose the first few $|f_n\rangle$.

As an example Fig. A.1 displays the low energy part of the calculated Raman 'spectrum' for a 40 site chain with frustration $\alpha = 0.35$. The dashed and solid curves show the excitations with dimerization $\delta = 0.012$ and without dimerization, respectively. In both cases, 5 target states were used, keeping $m = 100$ basis states for one subblock. The resulting spectrum consists of single, well separated peaks, as was to be expected due to the finite number of kept basis states. After the DMRG iterations several coefficients a_n, b_n^2 as defined in Eq. (A.6),(A.7) are calculated up to $n = 40$. The truncated Hilbert space, however, is

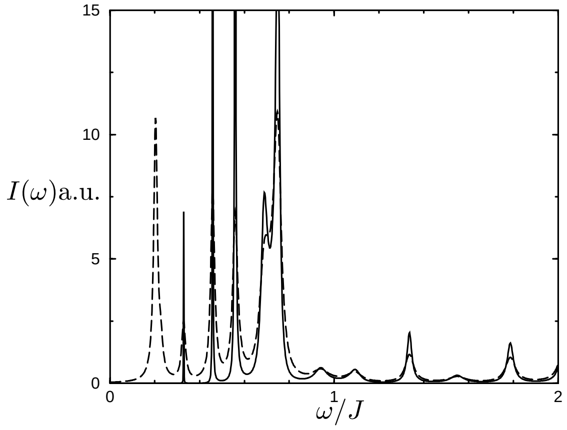

Figure A.1: Raman (singlet) excitations of a 40 site system with $\alpha = 0.35$, dimerization $\delta = 0.012$ (dashed line) and without dimerization (solid line).

designed to present only a few excitations leading to the observed peak structure. The calculation of a continuous spectrum is beyond the scope of this method, however single excitations are accessible. Here, the singlet bound state in presence of dimerization is of particular interest. As shown in Fig. A.1 (dashed line) the appearance of the extra peak, as is observed in Raman scattering experiments for $T < T_{SP}$, can be reproduced.

The fundamental drawback of this approach, the lack of accuracy due to the number of target states, was overcome by T. Kühner [17] by including the target states $A|0\rangle$, $\frac{1}{z-H}A|0\rangle$ and the ground state, with A as the operator of interest.

Appendix B

Ground State Properties

For the ground state energy per site the scaling ansatz

$$e_0(L) = e_0(\infty) - \frac{A}{L^2} \exp\left(-\frac{L}{\xi}\right) \tag{B.1}$$

is appropriate in order to extrapolate to the infinite chain limit $L \to \infty$ [53, 133], where $e_0(\infty)$ is the energy in the thermodynamic limit and ξ denotes the correlation length. The exponential function reflects the gapped situation. Fitting the above function to the DMRG results as shown in Fig. B.1 for $\alpha = 0.35$ and $\delta = 0.012$ (with periodic boundary conditions) yields a correlation length ξ of 7.36 lattice spacings. This value is in good agreement with the estimation of Khomskii *et al.* [32] of $\xi \approx 8$ sites[1]. It is also in accordance with the (experimental and numerical) result for the magnetic correlation length which is derived in context of the investigation of the NMR line shape (cf. section 6.2.2). The inset in Fig. B.1 is included to highlight that finite size effects are absent for $L > 50$.

Next we turn to the analysis of the ground state energy $e_0(\infty)$ as a function of the dimerization. The ground state energy of SP systems is known to scale like $\delta^{4/3}$ for $\alpha < \alpha_c \approx 0.2412$ [46, 48] in the limit $\delta \to 0$. This was already derived by Cross and Fisher [42] combining

---

[1] The estimate is based on the relation $\xi = \frac{v_s}{\Delta}$. Using, however, the spin-wave velocity of Fledderjohann and Gros, $v_s = \frac{\pi}{2}(1 - 1.12\alpha)$ [134], which was derived for $\alpha < \alpha_c$, as an approximation for $v_s(\alpha = 0.35)$ yields $\xi \approx 6$.

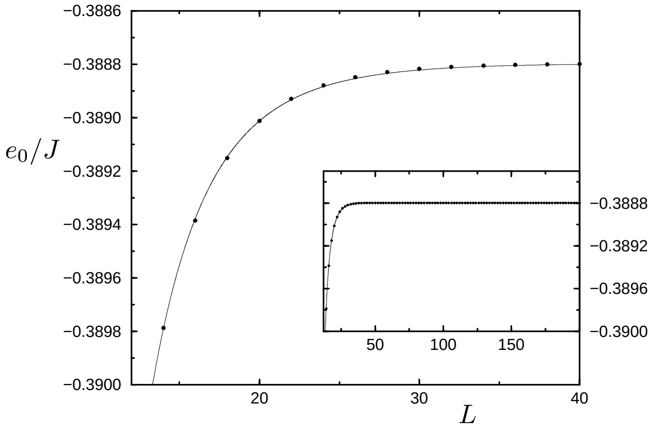

Figure B.1: Ground state energy per site for $\alpha = 0.35$ and $\delta = 0.012$ as function of the system length L with periodic boundary conditions. The solid line denotes the fit corresponding to Eq. (B.1). The inset shows the same data on a larger scale.

bosonization results with scaling relations of the polarizability. The above relation has been rederived by Klümper on the basis of conformal field theoretical arguments [43].

For $\alpha > \alpha_c$ and $\delta = 0$ the (degenerate) ground state is spontaneously dimerized. In presence of finite dimerization the degeneracy is lifted and the ground state energy decreases linearly with δ. In general, for scaling exponents less than 2 the gain in magnetic energy overcompensates the cost of elastic energy which is proportional to δ^2, independently of the prefactors.

The DMRG results for the ground state energy per site $e_0(\delta)$ confirm the expected scaling behavior for the magnetic energy. This is shown in the following for $\alpha = 0$, α close to α_c (absence of logarithmic corrections), and for $\alpha = 0.5$, i.e. the Majumdar-Ghosh model [18].

Both degenerate ground states of the Majumdar-Ghosh model consist of decoupled singlets. The singlet pairs reside on the even or on the odd bonds. The ground state energy per site equals half the singlet energy $-3/4J$. Switching on a small dimerization δ the energy of one

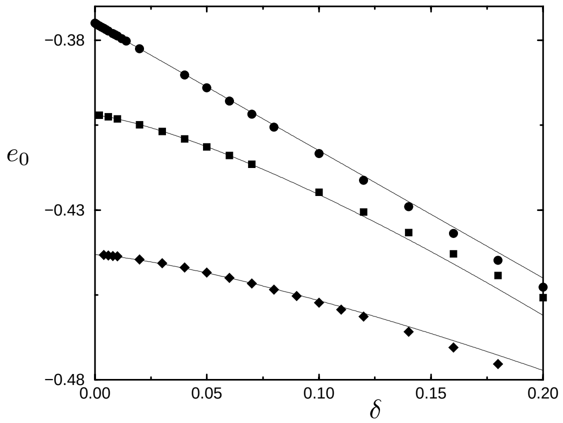

Figure B.2: Ground state energy per site versus dimerization. The DMRG results in the limit $L \to \infty$ are depicted with diamonds for $\alpha = 0$, squares for $\alpha = 0.241$ and circles for $\alpha = 0.5$. The solid lines are given by $-\ln 2 + 1/4 - 0.297\,\delta^{4/3}$ (one-parameter fit) for $\alpha = 0$, by $-0.40207 - 0.503\,\delta^{4/3}$ (two-parameter fit) for $\alpha = 0.241$, and by $-0.375 - 0.375\,\delta$ (no fit) for $\alpha = 0.5$.

ground state is lowered by $-3/8\,\delta\,L$, whereas the energy of the other state increases. As shown in Fig. B.2 (upper curve), the expected behavior $e_0(\delta, \alpha = 0.5) = -3/8 - 3/8\,\delta$ for the ground state energy per site is in excellent accordance with the numerical results.

The exact Bethe-ansatz result for the ground state energy of the Heisenberg chain ($\alpha = \delta = 0$) is known to be $-\ln 2 + 1/4$. Hence, the DMRG data in Fig. B.2 are compared to a one-parameter fit: $e_0(\delta, \alpha = 0) = -\ln 2 + 1/4 - c\,\delta^{4/3}$. The fit interval was chosen to be $0 < \delta \leq 0.06$. Reasonable agreement is achieved for δ up to 0.1. For $\alpha = 0.241$ the ground state energy is not known exactly. Thus, a two-parameter fit $e_0(\delta, \alpha = 0.241) = e_0 - c\,\delta^{4/3}$ and the same fit interval as before is used. The scaling relation is also fulfilled for δ less than about 0.1.

In conclusion, the DMRG results in the sub- and supercritical frustration regime are well in accordance with the few known exact results and with the expected scaling relations.

Appendix C

Spinon Potential

Following the approach presented in Ref. [61] the confining potential of two spinons can be calculated by applying the ideas of Talstra *et al.* [135, 136]. These authors have shown that a spinon state can be generated to 98% overlap by inserting a single spin in a Heisenberg chain which is otherwise in its ground state. Thus, in the case of two spinons one may assume that the system between both spinons is in its undimerized ground state which is the ground state of a finite segment with open boundary conditions. One has to calculate the expectation value of the dimerization operator H_{D} in this undimerized ground state in order to obtain an estimate for the interaction potential. However, since one is interested in the expectation value of H_{D} with respect to the bulk limit the bulk value $\langle H_{\mathrm{D}} \rangle$ has to be subtracted leading to [61]

$$H'_{\mathrm{D}}(L) = \sum_{j=1}^{L} (-1)^j (\vec{S}_{2j-1}\vec{S}_{2j} - \langle \vec{S}_1 \vec{S}_2 \rangle_{\mathrm{bulk}}) \ . \tag{C.1}$$

Switching on a small dimerization δ, the potential energy of the two spinons with mutual distance L is proportional to $H'_{\mathrm{D}}(L)\,\delta$. The results for $\langle H'_{\mathrm{D}} \rangle$ for three different frustrations are shown in Fig. C.1. One clearly observes a sublinear increase of $\langle H'_{\mathrm{D}} \rangle$ with the chain length. Without frustration ($\alpha = 0$) a square root power law fits the data perfectly if a small offset on the x-axis is taken into account. For larger frustration larger exponents yield better fits. The inset, however, shows

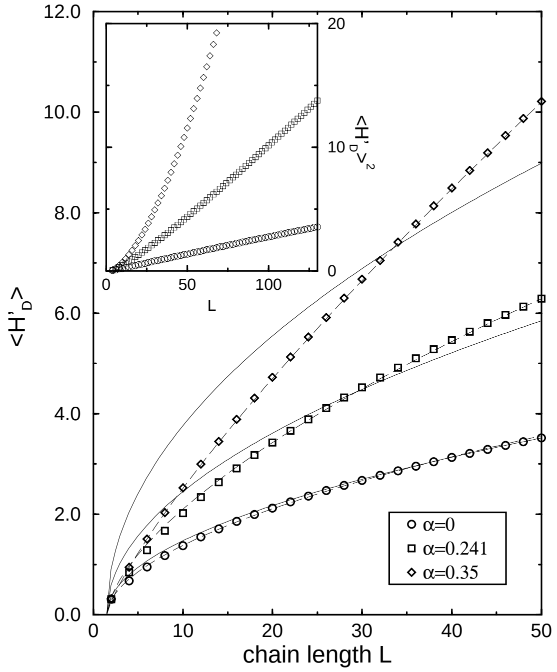

Figure C.1: Expectation value of H'_{D} as explained in the text for three values of α. The solid lines are square root fits $\propto \sqrt{L-1.5}$. The offset 1.5 is chosen for improvement of the fits. The dashed lines are power law fits $\propto (L-1.5)^{\beta}$ with the exponents 0.544 ($\alpha = 0$), 0.630 ($\alpha = 0.241$), and 0.804 ($\alpha = 0.35$). Inset: Square of the same data for longer chains.

that for longer chain lengths ($L > 50$), the square root behavior is recovered for $\alpha \leq \alpha_c$ which can be seen from the linear behavior of the squared values. The frustration value $\alpha = 0.35$ is included to show that for this value relatively close to the critical value α_c a linear behavior $\langle H'_{\mathrm{D}} \rangle \propto L$ cannot be seen for $L \leq 50$.

So the conjecture of a square root confining potential for lower frustrations is corroborated by the direct DMRG calculations. Now one can set up the spinon Hamiltonian as in the case of supercritical frustration (cf. Eq. (5.2)), but with two crucial modifications. First, one has to consider a linear kinetic energy due to the absence of a gap. Second, a square root potential has to be regarded as shown above. Rescaling of the spatial variable immediately yields that all the energies scale with $\delta^{2/3}$.

Bibliography

[1] M. Hase, I. Terasaki, and K. Uchinokura, Phys. Rev. Lett. **70**, 3651 (1993)

[2] J.G. Bednorz and K.A. Müller, Z. Phys. B **64**, 189 (1986)

[3] S.R. White, Phys. Rev. Lett. **69**, 2863 (1992)

[4] S.R. White, Phys. Rev. B **48**, 10345 (1993)

[5] R.J. Bursill, T. Xiang and G.A. Gehring, J. Phys. Cond. Mat. **8**, L583 (1996)

[6] X. Wang and T. Xiang, Phys. Rev. B **56**, 5061 (1997)

[7] N. Shibata, J. Phys. Soc. Jap. **66**, 2221 (1997)

[8] See e.g. J.N. Fields, Phys. Rev. B **19**, 2637 (1978)

[9] K.G. Wilson, Rev. Mod. Phys. **47**, 773 (1975)

[10] R.P. Feynman, *Statistical Mechanics: A set of Lectures* (Benjamin, Reading, MA, 1972)

[11] W.H. Press, B.P. Flannery, S.A. Teukolsky, and W.T. Vetterling, *Numerical Recipes: The Art of Scientific Computing* (Cambridge University Press, New York , 1986)

[12] F. Chatelin, *Eigenvalues of Matrices* (John Wiley, New York , 1993)

[13] E.R. Davidson, J. Comput. Phys. **17**, 87 (1975)

[14] C. Lanczos, J. Res. Natl. Bur. Stand. **45**, 225 (1950)

[15] J.K. Cullum, R.A. Willoughby, *Lanczos Algorithms for Large Symmetric Eigenvalue Computations* (Birkhäuser, Boston-Basel-Stuttgart, 1985)

[16] K.A. Hallberg, Phys. Rev. B **52**, R9827 (1995)

[17] T.D. Kühner and S.R. White, cond-mat/9812372

[18] C.K. Majumdar and D.K. Ghosh, J. Math. Phys. **10**, 1388 (1969)

[19] C.K. Majumdar, J. Phys. C **3**, 911 (1970)

[20] G.S. Uhrig and E. Müller-Hartmann, to be published

[21] K. Maisinger, U. Schollwöck, Phys. Rev. Lett. **81**, 445 (1998)

[22] M. Suzuki, Prog. Theor. Phys. **56**, 1454 (1976)

[23] H. Betsuyaku, Prog. Theor. Phys. **73**, 319 (1985)

[24] A. Klümper, private communication

[25] J. Stoer and R. Bulirsch, *Einführung in die Numerische Mathematik II* (Springer, Berlin, 1973)

[26] Y. Ginetti, Bull. Soc. Chim. Belg. **63**, 209 (1954)

[27] J.W. Bray *et al.*, Phys. Rev. Lett. **35**, 744 (1975)

[28] M. Hase *et al.*, Phys. Rev. Lett. **71**, 4095 (1993)

[29] J.P. Renard *et al.*, Europhys. Lett. **30**, 475 (1995)

[30] T. Lorenz, PhD thesis, Universität zu Köln, 1998

[31] W. Geertsma and D. Khomskii, Phys. Rev. B **54**, 3011 (1996)

[32] D. Khomskii, W. Geertsma, and M. Mostovoy, Czech. Journ. Phys. **46**, 3239 (1996)

[33] M. Nishi *et al.*, Phys. Rev. B **50**, 6508 (1994)

[34] L.P. Regnault *et al.*, Phys. Rev. B **53**, 5579 (1996)

[35] G.S. Uhrig, Phys. Rev. Lett. **79**, 163 (1997)

[36] R. Werner, C. Gros, and M. Braden, cond-mat/9810038

[37] For a review see: J.W. Bray, L.V. Interrante, and J.C. Bonner, in *Extended Linear Chain Compounds*, Vol. **3**, edited by J.S. Miller (Plenum Press, New York, 1983)

[38] M. Braden *et al.*, Phys. Rev. B **54**, 1105 (1996)

[39] M. Braden *et al.*, Phys. Rev. Lett. **80**, 3634 (1998)

[40] A.I. Buzdin and L.N. Bulaevskii, Sov. Phys. Usp. **23**, 409 (1980)

[41] J. des Cloizeaux and J.J. Pearson, Phys. Rev. **128**, 2131 (1962)

[42] M.C. Cross and D.S. Fisher, Phys. Rev. B **19**, 402 (1979)

[43] A. Klümper, Eur. Phys. J. B **5**, 677 (1998)

[44] R. Chitra *et al.*, Phys. Rev. B **52**, 6581 (1995)

[45] J.P. Boucher and L.P. Regnault, J. Phys. I France **6**, 1939 (1996) and references therein

[46] K. Okamoto and K. Nomura, Phys. Lett. **169**, 433 (1993)

[47] S. Eggert, Phys. Rev. B **54**, R9612 (1996)

[48] G. Castilla, S. Chakravarty, and V.J. Emery, Phys. Rev. Lett. **75**, 1823 (1995)

[49] B.S. Shastry and B. Sutherland, Phys. Rev. Lett. **47**, 964 (1981)

[50] J. Riera and A. Dobry, Phys. Rev. B **51**, 16098 (1995)

[51] K. Fabricius *et al.*, Phys. Rev. B **57**, 1102 (1998)

[52] S. Imagawa *et al.*, Physica B **201**, 178 (1994)

[53] G. Bouzerar, A.P. Kampf, and F. Schönfeld, cond-mat/9701176

[54] H. Kuroe *et al.*, Phys. Rev. B **50**, 16468 (1994)

[55] P.H.M. van Loosdrecht *et al.*, Phys. Rev. Lett. **76**, 311 (1996)

[56] P. Lemmens *et al.*, Physica B **223&224**, 535 (1996)

[57] G. Els *et al.*, Phys. Rev. Lett. **79**, 5138 (1997)

[58] G. Els *et al.*, Europhys. Lett. **43**, 463 (1998)

[59] B.S. Shastry and B.I. Shraiman, Phys. Rev. Lett. **65**, 1068 (1990)

[60] J. Riera and S. Koval, Phys. Rev. B **53**, 770 (1996)

[61] G.S. Uhrig, F. Schönfeld, M. Laukamp, and E. Dagotto, Eur. Phys. J. B **7**, 67 (1999)

[62] J. Affleck, in *Dynamical Properties of Unconventional Magnetic Systems* (NATO ASI, Geilo, Norway, 1997)

[63] H. Yokoyama and Y. Saiga, J. Phys. Soc. Jpn. **66**, 3617 (1997)

[64] S.R. White and I. Affleck, Phys. Rev. B **54**, 9862 (1996)

[65] M. Abramowitz and I. A. Stegun, *Handbook of Mathematical Functions* (Dover Publisher, New York, 1964)

[66] K. Johnston *et al.*, Phys. Rev. B **35**, 219 (1987)

[67] T. Barnes and J. Riera, Phys. Rev. B **50**, 6817 (1994)

[68] A.W. Garret *et al.*, Phys. Rev. Lett. **79**, 745 (1997)

[69] D.A. Tennant *et al.*, Phys. Rev. Lett. **78**, 4998 (1997)

[70] G.S. Uhrig and H.J. Schulz, Phys. Rev. B **54**, R9624 (1996)

[71] G. Bouzerar, A.P. Kampf, and G.I. Japaridze, Phys. Rev. B **58**, 3117 (1998)

[72] G.S. Uhrig and B. Normand, Phys. Rev. B **58**, R14705 (1998)

[73] A. Weisse, G. Bouzerar, and H. Fehske, Eur. Phys. J. B **7**, 5 (1999)

[74] M. Hase, *et al.*, Physica B **215**, 164 (1995)

[75] L.P. Regnault, *et al.*, Europhys. Lett. **32**, 579 (1995)

[76] Y. Sasago *et al.*, Phys. Rev. B **54**, R6835 (1996)

[77] M.C. Martin *et al.*, Phys. Rev. B **56**, 3173 (1997)

[78] B. Grenier *et al.*, Phys. Rev. B **57**, 3444 (1998)

[79] T. Masuda *et al.*, Phys. Rev. Lett. **80**, 4566 (1998)

[80] M. Weiden *et al.*, Physica B **233**, 153 (1997)

[81] Y. Iino and M. Imada, J. Phys. Soc. Jpn. **65**, 3728 (1996)

[82] H. Fukuyama, N. Nagaosa, M. Saito, and T. Tanimoto, J. Phys. Soc. Jpn. **65**, 2377 (1996)

[83] M. Sigrist and A. Furusaki, J. Phys. Soc. Jpn. **65**, 2385 (1996)

[84] H.-J. Mikeska, U. Neugebauer, and U. Schollwöck, Phys. Rev. B **55**, 2955 (1997)

[85] M. Mostovoy and D. Khomskii, Z. Phys. B **103**, 209 (1997)

[86] P. Hansen, D. Augier, J. Riera, and D. Poilblanc, cond-mat/9805352; E. Sørensen, I. Affleck, D. Augier, and D. Poilblanc, Phys. Rev. B **58**, R14701 (1999); D. Augier, P. Hansen, D. Poilblanc, J. Riera, and E. Sørensen, cond-mat/9807265

[87] S. Watanabe and H. Yokoyama, submitted to J. Phys. Soc. Jpn. (1999)

[88] K. Hirota *et al.*, Phys. Rev. Lett. **73**, 736 (1994)

[89] H. Fukuyama, T. Tanimoto, and M. Saito, J. Phys. Soc. Jpn. **65**, 1949 (1996)

[90] A.E. Feiguin, J.A. Riera, A. Dobry, and H.A. Ceccatto, Phys. Rev. B **56**, 14607 (1997)

[91] F. Schönfeld, G. Bouzerar, G.S. Uhrig, and E. Müller-Hartmann, Eur. Phys. J. B **5**, 521 (1998)

[92] T. Nakano and H. Fukuyama, J. Phys. Soc. Jpn. **49**, 1679 (1980)

[93] T. Nakano and H. Fukuyama, J. Phys. Soc. Jpn. **50**, 2489 (1981)

[94] M. Fujita and K. Machida, J. Phys. Soc. Jpn. **53**, 4395 (1984)

[95] S.A. Brazovskiĭ, Sov. Phys. JETP **51**, 342 (1980)

[96] S.A. Brazovskiĭ, S.A. Gordyunin, and N.N. Kirova, JETP Lett. **31**, 456 (1980)

[97] A.I. Buzdin, M.L. Kulić, and V.V. Tugushev, Solid State Commun. **48**, 483 (1983)

[98] M.C. Cross, Phys. Rev. B **20**, 4606 (1979)

[99] S.M. Bhattacharjee, T. Nattermann, and C. Ronnewinkel, Phys. Rev. B **58**, 2658 (1998)

[100] R. Chitra and T. Giamarchi, Phys. Rev. B **55**, 5861 (1997)

[101] T. Tonegawa, T. Nishida, and M. Kaburagi, Physica B **246**, 368 (1998)

[102] E. Lieb, T. Schultz, and D. Mattis, Ann. Phys. (N.Y.) **16**, 407 (1961)

[103] M. Oshikawa, M. Yamanaka, and I. Affleck, Phys. Rev. Lett **78**, 1984 (1997)

[104] D.C. Cabra, A. Honecker, and P. Pujol, Phys. Rev. B **58**, 6241 (1998)

[105] G. Chaboussant *et al.*, Phys. Rev. B **55**, 3046 (1997)

[106] B. Chiari *et al.*, Inorg. Chem. **29**, 1172 (1990)

[107] M. Troyer, M.E. Zhitomirsky, and R. Ueda, Phys. Rev. B **55**, R6117 (1997)

[108] V. Kiryukhin and B. Keimer, Phys. Rev. B **52**, 704 (1995)

[109] V. Kiryukhin, B. Keimer, J.P. Hill, and A. Vigliante, Phys. Rev. Lett. **76**, 4608 (1996)

[110] V. Kiryukhin *et al.*, Phys. Rev. B **54**, 7269 (1996)

[111] G.S. Uhrig, F. Schönfeld, and J. Boucher, Europhys. Lett. **41**, 431 (1998)

[112] G. Müller, H. Thomas, H. Beck, and J.C. Bonner, Phys. Rev. B **24**, 1429 (1981)

[113] D. Poilblanc *et al.*, Phys. Rev. B **55**, R11941 (1997)

[114] B. Horovitz, Phys. Rev. Lett. **46**, 742 (1981)

[115] Interestingly, however, one finds in the XY model with site-centered coupling of the distortions $J(i) = J(1 + \delta_i - \delta_{i+1})$ an exponentially small attractive interaction between the solitons for *small* correlation lengths of the order of 2 lattice spacings, i.e. quite large gaps.

[116] G.S. Uhrig, F. Schönfeld, J.-P. Boucher, and M. Horvatic, cond-mat/9902272

[117] T. Lorenz *et al.*, Phys. Rev. B **54**, R15610 (1996)

[118] H. Winkelmann *et al.*, Phys. Rev. B **51**, 12884 (1995)

[119] T. Lorenz *et al.*, Phys. Rev. B **55**, 5914 (1997)

[120] U. Ammerahl *et al.*, Z. Physik B **102**, 71 (1997)

[121] Y. Fagot-Revurat *et al.*, Phys. Rev. Lett. **77**, 1861 (1996)

[122] M. Horvatic *et al.*, cond-mat/9812370

[123] J. Zang, S. Chakravarty, and A.R. Bishop, Phys. Rev. **B55**, R14705 (1997)

[124] G.S. Uhrig, Habilitationsschrift, Universität zu Köln, 1999

[125] A. Klümper, Z. Phys. B **91**, 507 (1993)

[126] J.P. Pouget *et al.*, Phys. Rev. Lett. **72**, 4037 (1994)

[127] B. Büchner, H. Fehske, A.P. Kampf, and G. Wellein, Physica B **261**, 956 (1999)

[128] B. Maric, F. Schönfeld, and G.S. Uhrig, in preperation

[129] R. Raupach, A. Klümper, and B. Büchner, in preperation

[130] P.A. Fleury and R. Loudon, Phys. Rev. **166**, 166 (1968)

[131] R.R.P. Singh *et al.*, Phys. Rev. Lett. **77**, 4086 (1996)

[132] V.N. Muthukumar *et al.*, Phys. Rev. B **54**, R9635 (1996)

[133] T. Barnes *et al.*, Phys. Rev. B **47**, 3196 (1993)

[134] A. Fledderjohann and C. Gros, Europhys. Lett. **37**, 189 (1997)

[135] J.C. Talstra, S.P. Strong, and P.W. Anderson, Phys. Rev. Lett. **74**, 5256 (1995)

[136] J.C. Talstra and S.P. Strong, Phys. Rev. B **56**, 6094 (1997)

[137] T. Lorenz *et al.*, Phys. Rev. Lett. **81**, 148 (1998)

[138] A. Klümper, R. Raupach, F. Schönfeld, Phys. Rev. B **59**, 3612 (1999)

[139] G.S. Uhrig, Phys. Rev. B **57**, R14004 (1998)

[140] A.W. Sandvik, R.R.P. Singh, and D.K. Campbell, Phys. Rev. B **56**, 14510 (1997)

[141] D. Augier, D. Poilblanc, E. Sørensen, and I. Affleck, Phys. Rev. B **58**, 9110 (1998)

[142] R.J. Bursill, R.H. McKenzie, and C.J. Hamer, cond/mat9812409

[143] G. Wellein, H. Fehske, and A.P. Kampf, Phys. Rev. Lett. **81**, 3956 (1998)

Zusammenfassung

Die vorliegende Arbeit beschäftigt sich mit der – vornehmlich numerischen – Untersuchung von Spin-Peierls (SP)-Systemen. Insbesondere steht die theoretische Beschreibung der SP-Substanz $CuGeO_3$ im Mittelpunkt. $CuGeO_3$ wurde 1993 von Hase *et al.* [1] als erste anorganische SP-Verbindung identifiziert. Der Phasenübergang von der ungeordneten (U) Phase in die dimerisierte (D) Phase bei einer Übergangstemperatur von 14.4 K manifestiert sich experimentell u.a. in der rapiden Abnahme der Suszeptibilität [1] sowie in der Verdoppelung der Einheitszelle in Kettenrichtung [108].

Seit der Entdeckung von $CuGeO_3$ als anorganische SP-Substanz ist diese Verbindung Gegenstand einer Vielzahl von sowohl experimentellen als auch theoretischen Untersuchungen. Aus experimenteller Sicht zeichnet sich $CuGeO_3$ durch die Möglichkeit der Synthetisierung relativ großer, qualitativ hochwertiger einkristalliner Proben aus. Dies ermöglicht die Anwendung der ganzen Bandbreite experimenteller Methoden.

Hinsichtlich der theoretischen Beschreibung wird das rege Interesse an $CuGeO_3$ auch durch die vorwiegend eindimensionale (1-d) Struktur, den kettenförmigen Aufbau, gefördert, da eindimensionale Modelle analytisch und numerisch wesentlich leichter handhabbar sind als solche in höheren Dimensionen.

Die in der vorliegenden Arbeit präsentierten numerischen Ergebnisse sind mit Hilfe der sogenannten Dichtematrix-Renormierungsgruppe (DMRG) [3,4] erzielt worden. Bei diesem 1992 von White entwickelten Verfahren handelt es sich um einen besonders effizienten Algorithmus

zur Untersuchung ein- bzw. niedrigdimensionaler Modelle.

Aufgrund des seit 1993 durch $CuGeO_3$ allgemein wiedererweckten Interesses an SP-Systemen und der Entwicklung des DMRG-Verfahrens ein Jahr zuvor sowie aufgrund der in beiden Fällen ausschlaggebenden Eindimensionalität ist die Kombination beider, d.h. die Anwendung des DMRG-Verfahrens zur Untersuchung der SP-Phase, in gewisser Weise naheliegend. Dies bildet den thematischen Schwerpunkt der vorliegenden Arbeit.

Die wesentlichen Grundzüge der DMRG-Methode werden in Kapitel zwei vorgestellt. Hier werden unter anderem das Renormierungskonzept, die Relevanz der Dichtematrix in diesem Zusammenhang und der daraus abgeleitete Algorithmus erläutert. Des weiteren finden sich hier Beispiele zur erzielten Genauigkeit und einige Implementierungsdetails wie etwa die Hierarchie der verwendeten Klassen und Angaben zur Speicherung und Diagonalisierung der auftretenden dünnbesetzten Matrizen etc.

Eine wesentliche Erweiterung des ursprünglichen DMRG-Zugangs besteht aus der Kombination des DMRG-Konzepts mit der Methode der Transfermatrizen. Dies ermöglicht die Berechnung thermodynamischer Potentiale und verschiedener Korrelationsfunktionen im thermodynamischen Limes als Funktion der Temperatur. Auf das Transfermatrix-DMRG (T-DMRG)-Verfahren wird im dritten Kapitel näher eingegangen. Für die Anwendung dieses Verfahrens ist, im Gegensatz zu dem oben erwähnten DMRG-Verfahren, die Translationsinvarianz des Hamiltonoperators essentiell, was im vorliegenden Fall durch die Gruppierung von je zwei Spins zu einer Einheitszelle erreicht wird.

Damit sind die methodischen Grundlagen für die angestellten numerischen Berechnungen gelegt.

Im folgenden Kapitel wird zunächst der strukturelle Aufbau des anorganischen SP-Materials $CuGeO_3$ erläutert und die Ableitung des verwendeten Hamiltonoperators skizziert. Motiviert durch die kettenförmige Struktur werden die magnetischen Freiheitsgrade im Rahmen eines eindimensionalen Modells, der dimerisierten, frustrierten Spin-$\frac{1}{2}$ Heisenbergkette, beschrieben. Das eindimensionale Spinsystem ist an das dreidimensionale Phononensystem gekoppelt. Die Spin-Phonon-Kopplung impliziert eine abstandsabhängige Austauschwechselwirkung zwischen zwei benachbarten Spins, die zur Ausbildung der SP-Phase führt. Die magnetische Energie kann hierbei durch die Formation von sogenannten Dimeren, Singulettpaaren benachbarter Spins, abgesenkt werden. Der magnetische Energiegewinn ist proportional zu $\delta^{4/3}$, wobei δ die Änderung der Austauschwechselwirkungen beschreibt [42,43]. Aufgrund der Spin-Phonon-Kopplung impliziert die sich einstellende alternierende Wechselwirkung Auslenkungen der entsprechenden Kupferionen aus ihren Gleichgewichtslagen. Der mit den Auslenkungen verbundene Energieaufwand ist jedoch nur von der Ordnung δ^2, wird also von dem magnetischen Energiegewinn überkompensiert.

Um das Modell mit den oben erwähnten Methoden numerisch behandeln zu können, werden die Phononen im Rahmen der Molekularfeld-Näherung beschrieben. Man geht also von statischen Auslenkungen der Kupferionen aus. Diese Näherung ist nicht unumstritten, da sie hier nicht durch das Auftreten unterschiedlicher Energieskalen, wie es etwa bei den organischen SP-Materialien der Fall ist, gerechtfertigt ist. In der vorliegenden Arbeit kann die Rechtfertigung für den gewählten Zugang jedoch *a posteriori* gegeben werden, da sich in diesem Rahmen eine Vielzahl von experimentellen Beobachtungen zwanglos erklären läßt.

Zunächst läßt sich die Grundzustandsenergie und die Singulett-Triplett-Lücke generell als Funktion der Dimerisierung für verschiedene Frustrationen analysieren, unabhängig von der Modellierung eines realen SP-Systems. Für verschwindende Dimerisierung sind zwei Fälle zu unterscheiden: Für unterkritische Frustration, $\alpha \leq \alpha_c$[1], liegt ein ungeordneter Grundzustand und ein lückenloses Anregungskontinuum vor. Im Falle überkritischer Frustration, $\alpha > \alpha_c$, besitzt das System eine Anregungslücke. Die Symmetrie des zweifach entarteten Grundzustandes ist spontan gebrochen, und es liegt langreichweitige Dimerordnug vor. Bei endlicher Dimerisierung δ ist die Entartung des Grundzustandes aufgehoben, und es existiert eine endliche Anregungslücke (vergl. Phasendiagramm auf Seite 38).

Das gefundene Verhalten für die Grundzustandsenergie bei kleiner - aber endlicher - Dimerisierung δ stimmt mit den analytischen Resul-

---

[1] $\alpha_c \approx 0.2412$ [46–48]

taten $e_0(\delta) \propto \delta^{4/3}$ [42, 43] für $\alpha \leq \alpha_c$ bzw. $e_0(\delta) \propto \delta$ für $\alpha > \alpha_c$ gut überein[2].

Für die Singulett-Triplett-Lücke Δ_{01} findet man sowohl im Fall unterkritischer als auch im Fall überkritischer Frustration dieselbe funktionale Abhängigkeit $\Delta_{01} \approx \Delta_0(\alpha) + a\delta^{\nu}$, wobei $\nu \approx 2/3$ und $\Delta_0(\alpha \leq \alpha_c) = 0$. Die gefundene Abhängigkeit läßt sich in beiden Fällen im Rahmen des sogenannten Spinonenbildes qualitativ verstehen. Spinonen sind die elementaren Anregungen von schwach dimerisierten antiferromagnetischen Heisenbergketten. Ein Spinon hat Spin $S = \frac{1}{2}$ und entspricht einer Domänenwand, also einem Wechsel zwischen zwei möglichen Zuständen (hier zwischen zwei Dimerisierungsmustern, vergleiche z.B. Skizze auf S. 47). Die Triplett-Anregung läßt sich nun als Paar zweier gebundener $S = \frac{1}{2}$-Spinonen auffassen [61, 62]. Mit der Kenntnis der Abstandsabhängigkeit des Bindungspotentials $V(l) \propto l$ und $V(l) \propto \sqrt{l}$ (vergleiche Anhang C) für $\alpha > \alpha_c$ bzw. $\alpha < \alpha_c$ ergibt sich im Kontinuumslimes obige numerisch gefundene Abhängigkeit $\Delta_{01}(\delta)$.

Nachdem die Abhängigkeit niedrigliegender Anregungen von Frustration und Dimerisierung analysiert wurde, werden die Modellparameter durch den Vergleich mit experimentellen Daten von $CuGeO_3$ fixiert. Die Austauschwechselwirkung J und die relative Frustration α lassen sich durch Anpassen der berechneten magnetischen Suszeptibiltät an die experimentellen Daten in der U-Phase bestimmen [48, 50, 51]. Allen Rechnungen im Zusammenhang mit $CuGeO_3$ liegen im weiteren die in den Arbeiten [50, 51] ermittelten Werte, $J \approx 160K$ und $\alpha \approx 0.35$, zugrunde[3].

Der noch nicht bestimmte Modellparameter, die Dimerisierung, wird anhand der Singulett-Triplett-Lücke fixiert. Diese ist experimentell in Neutronenstreuexperimenten zugänglich [33, 34]. Numerisch läßt sich die Lücke mit Hilfe der DMRG bestimmen. Für eine Dimerisierung von ca. 1.3% ergibt sich gute Übereinstimmung mit dem experimentell

---

[2] Die lineare Abhängigkeit im Falle überkritischer Frustration ergibt sich aus führender Ordnung Störungsrechnung.

[3] Spätere Kontrollrechnungen mit Hilfe der T-DMRG-Methode bestätigen die in Ref. [50, 51] mittels exakter Diagonalisierung ermittelten Werte. Unter Verwendung dieser Werte erhält man für die magnetische Suszeptibilität eine nahezu perfekte Übereinstimmung zwischen Experiment und Theorie.

bestimmten Wert von 25K. Somit sind alle Modellparameter festgelegt.

Es stellt sich nun die Frage, wie diese Werte unabhängig von deren Ableitung überprüft werden können. Man findet, daß die Konsistenz des oben ermittelten Parametersatzes durch Vergleich der daraus resultierenden Singulett-Singulett-Lücke mit der experimentell mittels Raman-Spektroskopie bestimmten entsprechenden Lücke verifiziert werden kann[4].

Die DMRG-Methode eignet sich hervorragend zur Bestimmung der benötigten Lücken, da Spinketten von ein- bis zweihundert Spins mit vertretbarem numerischen Aufwand berechnet werden können. Die Energien des Grundzustands und niedrig angeregter Zustände im thermodynamischen Limes können aufgrund der zugänglichen Systemgrößen direkt, d.h. ohne Extrapolation, abgelesen werden. Dieser Vorteil zeigt sich besonders bei der Berechnung der Singulett-Singulett-Lücke. Das hier gefundene nicht-monotone Verhalten der Lücke als Funktion der Systemgröße überrascht. Eine Extrapolation der Ergebnisse von kleinen Systemen ($L \lesssim 28$), die mittels exakter Diagonalisierung (ED) behandelt werden können, würde hingegen die genaue Kenntnis der Extrapolationsfunktion erfordern, die hier *a priori* jedoch nicht bekannt ist.

Weitere interessante Aspekte ergeben sich bei Analyse und theoretischer Beschreibung dotierter SP-Materialien. Hier liegt der Modellbildung die Annahme zugrunde, daß die betrachteten $S = 0$–Verunreinigungen nahezu eine Unterbrechung der Ketten bewirken[5]. Durch Einfügen einer $S = 0$-Verunreinigung, also einer Leerstelle, verliert ein Spin seinen 'Singulettpartner', und es entsteht ein mehr oder minder bewegliches $S = \frac{1}{2}$-Spinon. Die Aufenthaltswahrscheinlichkeit eines Spinons ergibt sich aus den lokalen Magnetisierungen $\langle S_i^z \rangle$. Die maximale lokale Magnetisierung geht mit der Unterdrückung der Gittermodulation einher. Für das resultierende Objekt, bestehend aus Spinon und Nullstelle der Gittermodulation, wird hier der Terminus *Soliton* ver-

---

[4] Mit dem oben angegebenen Wert für die Dimerisierung können beide, Triplett- und Singulettlücke, bis auf wenige Prozent reproduziert werden.

[5] Numerische Rechnungen (ED) zeigen, daß diese Näherung für nicht zu große Frustration gerechtfertigt ist [87].

wendet.

Die Struktur des Solitons sowie dessen Bindung an das durch die Leerstelle verursachte Kettenende sind Gegenstand der numerischen Untersuchungen.

Für die sich einstellende Bindung sind zwei konkurrierende Effekte von ausschlaggebender Bedeutung. Zum einen wird die Energie einer Heisenbergkette durch eine starke Korrelation der Randspins $\langle \vec{S}_0 \vec{S}_1 \rangle$ an einem offenen Kettenende abgesenkt. Das hat zur Folge, daß der ungepaarte Spin vom Kettenende weg in die Kettenmitte gedrängt wird. Dadurch fällt dem freien Spin nur ein schwächerer bond der Kettenmitte zum Opfer.

Zum anderen wird aber jeder Kette ein Dimerisierungsmuster aufgrund der Nachbarketten vorgegeben[6]. Da der freie Spin mit einer Domänenwand, d.h. mit dem Umklapp des Dimerisierungsmusters, einhergeht, hat zwangsläufig ein Teil der Kette eine bezüglich der Nachbarketten energetisch ungünstige Dimerisierung. Um den Energieverlust aufgrund des falsch ausgerichteten Kettenteils zu minimieren, wird der ungepaarte Spin in Richtung eines der Kettenenden gedrängt. Das Wechselspiel beider Effekte führt zur Bindung des Spinons in der Nähe eines Kettenendes. Die Aufenthaltswahrscheinlichkeit kann in Abhängigkeit der verschiedenen Modellparameter mittels DMRG berechnet werden. Ergebnisse, die im Rahmen der Kontinuumsnäherung erzielt wurden, stehen mit diesen numerischen Resultaten qualitiv gut in Einklang [61].

Die hier numerisch gefundene Bindung des Solitons beinhaltet die Möglichkeit von zusätzlichen $\Delta S = 0$–Anregungen. Eine solche kann in der Tat sowohl numerisch als auch experimentell in Zn-dotiertem $CuGeO_3$ gefunden werden [58]. Eine quantitative Reproduktion der experimentell gefundenen Anregungsenergie ist, vermutlich aufgrund der Vernachlässigung von magnetischer Zwischenkettenkopplung, jedoch nicht möglich.

Bemerkenswert sind auch die starken antiferromagnetischen (AF) Korrelationen, die den Aufenthaltsbereich eines Spinons bzw. eines Solitons kennzeichnen. Die AF Bereiche bieten im Zusammenhang mit ma-

---

[6] Ausschlaggebend hierfür ist die elastische Zwischenkettenkopplung.

gnetischer Zwischenkettenkopplung eine natürliche Erklärungsgrundlage für die in dotiertem $CuGeO_3$ gefundene langreichweitige AF Ordnung [76–78].

Weiterhin werden Eigenschaften von SP-Systemen in Anwesenheit eines äußeren magnetischen Feldes eingehend untersucht. Zunächst werden allgemeine Ergebnisse bezüglich des Phasenübergangs von der D- in die inkommensurable (I)-Phase, die oberhalb eines kritischen Magnetfeldes auftritt, vorgestellt. Hierzu werden drei verschiedene Szenarien betrachtet:

Zunächst wird eine feste Dimerisierung angenommen und die Magnetisierung $m(H)$ als Funktion des anliegenden Magnetfeldes berechnet. Oberhalb des kritischen Feldes (= Singulett–Triplett–Lücke) findet man eine stetig ansteigende Magnetisierung. Bemerkenswert ist die Ausbildung eines Plateaus bei $m = 1/4$ in bestimmten Parameterbereichen der Dimerisierung und der Frustration. Für das hier untersuchte Modell wurde das Auftreten dieses Plateaus bereits kurz zuvor von Tonegawa *et al.* [101] gefunden und steht vermutlich mit dem Lieb–Schultz–Mattis–Theorem in Zusammenhang [102–104].

Um den in elastischer Röntgenstreuung beobachteten inkommensurablen Gitterverzerrungen in $CuGeO_3$ [108–110] Rechnung zu tragen, wird des weiteren eine sinusoidale Modulation der Austauschwechselwirkung betrachtet. Zunächst kann der erwartete Zusammenhang zwischen dem Modulationsparameter q und der Magnetisierung, $q = \pi(1 + 2m)$, numerisch eindeutig bestätigt werden. Unter Verwendung dieser Beziehung wird wiederum die Magnetisierung $m(H)$ berechnet. Diese zeigt einen beträchtlichen Sprung bei der kritischen Magnetfeldstärke H_c. Die sinusoidale Modulation führt also zu einem Phasenübergang erster Ordnung.

Die sinusoidale Modulation stellt natürlich nur eine näherungsweise Beschreibung der I-Phase dar. In den oben angegebenen experimentellen Arbeiten zeigt sich, daß auch höhere Harmonische zur Gitterverzerrung bzw. zur Modulation beitragen. Am zuverlässigsten läßt sich die energetisch günstigste Modulation, die sich bei einer bestimmten Magnetisierung einstellt, mittels eines selbstkonsistenten iterativen Zugangs berechnen[7]. Die ortsabhängigen Änderungen der Austauschwechselwirkungen δ_i lassen sich durch Minimierung der Energie $\langle\hat{H}(\{\delta_i\})\rangle$ iterativ bestimmen. Somit können sich die Nächstnachbar-Wechselwirkungen unter Berücksichtigung der lokalen elastischen Energien ($\propto \delta_i^2$) vollständig an das Spinsystem anpassen, weswegen im weiteren der Terminus *adaptive Modulation* verwendet wird.

Im Rahmen dieser Arbeit wird der selbstkonsistente Ansatz, der in diesem Zusammenhang in Ref. [90] eingeführt wurde, erstmalig mit dem DMRG-Verfahren, welches die Berechnung der Erwartungswerte für große Spinsysteme ermöglicht, kombiniert. Die hohe Genauigkeit dieses Zugangs zeigt sich durch Vergleich von DMRG-Resultaten für das unfrustrierte XY-Modell mit entsprechenden Daten, die mit Hilfe einer Kettenbruchentwicklung berechnet wurden [111].

Unter Verwendung der adaptiven Modulation ergibt sich ein Phasenübergang zweiter Ordnung. Die Ordnung des Phasenüberganges sowie der sich ergebende steile Anstieg der Magnetisierung für Magnetfelder kurz oberhalb H_c läßt sich qualitativ durch die Lokalität der Spinonen in Verbindung mit einer abstoßenden Wechselwirkung erklären.

In diesem Zusammenhang wird auch eine modifizierte elastische Energie betrachtet, die zusätzlich Terme der Form $\delta_i\delta_{i+1}$ enthält. Aufgrund der zusätzlichen Energieterme, die eine sinusoidale Dispersion der elastischen Konstanten implizieren, werden höhere Harmonische der Gittermodulation unterdrückt. Man erhält eine zunehmend sinusförmige Modulation. Der zu erwartende Effekt, daß sich bei genügend großer Beimischung der Nächstnachbarterme ein Phasenübergang schwach erster Ordnung ergibt[8], kann numerisch bestätigt werden. Dies ist ein interessantes Szenario für den experimentell gefundenen Phasenübergang in $CuGeO_3$, der auch nur schwach erster Ordnung ist.

Schließlich werden auch Lücken als Funktion der Magnetisierung in der adaptiv modulierten I-Phase untersucht, mit dem Ergebnis, daß sol-

---

[7] Dieser selbstkonsistente Zugang wurde auch schon bei der Modellierung der dotierten Systeme angewandt, um die Modulation der Austauschwechselwirkungen in der Umgebung der Verunreinigung bzw. der Leerstelle zu bestimmen.

[8] 'Schwach erster Ordnung' bedeutet in diesem Zusammenhang, daß nur ein relativ kleiner Sprung in der Magnetisierung auftritt.

che Lücken für festgehaltene Modulation existieren. Die Relevanz dieser Lücken für reale Systeme ist bislang noch unklar; eine experimentelle Überprüfung steht noch aus.

In bezug auf $CuGeO_3$ kann die experimentell bestimmte spontane Verzerrung[9] $\epsilon(H)$ mit entsprechenden DMRG-Daten verglichen werden. Die spontane Verzerrung beschreibt die relative Längenänderung der Probe aufgrund der Dimerisierung. Diese läßt sich mit der elastischen Energie einer modulierten Kette in Beziehung setzen, die wiederum im Rahmen der selbstkonsistenten DMRG-Rechnungen zugänglich ist. Der Vergleich beider Datensätze ergibt eine exzellente Übereinstimmung zwischen Experiment und Theorie [137] – ohne Anpassung von zusätzlichen Parametern. Alle Modellparameter sind zuvor in der U- bzw. in der D-Phase fixiert worden. Die selbstkonsistent bestimmten Verzerrungsmuster zeigen einen Übergang von einer stufenförmigen Modulation zu einer sinusoidalen Modulation. Insbesondere steht die sowohl experimentell als auch theoretisch gefundene Sättigung von $\epsilon(H)$ für Magnetfelder oberhalb von 25T mit dem gebräuchlichen analytischen Solitonzugang [92, 94, 97] im Widerspruch und schränkt daher dessen Anwendbarkeit auf Felder nahe des Übergangsfeldes ein.

Mittels NMR-Experimente sind detaillierte Informationen über die Häufigkeitsverteilung der lokalen Magnetisierungen der Kupferionen unmittelbar zugänglich. Lokale Magnetisierungen können auch im Rahmen des verwendeten Zugangs nach der selbstkonsistenten Bestimmung der adaptiven Modulation berechnet werden. Der direkte Vergleich beider Datensätze liefert zunächst eine frappierende Diskrepanz: Die experimentell bestimmte maximale Amplitude der lokalen Magnetisierungen ist um einen Faktor vier kleiner als der theoretisch ermittelte Wert. Diese Diskrepanz kann jedoch durch die im statisch modulierten Modell nicht enthaltenen Nullpunktsschwingungen sogenannter Phasonen erklärt werden [111, 116]. Phasonen sind lückenlose Anregungen im Spin-Phonon-System und entsprechen Oszillationen des Modulationsmusters bzw. des Solitongitters, ähnlich wie Phononen den Oszillatio-

---

[9] Die Verzerrung als Funktion des angelegten Magnetfeldes läßt sich mittels Experimenten zur thermischen Ausdehnung und zur Magnetostriktion bestimmen [117–120].

nen der Atome in einem Gitterverband entsprechen. Eine näherungsweise Berücksichtigung der phasonischen Oszillationen führt zu einer Mittelung der lokalen Magnetisierungen benachbarter Plätze. Aufgrund der ausgeprägten AF Korrelationen in der Nähe eines Solitons hat dies eine drastische Reduktion der Magnetisierungsamplitude zur Folge. Die Größe des zu verwendenden Mittelungsparameters kann unabhängig bestimmt werden und führt zu einer guten Übereinstimmung zwischen Theorie und Experiment.

Ein weiteres zentrales Resultat der Analyse von Gittermodulation und zugehöriger lokaler Magnetisierung ist das Auftreten von unterschiedlichen Korrelationslängen. Für den gefundenen Unterschied zwischen magnetischer und distorsiver Korrelationslänge gibt es auch experimentelle Hinweise in $CuGeO_3$. Die mittels NMR-Experimente gewonnene Abschätzung [122] der (magnetischen) Korrelationslänge beträgt nur ca. 70% des Wertes, den man aus Röntgenstreuexperimenten erhält [109]. Dies stimmt mit den numerisch berechneten Korrelationslängen recht gut überein. Allerdings kann die von Horvatic *et al.* [122] experimentell gefundene Magnetfeldabhängigkeit der magnetischen Korrelationslänge nicht reproduziert werden.

Während in den bisher besprochenen Teilen der Arbeit ausschließlich $T=0$-Eigenschaften diskutiert werden, befaßt sich der verbleibende Teil mit Eigenschaften von SP-Systemen bei endlicher Temperatur. Insbesondere der Niedertemperaturbereich ist von großem Interesse. Hier ist die Physik durch das Wechselspiel der reduzierten thermischen und der in einer Dimension besonders großen quantenmechanischen Fluktuationen bestimmt. Mit Hilfe des verwendeten T-DMRG-Verfahrens können innere Energie, Entropie, magnetische Suszeptibilität und die freie Energie im thermodynamischen Limes als Funktion der Temperatur bestimmt werden. Diese Größen werden mit abnehmender Temperatur berechnet und können mit der verwendeten Methode bis zu Temperaturen von ca. $4 \cdot 10^{-2} J (\approx 6\text{K})$ verläßlich bestimmt werden. Das heißt, der Phasenübergang in die SP-Phase, also der Anstieg des Ordnungsparameters und die Abnahme der Suszeptibilität bzw. der Entropie im thermodynamischen Limes, ist somit erstmalig rechnerisch zugänglich.

Aus der freien Energie oder mittels der direkten Berechnung des

Dimerisierungserwartungswertes läßt sich der Ordnungsparameter $\delta(T)$ als Funktion der Temperatur bestimmen. Für festgehaltene Frustration ($\alpha = 0.35$) ist der andere freie Modellparameter, die elastische Konstante K_0, durch die experimentell bestimmte Übergangstemperatur von 14.4K [88, 119, 126] festgelegt. Mit dem so gewonnenen Parametersatz und dem Ordnungsparameter wird dann die Suszeptibilität $\chi(T, \delta(T))$ in Abhängigkeit der Temperatur und $\delta(T)$ bestimmt. Das Resultat steht in hervorragender Übereinstimmung mit der experimentellen Suszeptibilität[10] von $CuGeO_3$ [138]. Außerdem kann die numerisch ermittelte Entropie $S(T, \delta(T))$ mit den experimentellen Schranken, die sich aus der Integration der magnetischen spezifischen Wärme nach Subtraktion des Phononenbeitrags ergeben, verglichen werden. Auch hier findet man hervorragende Übereinstimmung. Insgesammt stehen also auch die Resultate bei endlichen Temperaturen mit den experimentellen Ergebnissen von $CuGeO_3$ sehr gut in Einklang.

Abweichungen ergeben sich jedoch bei der Bestimmung der Federkonstanten K_0. Während man im Rahmen des $T = 0$-Zugangs $K_0 = 18J$ erhält, was einer maximalen Dimerisierung von ca. 1.3% entspricht, bedingt die Reproduktion der Übergangstemperatur von 14.4K einen Wert von $K_0 \approx 11J$. Die kleinere elastische Konstante führt zu einer Vergrößerung der Dimerisierung, die sich bei $T = 0$ nun zu ca. 2.6% ergibt. Dies impliziert eine Singulett–Triplett-Lücke Δ_{01} von nahezu 40K. Die Lücke weicht also frappierend von dem zunächst, in Kapitel vier, verwendeten Wert von 25K ab. Es ist jedoch zu bedenken, daß magnetische Zwischenkettenkopplung, die sich in $CuGeO_3$ in der gemessenen Dispersion entlang der b-Richtung senkrecht zur Kettenrichtung manifestiert [34], bisher noch nicht berücksichtigt wurde. Dies könnte näherungsweise geschehen, indem man anstatt der minimalen experimentellen Singulett–Triplett–Lücke eine über die Dispersion in b-Richtung gemittelte Lücke verwendet [35]. Die gemittelte Lücke von ungefähr 44K vergleicht sich recht gut mit dem theoretischen Wert von 40K, welchen man mit $K_0 \approx 11J$ erhält. Zudem erscheint es durchaus plausibel, daß thermodynamische Eigenschaften stärker von einer

---

[10] Beide Suszeptibilitäten wurden im Nullfeld bestimmmt. Vergleiche bei endlichen Magnetfeldern sind in Vorbereitung.

mittleren Lücke als von der minimalen Lücke abhängen, während die minimale Lücke bei sehr niedrigen Temperaturen, also im Rahmen des $T=0$-Zugangs, ausschlaggebend ist. Es ist also davon auszugehen, daß die Diskrepanz der elastischen Konstanten zumindest teilweise auf Zwischenkettenwechselwirkung zurückgeführt werden kann.

Im Rahmen des gewählten Zuganges ist die adiabatische Behandlung des Phononensystems neben der Vernachlässigung der Zwischenkettenkopplung die zweite wesentliche Näherung. Wie bereits erwähnt, ist die adiabatische, statische Behandlung der Gitterfreiheitsgrade hier nicht von vornherein gerechtfertigt. Der Grund für die gemachte Näherung ist eher pragmatischer Natur: Das Spin-Phonon-System soll mit den vorgestellten effizienten numerischen Methoden untersucht werden können.

Eine analytische nichtadiabatische Behandlung des Phononensystems hat im antiadiabatischen Limes, also im Grenzfall sehr schneller, energiereicher Phononen, vor allem zwei Konsequenzen für das resultierende effektive Spinmodell. Zum einen führt die Spin-Phononkopplung zu längerreichweitigen Spinwechselwirkungen, insbesondere zur Übernächstnachbar-Wechselwirkung, also zu Frustration [124, 139]. Zum anderen treten durch Ausintegration der Phononen temperaturabhängige Kopplungen auf [124, 139, 140]. Da es sich bei der Frustration um einen marginalen Operator handelt, der also erst ab einer gewissen Stärke zur spontanen Dimerisierung führt, ist zu erwarten, daß Dimerisierung erst oberhalb einer gewissen Spin-Phonon-Kopplungsstärke g_c auftritt. Dies kann in numerischen Studien bestätigt werden [141, 142].

Die numerischen Rechnungen unter Berücksichtigung von Phonon-Fluktuationen zeigen den nicht zu vernachlässigenden Einfluß der Phonondynamik über die Tatsache eines endlichen g_cs hinaus. Daß eine statische Dimerisierung mitunter mit experimentellen Ergebnissen unvereinbar ist, zeigt sich auch im Rahmen der vorliegenden Arbeit bei der Analyse der NMR-Spektren. In diesem Zusammenhang ist die Berücksichtigung von Fluktuationen (hier phasonische) im nachhinein durch eine geeignete Mittelung möglich, was zu einer guten Übereinstimmung zwischen Theorie und Experiment führt.

Generell sollte man das hier untersuchte Modell eher als effektives, phänomenologisches Spinmodell des zugrundeliegenden Spin-Phonon-Systems betrachten. Die vollständige (nichtadiabatische) Behandlung dieses Systems ist natürlich erstrebenswert. Diesbezüglich sind in jüngerer Zeit auch Fortschritte sowohl hinsichtlich der numerischen Untersuchungen [141–143] als auch der analytischen Behandlung gemacht worden. Jedoch sind die bisherigen Analysen bzw. Resultate noch weit von einem so umfangreichen, auf verschiedene Aspekte bezogenen Vergleich zwischen Theorie und Experiment entfernt, wie er im Rahmen des hier gewählten Zuganges möglich ist.

Auf der Basis des dimerisierten frustrierten 1-d Heisenbergmodells mit adiabatischer Behandlung des Phononensystems wird in der vorliegenden Arbeit ein abgerundetes Bild zum Verständnis der SP-Phase und damit zusammenhängender Phänomene in $CuGeO_3$ entwickelt.

Im Rahmen der vorgestellten T-DMRG-Rechnungen bieten sich weitere Vergleiche z.B. mit experimentellen Daten von $CuGeO_3$ unter Druck [129] und von $CuGeO_3$ im Magnetfeld an. Außerdem ist mittels der Berechnung der Energie-Energie-Korrelationsfunktion die Untersuchung der U-D- *und* der U-I-Phasengrenze möglich. Dies bietet erstmalig die Möglichkeit, die so - quasi exakt - berechnete Phasengrenze mit dem experimentellen Resultat für $CuGeO_3$ zu vergleichen und die von Cross und Fisher [42] gemachten Näherungen zu überprüfen. Rechnungen zu den oben genannten Punkten sind in Gang bzw. teilweise schon abgeschlossen.

Ich versichere, daß ich die von mir vorgelegte Dissertation selbständig angefertigt, die benutzten Quellen und Hilfsmittel vollständig angegeben und die Stellen der Arbeit – einschließlich Tabellen, Karten und Abbildungen –, die anderen Werken im Wortlaut oder dem Sinn nach entnommen sind, in jedem Einzelfall als Entlehnung kenntlich gemacht habe; daß diese Dissertation noch keiner anderen Fakultät oder Universität zur Prüfung vorgelegen hat; daß sie – abgesehen von unten angegebenen Teilpublikationen – noch nicht veröffentlicht worden ist sowie, daß ich eine solche Veröffentlichung vor Abschluß des Promotionsverfahrens nicht vornehmen werde. Die Bestimmungen dieser Promotionsordnung sind mir bekannt. Die von mir vorgelegte Dissertation ist von Herrn Professor Dr. E. Müller-Hartmann betreut worden.

Köln, den 28. März 1999

Friedhelm Schönfeld

Teilpublikationen:

G. Bouzerar, A.P. Kampf, F. Schönfeld, *Magnetic excitations in the spin-Peierls system* $CuGeO_3$, cond-mat/9701176

F. Schönfeld, G. Bouzerar, G.S. Uhrig, E. Müller-Hartmann, *On the incommensurate phase of modulated Heisenberg chains*, Eur. Phys. J. B **5**, Seite 521 (1998)

G.S. Uhrig, F. Schönfeld, J. Boucher, *A magnetic model for the incommensurate I phase of spin-Peierls systems*, Europhys. Lett. **41**, Seite 431 (1998)

G.S. Uhrig, F. Schönfeld, J. Boucher, M. Horvatic, *Soliton lattices in the incommensurate spin-Peierls phase: local distortions and magnetizations*, cond-mat/9902272

T. Lorenz, B. Büchner, P.H.M. van Loosdrecht, F. Schönfeld, G. Chouteau, A. Revolevschi, G. Dhalenne, *The incommensurate phase of* $CuGeO_3$ *: from solitons to sinusoidal modulation*, Phys. Rev. Lett. **81**, Seite 148 (1998)

G.S. Uhrig, F. Schönfeld, M. Laukamp, E. Dagotto, *Unified quantum mechanical picture for confined spinons in dimerized and frustrated spin S=1/2 chains*, Eur. Phys. J. B **7**, Seite 67 (1999)

A. Klümper, R. Raupach, F. Schönfeld, *Finite temperature density-matrix-renormalization-group investigation of the spin-Peierls transition in* $CuGeO_3$, Phys. Rev. B **59**, Seite 3612 (1999)

Danksagung

Herzlich bedanken möchte ich mich bei Prof. Dr. Müller-Hartmann für die Vergabe und die Betreuung der vorliegenden Arbeit. Die aktuelle und interessante Themenstellung sowie die stete Diskussions- und Hilfsbereitschaft haben wesentlich zum Gelingen dieser Arbeit beigetragen.

Besonderer Dank gilt auch Dr. Götz S. Uhrig für die lehrreiche und fruchtbare Zusammenarbeit und die Vielzahl von Ideen, Ratschlägen und Tips.

Dr. Joachim Altmann, Dr. Götz S. Uhrig, Alexander Bühler und Christian Knetter danke ich für die schöne Zeit in unserem gemeinsamen Büro, verbunden mit anregenden Diskussionen, Ratschlägen, Tischtennismatches usw.

Rainer Raupach danke ich für die angenehme und gute Zusammenarbeit bei der Implementierung des T-DMRG-Programms. Für die Ratschläge und Diskussionen im Rahmen der damit zusammenhängenden Veröffentlichung möchte ich mich neben Rainer Raupach auch bei Priv.-Doz. Dr. A. Klümper bedanken.

Desweiteren danke ich Dr. Karen Hallberg für wertvolle Hilfestellungen in der Anfangsphase der Programmentwicklung.

Dr. Bernd Büchner und Dr. Thomas Lorenz von der experimentellen Front sei für die erfolgreiche Zusammenarbeit und die anregenden Diskussionen in freundschaftlicher Atmosphäre inklusive Kaffeeversorgung gedankt.

Für's Korrekturlesen bedanke ich mich vor allem bei Joachim Altmann, aber auch herzlich bei Götz Uhrig, Rainer Raupach und last but not least bei meiner Schwester Ulrike Nauroth.

Lebenslauf

Persönliche Daten

Name:	Friedhelm Schönfeld
Geburtsdatum:	28.03.1970
Geburtsort:	Kirchen
Eltern:	Ernst Schönfeld und Helga Schönfeld, geb. Queseleit
Familienstand:	ledig
Staatsangehörigkeit:	deutsch

Schulbildung

1976 – 1980	Grundschule in Gebhardshain
1980 – 1989	Staatl. Kopernikus-Gymnasium Wissen
Juni 1989	Abitur
Sept. 1989 – Okt. 1990	Zivildienst

Hochschulstudium

Okt. 1990	Immatrikulation an der Universität zu Köln, Studiengang: Physik, Diplom
Sept. 1992	Vordiplom
Dez. 1995	Abschluss der Diplomarbeit bei Prof. Dr. E. Müller-Hartmann
ab Jan. 1996	Anfertigung der vorliegenden Dissertation unter Anleitung von Prof. Dr. E. Müller-Hartmann

Arbeitsverhältnisse am Institut für
Theoretische Physik, Universität zu Köln

April 1995 – Dez. 1995	Studentische Hilfskraft
Jan. 1996 – Juli 1997	Wissenschaftliche Hilfskraft
seit Aug. 1997	Wissenschaftlicher Mitarbeiter